Doctoral Thesis in Physics

Heusler materials with perpendicular magnetic anisotropy

Thin films for spintronics

Alessia Niesen

Bielefeld University
Department of Physics

Declaration

I wrote this thesis by myself and used none but the indicated resources. Text and figures were partly taken from corresponding publications, which originate directly from this work.

(Alessia Niesen)

Reviewers:

Prof. Dr. Günter Reiss
Prof. Dr. Thomas Huser

Bielefeld University, Department of Physics
Center for Spinelectronic Materials & Devices

Doctoral thesis
March 6, 2019

Our responsibility is to do what we can, learn what we can, improve the solutions, and pass them on.

(Richard P. Feynman)

Contents

Chapter 1

Introduction

During the twentieth century the magnetism and material science society performed a huge step from basic theory towards the experimental practice. Figure 1.1 sketches the development of (a) fundamental theory, (b) normal science, (c) materials development and (d) the industrial production during the 20th century in relation to permanent magnetism, revealing how enormous the possibilities in this field are. Most remarkable progress has been achieved in magnetic recording and storage media [1], leading to strongly growing demands on the materials and preparation techniques in these research field.

In the field of spintronics and its applications as nonvolatile memory [2] and field programmable logic devices [3, 4] the search for promising materials, which lower the production costs, provide devices with high thermal stability, long-term memory and low switching currents, is still ongoing. In order to realize energy-efficient spin-torque devices the needed properties are: high spin polarization, strong perpendicular uniaxial anisotropy K_u and low magnetic damping α.[5–7]

Since their invention in 1903 by Friedrich Heusler [8], Heusler compounds were investigated intensively due to their properties, as half-metallicity, high Curie temperatures, low magnetic damping constants, as well as perpendicular magnetic anisotropy (PMA), opening the door for energy efficient, long-term spin-torque devices. Half-metallicity [9, 10] is one of the most desirable properties of the Heusler alloys, which was theoretically predicted and experimentally proven for many cubic Co_2- and Mn_2-based Heusler com-

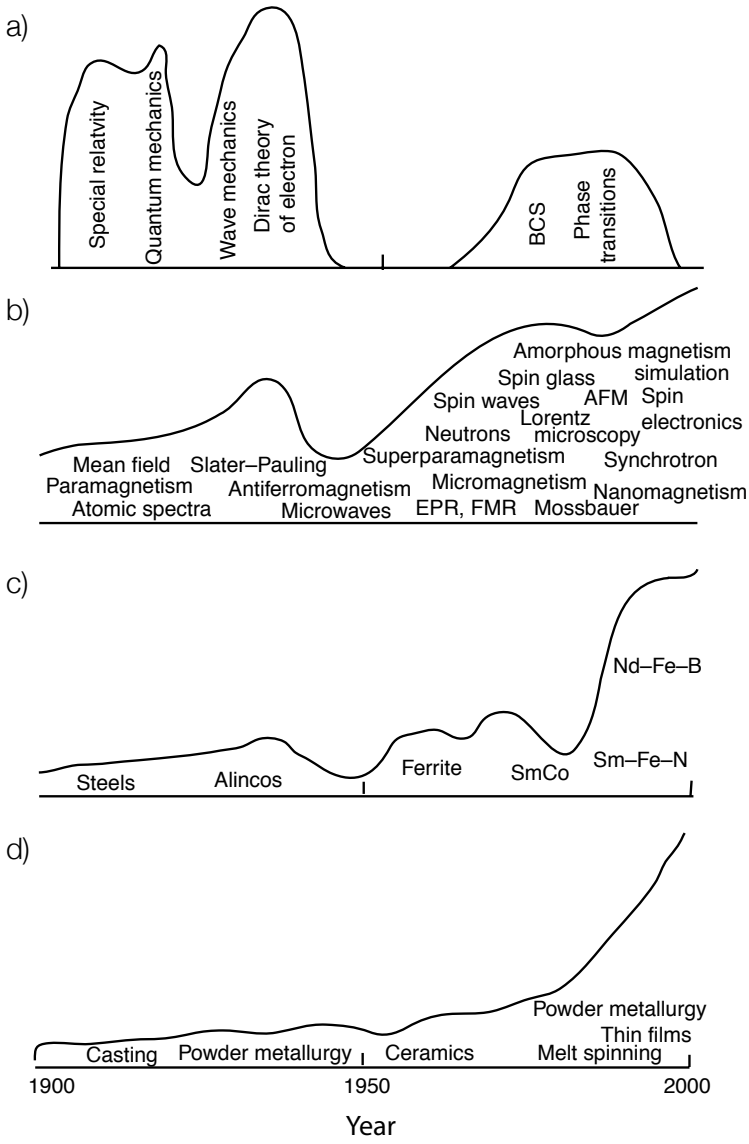

Figure 1.1. Overview of the development of a) fundamental theory, b) normal science, c) materials development and d) industrial production during the 20th century in relation to permanent magnetism. [1]

pounds. The appearance of a gap in the minority *density of states* (DOS), leading to full spin polarization of 100 %, is a result of highly symmetric

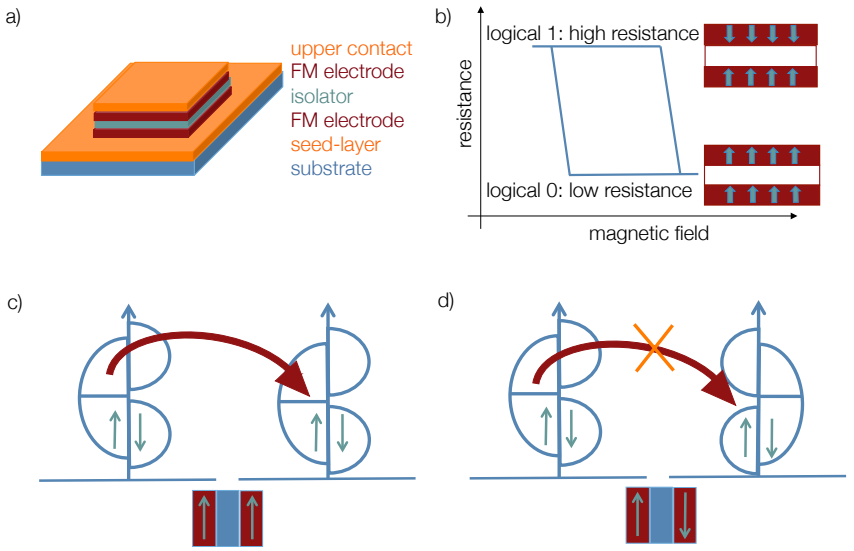

Figure 1.2. a) Typical layer stack of a magnetic tunnel junction (MTJ). The two ferro-magnetic (FM) electrodes are separated by an isolating material. In order to provide the electrical contact and also to improve the crystallographic growth of the lower electrode, a conducting material can be used as a seed-layer. The substrate and the seed-layer, thus, should provide a lattice structure similar to the FM electrode material. b) Hysteresis curve of an MTJ. In case, the magnetization of the two electrodes is oriented antiparallel, the tunneling probability of the spin polarized electrons is low and a high resistance is measured. By switching one of the electrodes and changing the magnetization orientation to parallel, the tunneling probability is high and the MTJ has a low resistance. c), d) Sketch of the DOS for half-metallic FM electrodes, for parallel (c) and antiparallel (d) configuration of the magnetization.

structure and the distinctive electronic characteristics of Heusler materials and is needed when implementing these compounds into devices as magnetic tunnel junctions, which is one of the most significant devices in spintronics. Figure 1.2(a) shows a sketch of a layer system commonly used for an MTJ. The basic structure of the MTJ itself consists of two ferromagnetic (FM) electrodes, which are separated by a thin isolating material – the tunneling barrier. The tunneling magneto resistance (TMR) is dependent on the orientation of the magnetization of the two FM electrodes to each other. In its simplest model [11] it is defined as $\mathrm{TMR} = \frac{R_{ap}-R_p}{R_p} = \frac{2P_1P_2}{1-P_1P_2}$, with R_p the resistance state with parallel alignment of the FM electrodes, R_{ap} the resistance state with

antiparallel alignment of the FM electrodes, and P_1 (P_2) the spin polarization of the conduction electrons of the FM material. The two resistance states can be assigned to a logical "0" and a logical "1" (see Fig. 1.2(b)), thus making it possible to employ these devices in magnetic random access memory (MRAM). It is also obvious, that a fully spin polarized material ($P = 1$) would lead to an extremely high TMR value. Due to the gap in one of the spin channels (see Fig. 1.2)(c) and (d)), the electron tunneling is completely blocked in the antiparallel configuration of the magnetization.

However, in reality it is highly challenging to find the right materials for the electrodes, the substrate, the seed-layer and the tunneling barrier. Beside all the intrinsic properties, mentioned above (half-metallicity, PMA, low magnetic damping, etc.), the used materials need to suit to each other. Low lattice mismatch, high crystallinity at moderate deposition temperatures, and low surface roughness are thus essential criteria for the functionality of these devices. Most materials need high deposition temperatures, in order to crystallize in the correct crystallographic structure, which on the other hand leads to increased roughness. High roughness of the electrodes leads to short cuts, so called pinholes, through the tunneling barrier, thus obstructing the tunneling of the electrons. Half-metallicity is extremely sensitive to structural changes, disorder or defects in the material, which makes it challenging to achieve fully ordered crystallographic structures using sputtering deposition techniques.

Hence, the design, preparation and investigation of novel materials that fulfill the manifold criteria, is highly essential and will be addressed in this theses. This work focuses on the investigation of two types of Heusler materials, providing **intrinsic PMA** (Mn-based compounds Mn-Fe-Ge and Mn-Fe-Ga) and **surface induced PMA** (Co-based full Heusler compounds Co_2FeAl and Co_2FeGe on a TiN seed-layer).

The Co-based Heusler compounds are already well investigated and known from literature.[12–17] Especially the possibility of achieving crystallinity at room temperature deposition, and further improvement by ex-situ post annealing processes, makes these Heusler group interesting for industrial realization. However, there is still a need for materials providing high PMA ($K_u > 0.19\,\mathrm{MJ/m^3}$), high Curie temperatures ($T_c >> 373\,K$) and low damping constants ($\alpha < 0.01$), in order to achieve long term thermal stability and low switching currents in these devices.

Mn-based compounds are more promising in terms of low magnetization (almost compensated ferrimagnetism), thus leading to low stray fields, stable and high intrinsic PMA, as well as high switching fields (coercive fields up to $\mu_0 H_c = 4\,\mathrm{T}$). $Mn_{3-x}Ga$ ($0.15 \leq x \leq 2$) is one of the well investigated compounds providing all the necessary properties.[18–20] Extensive studies were also performed for the Mn-Ge compound, which was predicted to provide small magnetic moment combined with sharp magnetization switching and large perpendicular magnetic anisotropy.[21–23] For this reason, a further improvement of these compounds by doping the materials with one additional element is investigated in this theses.

This work is organized as follows: The fundamentals and experimental methods used in this work will be introduced in the second chapter. The third chapter will be focusing on the experimental results for Mn-Fe-Ge and Mn-Fe-Ga, followed by the results for TiN buffered Co-based Heusler compounds Co_2FeAl and Co_2FeGe in the fourth chapter. The current research status of the materials is summarized in a short introduction at the beginning of each section, followed by the presentation of structural, magnetic and electrical properties of the investigated materials, collected in this work. In the final chapter a summary of all experimental results will be given including a short outlook for future work.

Chapter 2

Fundamentals and Methods

In this chapter the relevant theoretical basics and the used experimental methods are presented. The fundamentals and the theoretical basics of the Heusler compounds and their promising magnetic properties are given first. The experimental methods are divided into the following sections:

- Sample preparation
- Structural and material properties
- Magnetic properties
- Determination of the perpendicular magnetic anisotropy
- Resistivity measurements

X-ray analysis methods, used for the investigation of the **crystallographic properties, the surface roughness, the density and thickness** of the novel compounds, are presented in the first section, followed by the method, used for the determination of the chemical composition of the thin films. The surface morphology of the investigated materials is of high importance for the implementation of these materials in future applications. Therefore, atomic force microscopy, as well as the different growth modes of sputter deposited thin films are described as the last point.

The experimental methods, used for the characterization of the **magnetic properties** are presented in the second part, starting with the alternating gradient magnetometry (AGM) and vibrating sample magnetometry (VSM), which were utilized in order to determine the magnetization of the materials, followed by the magneto optical Kerr effect (MOKE), giving the coercivity and switching behavior of the thin films. The anomalous Hall effect (AHE) is described in more detail, as well as the method used for the determination of the perpendicular magnetic anisotropy, utilizing the anomalous Hall effect. The chapter finishes with a short introduction into the 4-terminal method, which was used for resistivity measurements.

2.1 Fundamentals

In this section the basics for general understanding of the investigated Heusler materials are given. Due to their manifold advantages, as half-metallicity and adjustable structural and magnetic properties, Heusler compounds attracted growing interest during the last decades. Thus, this work focuses on the investigation of Heusler compounds, starting with the fundamentals for understanding this material type.

2.1.1 Heusler compounds

Since their invention in 1903 by Friedrich Heusler [8], the research field on Heusler compounds has strongly developed due to the manifold properties and application possibilities of these materials. Especially the possible implementation in spintronic devices or the fundamental research in the field of magnetic shape-memory alloys, as well as the skyrmion-related research, led to growing interest in this material class.[24–27] The main beneficial properties, found in this large materials family, are half-metallicity, as well as the tunability of magnetic properties, which can be achieved by changing the number of valence electrons in the composition, thereby modifying the magnetic moments. The possibility to influence the crystallographic structure, and with it the magneto-crystalline anisotropy, is another huge benefit of this material class. A lot of experimental and theoretical work has been already

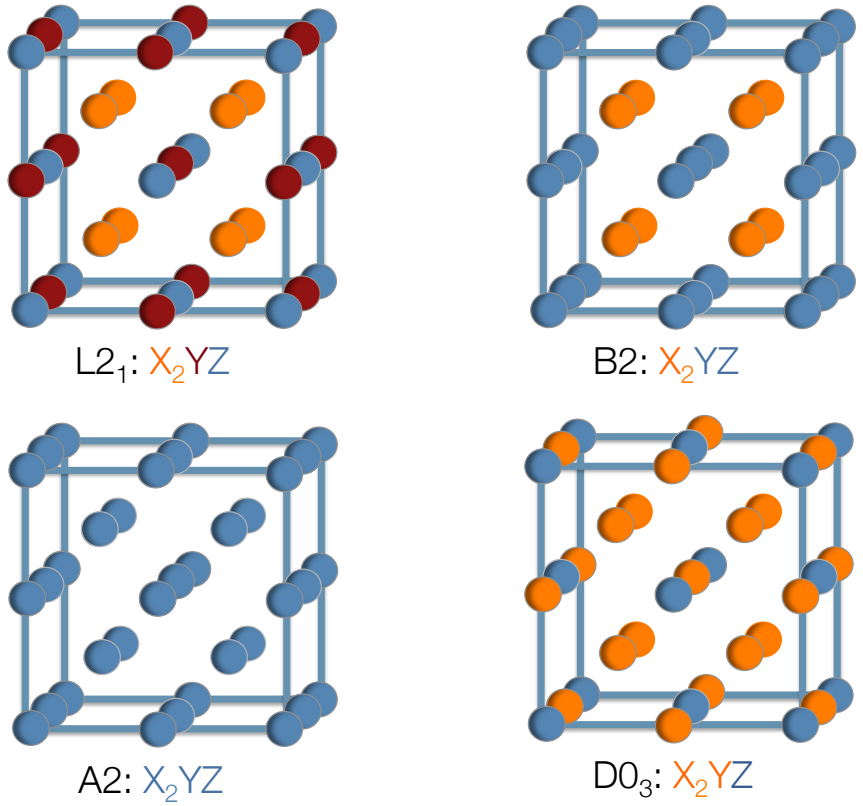

Figure 2.1. 16-atoms unit cell of the original $L2_1$ Heusler structure and chemical ordering types of the Heusler compounds.

done on multiple Heusler compounds. A detailed overview is given in [28] and [29]. Thus, in this chapter only a brief introduction into the theory of Heusler compounds will be given.

Heusler alloys are divided into two types: full Heusler alloys X_2YZ, crystallizing in the cubic $L2_1$ structure and half Heusler alloys XYZ, crystallizing in the $C1_b$ crystal structure. The $L2_1$ structure is characterized through four interpenetrating face centered cubic sublattices. Two of these sublattices are occupied by the X-element, which is typically a transition metal with the highest electronegativity, located at Wykhoff position 4*c* ($\frac{1}{4}$, $\frac{1}{4}$, $\frac{1}{4}$). The third sublattice is occupied by the Y element, which is then on the Wykhoff position

$4b$ ($\frac{1}{2}$, $\frac{1}{2}$, $\frac{1}{2}$) and can either be a transition metal with lower electronegativity, an alkaline earth metal or a rare earth element. The Z atoms occupy the fourth lattice and are a main group element, located at the atomic position $4a$ (0, 0, 0).

Depending on the chemical ordering of the elements in the Heusler unit cell and possible distortions of it, different types of related structures can be identified (see Fig. 2.1)[28]:

- $L2_1$: highest order of the X, Y and Z atoms, space group $Fm\bar{3}m$.
- $D0_3$: only the X and Y atoms are intermixed, the symmetry is preserved, space group $Fm\bar{3}m$.
- $B2$: Y and Z atoms are randomly distributed, the reduced symmetry results in the space group $Pm\bar{3}m$.
- $A2$: complete disorder of the X, Y and Z atoms, space group $Im\bar{3}m$.
- X_a: the *inverse* Heusler structure, is formed if the atomic number of the Y element is higher, than the atomic number of the X element. One of the X atoms is then located on the Wykhoff position $4b$ ($\frac{1}{2}$, $\frac{1}{2}$, $\frac{1}{2}$) (previous position of the Y atoms), and the Y atom is occupying one of the previous X-atom positions ($4c$ ($\frac{1}{4}$, $\frac{1}{4}$, $\frac{1}{4}$)). The space group is $F4\bar{3}m$.

One main focus of this theses is on novel Mn-based compounds with tetragonally distorted crystal structure, and especially the $D0_{22}$ crystallographic phase, which is related to the Heusler $L2_1$ structure. The tetragonally distorted structure was first observed for Mn_2YZ compounds, which crystallize in the inverse Heusler (X_a) structure. In this case, the Mn atoms occupy two different lattice sites, one with tetragonal and one with octahedral coordination. The Mn atom on the octahedral site possesses an oxidation state of +3 (Mn^{3+}, d^4).[9] The resulting electron configuration, caused by the triple-degenerated t_{2g} orbitals and one of the double degenerated e_g orbitals, which are each occupied by one electron, is energetically not favored. The energy is then gained by a distortion of the octahedron, through an elongation or a compression of the unit cell. The distortions lead to energetic lowering of the occupied orbitals, which results in an energy gain, often called the Jahn -Teller distortion.

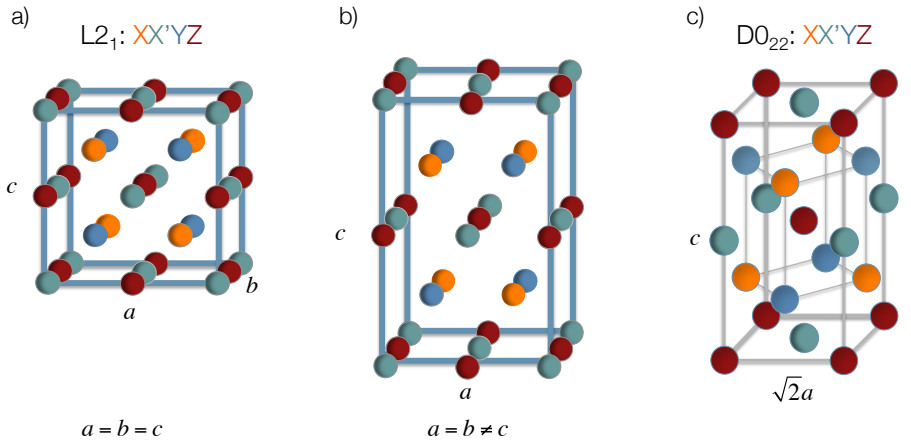

Figure 2.2. a) The $L2_1$ cubic Heusler structure. A tetragonal distortion of the cubic Heusler structure b), and subsequent redefinition of the unit cell leads to c) the $D0_{22}$ structure.

Another possibility to cause a tetragonal distortion is the presence of a saddle point in the band structure. This singularity, commonly known as the van Hove singularity, maximizes the band energy. This unpropitious condition is avoided by a tetragonal distortion of the crystal structure. In case of the Mn_2YZ compounds, the cubic unit cell is elongated along the c axis. The transition from the $L2_1$ cubic Heusler structure to a tetragonally distorted structure is depicted in Fig. 2.2(a) and (b). A subsequent redefinition of the unit cell leads to the $D0_{22}$ structure (see Fig. 2.2(c)).

Figure 2.3 illustrates the growth direction of the Heusler unit cell on the single crystalline MgO (100) (lattice constant $a_{\mathrm{MgO}} = 4.21\,\text{Å}$) substrates and the TiN buffer layer (fcc crystal structure, lattice constant $a_{\mathrm{TiN}} = 4.24\,\text{Å}$), both used in this work. Due to the relation $2a_{\mathrm{MgO/TiN}} \approx \sqrt{2}a_{\mathrm{Heusler}}$ the Heusler compounds grow 45° rotated on the MgO substrates or TiN seed layers.

The tetragonally distorted Heusler structures became more and more important, when systems with perpendicular magnetic anisotropy, as an intrinsic property, became inevitable for the miniaturization of device sizes. The tetragonal distortion can be established by tuning the Heusler compound with an additional element or by the use of substrates with lower in-plane lattice constant a, e.g. $SrTiO_3$ (STO) ($a_{\mathrm{STO}} = 3.91\,\text{Å}$).

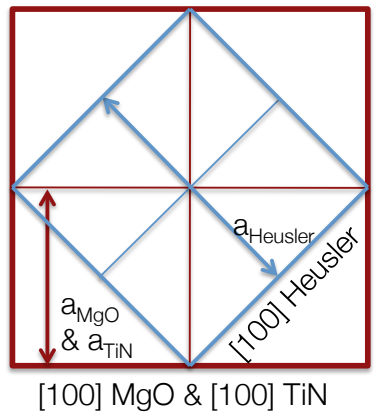

Figure 2.3. 45 degree rotated growth of the Heusler unit cell on the MgO substrate or the TiN buffer layer.

The desired tetragonal distortion of Mn-based compounds, which is necessary in order to achieve high *perpendicular magneto-crystalline anisotropy* (PMA), comes at the expense of spin-polarization. The calculated spin-polarization of the tetragonally distorted Mn_2FeGa compound, for example is 56 %, compared to the 95 % spin-polarization of the same compound in cubic structure.[30] However, due to the high PMA and low magnetization, those materials are highly promising for future technologies.

2.1.2 Magnetism of Heusler compounds

Heusler compounds provide a huge variety of magnetic phenomena, starting from ferro-, ferri- and antiferromagnetism to helimagnetism, skyrmionic systems, topological insulators and superconductors.[8, 31–35] The majority of Co-based Heusler compounds show ferromagnetic behavior, high saturation magnetization (4–5 μ_B) and low saturation fields. Ferrimagnetism in Heusler compounds often arises from antiferromagnetic coupling between atoms sitting on different positions in the unit cell, and has been mainly observed for Mn_2-based compounds (Mn_2VAl [31], Mn_2VGa [36], Mn_2PtGa [37]), especially for the tetragonally distorted structure. The advantage of ferrimagnetic ordering is the resulting low magnetic moment and with it the low stray fields, which are desired for spintronic applications. Nevertheless, the predicted and experimentally detected Curie temperatures of the ferrimagnetic Heusler compounds remain high, thus ensuring the thermal stability of the materials. Despite the fact, that all the known tetragonal Heusler compounds are

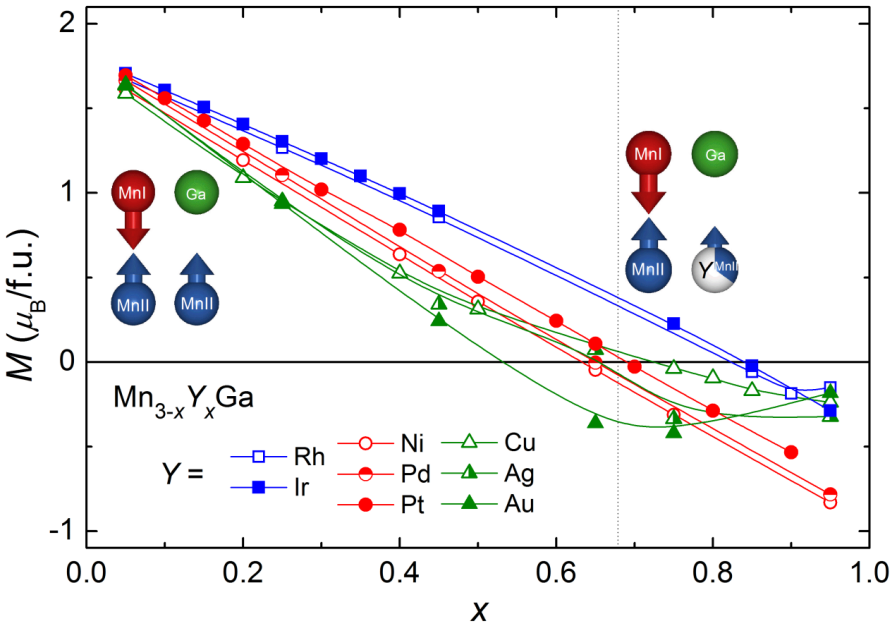

Figure 2.4. Dependence of the magnetization in $Mn_{3-x}Y_xGa$ on the substitution of Y position with a high atomic number (Z) transitional element. The different magnetic states are indicated schematically (arrows) for the corresponding compositional range. One of the magnetic sublattices is occupied by MnI (red spheres) and Ga (green spheres), MnII (blue) and the Y atoms (gray) occupy the second magnetic sublattice.[37]

ferrimagnets, none of them shows full magnetic compensation. However, according to density functional calculations, it is possible to reach the fully compensated state for $Mn_{3-x}Y_xGa$ with Y = Ru, Ni, Cu, Rh, Pd, Ag, Ir, Pt and Au, at least at $T = 0\,K$ and for a certain composition of the Heusler material (see Fig. 2.4 [37]). Hence, the investigation of the influence of inserting an additional element (doping) into the Heusler alloys, became more and more important in this research field.

2.2 Experimental methods

In this section the experimental techniques, used for the characterization of the investigated Heusler compounds are described. First, the techniques used for the determination of the crystallographic and chemical properties of the material are given. Atomic Force Microscopy, used for the investigation of surface properties and morphology of the materials are presented in the following.

The magnetic properties of the materials were investigated using manifold techniques, which are described in a separate section. The chapter is closed by the description of the experimental techniques used for the determination of the PMA of the hard-magnetic Mn-Fe-Ga and Mn-Fe-Ge compounds and the resistivity measurements. Where not explicitly mentioned, the measurements were performed **at room temperature**.

2.2.1 Sample preparation

The thin films were sputter deposited in two different sputtering machines. The BESTEC ultra-high-vacuum (UHV) sputtering system is equipped with six DC and two RF 3" sources arranged in a confocal geometry and allows co-sputtering from 4 sources simultaneously. It provides a base pressure below 5×10^{-10} mbar and deposition temperatures up to 1000 °C are possible. The sample holder allows rotation during the deposition, thus providing the possibility to increase the homogeneity of the film thickness and composition of the materials.

The LEYBOLD high vacuum (HV) sputtering chamber provides a base pressure of down to 1×10^{-7} mbar. It is equipped with five DC, one RF 4" source, as well as one DC 2" source. The samples are placed on a rotating plate, which is fixed 13 cm above the sources. Sputter deposition can only be performed from one source at a time, and only at room temperature.

2.2.2 Structural and material properties

Chemical composition analysis

The chemical composition of the investigated materials is an important characteristic, which has a strong influence on the crystallographic, magnetic and electrical properties. Two different methods were used in this work for the determination of the chemical composition: x-ray fluorescence and the ICP-OES method. A short description of these methods is given in the following.

X-ray fluorescence spectroscopy (XRF) was used, in order to determine the chemical composition of the co-sputter deposited materials, presented in this thesis: Mn-Fe-Ga, Mn-Fe-Ge and Co-Fe-Ge. The spectra were taken with an AMPTEK XR-100CR Si-PIN detector and a digital pulse processor. The detector is equipped with an Ag tube and a 250 µm thin Al primary beam filter, implemented in order to reduce the background radiation and remove the Ag L- spectral lines. The Ag tube, operating at 40 keV, irradiates the investigated materials with hard x-rays, leading to a transition of the core level electrons of the atoms in the compositions, into the K or L shells. This transition leads to the emission of a photon carrying the transition specific, and therefore also element specific, energy. The measured characteristic spectra are processed by the software, removing the contribution from the background radiation, the escape and sum peaks, and smoothing the spectra. The following evaluation of the resulting data is performed by a standardless fundamental parameter analysis [38], taking into account the filters, the atmosphere, the detector and x-ray source, as well as the setup and sample geometries. Additionally, the reabsorption and secondary fluorescence, which depend on the the film thickness and density, are taken into account based on known atomic parameters.

The measurements were performed in He atmosphere, in order to avoid the absorption of the emitted photons by the heavier atoms present in air. The used integration times of one or two hours, usually results in statistical accuracies around 1 at.%. In order to minimize the presence of diffraction peaks, the thin films were deposited on amorphous glass substrates. It is a non-destructive and quick method. The measurements can be performed without any additional treatment of the investigated sample or material, and it gives precise and reliable results, after a short integration time. However, due

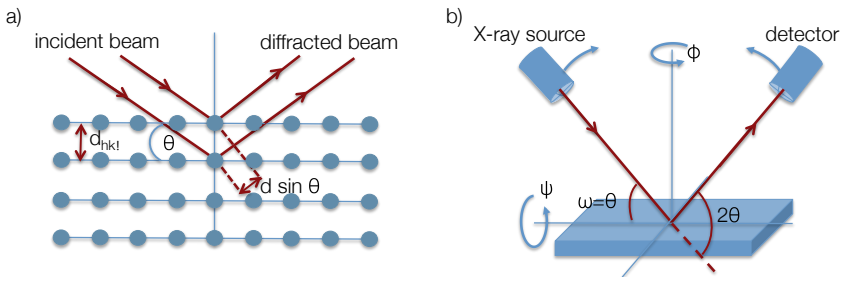

Figure 2.5. a) Sketch of the diffracted beam paths in a crystal structure. The path difference $2d \sin\theta$, where θ is the diffraction angle, results from the diffraction of the incident beam on two crystal planes with the lattice spacing d. b) Bragg-Brentano (variation of 2θ and ω) and open Eulerian cradle geometries (additional variation of ψ and ϕ) used to characterize the crystallography.

to the used Al primary beam filter, light elements (e.g. Al, Si) with transition energies below 3 keV are suppressed and, therefore, cannot be investigated.

Thus, another method was utilized in order to verify the stoichiometry of the Co_2FeAl compound, which was deposited using a composite target: **the inductively coupled plasma optical emission spectrometry (ICP-OES)** element analysis.[39] In this case, the investigated materials are dissolved in an acidic solution and introduced into an inductively coupled plasma. In this process the materials are desolved, ionized, and excited, again leading to the irradiation of characteristic emission lines, which are quantified by their intensity, similar to the XRF analysis. The ICP-OES analysis was realized by Currenta GmbH & Co. OHG.

Analysis of the crystallographic properties

The crystal structure, the density, thickness and roughness of the presented materials was analyzed using **x-ray diffraction (XRD)** and **x-ray reflectivity (XRR)** [40], performed in a Phillips X'pert Pro Diffractometer in Bragg-Brentano geometry (see Fig. 2.5). A Cu anode with a monochromator is used, emitting x-rays with the wavelength of $\lambda = 1.5419$ Å, which is a weighted average of the K_α and K_β lines.

Constructive interference of elastically scattered incident x-rays on a set of lattice planes appears, when Bragg's law is fulfilled:

$$n\lambda = 2d\sin(\theta) \tag{2.1}$$

with the diffraction order n, the crystal lattice spacing d and the diffraction angle θ (see Fig. 2.5(a)). The lattice parameters a, b and c of the investigated materials can be determined by evaluating the diffraction angles θ of the intensity peaks in the diffraction patterns, using the following relation for the lattice spacing d, which is valid for orthorhombic systems:

$$d_{hkl} = \frac{1}{\sqrt{\left(\frac{h}{a}\right)^2 + \left(\frac{k}{b}\right)^2 + \left(\frac{l}{c}\right)^2}} \tag{2.2}$$

For a cubic system, where all lattice parameters are equal, and a tetragonal system, where $a = b$, this equation simplifies accordingly. The crystal planes are labeled with the Miller indices h, k, l. The structure factor

$$F_{hkl} = \sum_{n=1}^{N} f_n(\theta) exp(2\pi(hx_n + ky_n + lz_n)) \tag{2.3}$$

includes the atomic form factors f_n, as well as the number of atoms in a unit cell with the coordinates (x_n, y_n and z_n).

For the cubic Heusler structure, consisting of four interpenetrating fcc sublattices, which are usually denoted as A, B, C and D with the associated average atomic form factors f_A, f_B, f_C and f_D, three types of reflections are possible:

- (hkl)-reflections caused by the $A2$ (unordered) crystal structure, lead to $F_{hkl} = |4[f_A + f_B + f_C + f_D]|$ with $(h+k+l)/2 = 2n$ (e.g. (022), (004),...)
- (hkl)-reflections caused by the additional order in the $B2$ crystal structure, lead to $F_{hkl} = |4[f_A - f_B + f_C - f_D]|$ with $(h+k+l)/2 = 2n+1$ (e.g. (002), (222),...)
- (hkl)-reflections caused by the additional order in the $L2_1$ crystal structure, leading to $F_{hkl} = |4\sqrt{(f_A - f_C)^2 + (f_B - f_D)^2}|$ with h, k, l all odd (e.g. (111), (113),...)

The (004) reflections, connected with the $A2$ crystal structure, are insensitive to chemical disorder and therefore called *fundamental reflections*. The additional reflexes (e.g. (002) or (111)), appearing only in cases of higher chemical order ($B2$ or $L2_1$ structure), are called *superlattice reflections*. Hence, the presence of a certain reflection in the diffraction pattern, reveals the presence of a certain crystallographic order in the investigated materials.

From the usually performed θ–2θ scans, where the x-ray source and the detector arm are moved in a plane perpendicular to the sample surface, only out-of-plane lattice can be determined. Thus, in order to determine in-plane lattice constants, e.g. of the tetragonally distorted compounds, or to investigate, if higher order reflections are present, an open Eulerian cradle was used. The Eulerian cradle makes it possible to rotate and tilt the sample and set it to a certain azimutal angle ϕ and polar angle ψ, where the higher order reflections are expected (see Fig. 2.5 (b)).

By varying the angle $\omega = \frac{2\theta}{2} + \delta\omega$, while setting the angle between the x-ray source and the detector (θ) to a diffraction peak and leaving it constant, the resulting so called *rocking curves* additionally indicate the quality of crystalline growth. The presence of crystallites, which are slightly tilted and misoriented with respect to the substrate lattice, lead to a broadening of the rocking curves. Hence, extracting their full width at half maximum (FWHM), gives information about the orientational distribution of the crystallites and the presence of mosaicity.

The density, roughness and thickness of the presented Heusler compounds were determined using **XRR** measurements.[40] In this case, the incident angles are low ($2\theta < 5°$), so that the x-rays are reflected from the surface interfaces in the sample. Total reflection occurs up to a critical angle θ_c, which is dependent on the density ρ of the material ($\theta_c \propto \sqrt{\rho}$). For higher incident angles, x-rays partly penetrate into the material, being reflected on the layers interfaces and interfering with each other and the part of the x-ray beam, that is reflected on the sample surface. The resulting observed intensity oscillates in dependence on the incident angle θ, giving information about the layer thickness and roughness. For oscillation maxima with the order m and the incidental angular position n, the layer thickness can be estimated using the following formula:

$$d \approx \frac{\lambda \cdot (m-n)}{2 \cdot (\sin(\theta_m) - \sin(\theta_n))} \tag{2.4}$$

The roughness values can be derived from the reduction of the observed intensity, which is a result of diffuse scattering of the x-rays, due to inhomogeneity and roughness of the sample surface and interfaces. For a detailed theoretical description see [40].
In order to extract the thickness, roughness and density parameters, the measured XRR curves were analyzed by numerical fitting of the reflection by using the Parratt formalism, which is used to calculate XRR curves based on optical properties of the material.[41] For this, a model of the layer stack needs to be provided, whereas the thickness, density and roughness of each single layer are fit parameters, which are varied until the calculated XRR curve coincides with the measured one.

Atomic Force Microscopy

Atomic Force Microscopy (AFM) was invented in 1986 by Gerd Binnig, Calvin Quate and Christoph Gerber.[42] Here, the interactional forces, between a sharp tip of a cantilever and the surface, are used in order to investigate the morphology of the sample surface. A sketch of this measurement technique is shown in Fig. 2.6. Depending on the distance z between the tip of the cantilever and the sample, different kinds of forces dominate: the electrostatic force for distances $z > 100\,\text{nm}$, for $100\,\text{nm} < z < 10\,\text{nm}$ the attractive capillary force occurs, smaller distances $z > 1\,\text{nm}$ lead to Van-der-Walls forces and in case of further approaching the surface, the repulsive Pauli interaction is dominant. The last two forces are commonly used for the image formation using AFM.

There are two widely used measurement modes: *contact mode* and *tapping mode*. In the contact mode, the deflection of the cantilever is directly measured using a 4-quadrant photo detector, which detects the position the laser beam, reflected on the back side of the cantilever (see Fig. 2.6). In the tapping mode, the cantilever is oscillating close to the sample surface with a frequency, close to its resonant frequency. Due to the interaction with the sample, approaching the surface leads to a change of the amplitude of the oscillation, which is again detected by the photo detector. An electric feedback control loop is used, in order to keep a constant distance between the cantilever and the sample surface. In both cases, the sample surface is scanned line by line

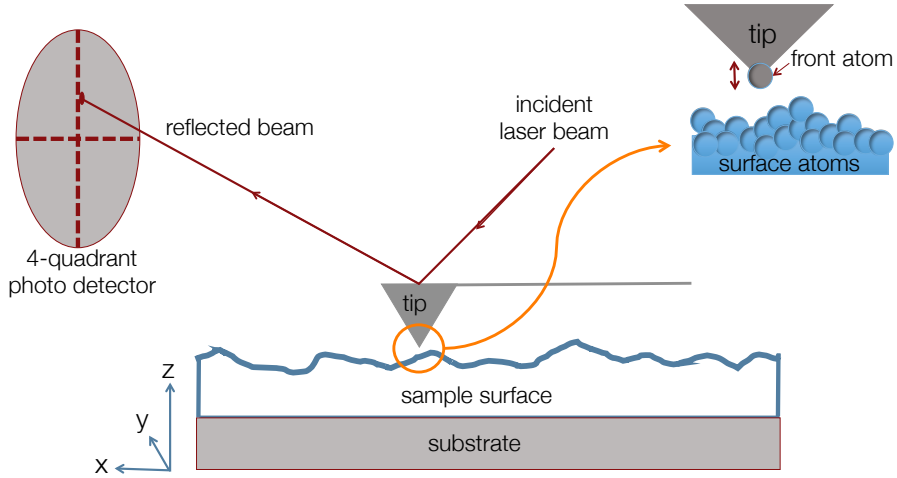

Figure 2.6. Sketch of the measurement procedure used in atomic force microscopy. A sharp tip (cantilever) approximates the surface of the investigated material and scans it line by line. The deflection of the cantilever is detected using a laser beam, reflected on the back side of the cantilever. The read-out is performed using a 4-quadrant photo detector.

(xy-direction in Fig. 2.6) along the x-axis of the sample and the deflection of the cantilever is detected as the height information (z-value) (see Fig. 2.6).

Besides of a direct observation of the surface morphology, AFM was used in oder to determine the roughness of the samples, by calculating the root mean square (rms) values using a standard deviation of surface heights:

$$rms = \sqrt{\frac{1}{N}\sum_{x=1}^{N}(z(x,y)-\overline{z}(N,M))^2} \tag{2.5}$$

with $\overline{z}(N,M)$ the arithmetic average height. The surface is described by a matrix with N lines and M columns corresponding to the points (x,y) of the height $z(x,y)$.

Thin film growth modes

In order to be able to explain and understand the surface morphology of the sputter deposited thin films, one needs to have a closer look into the possible

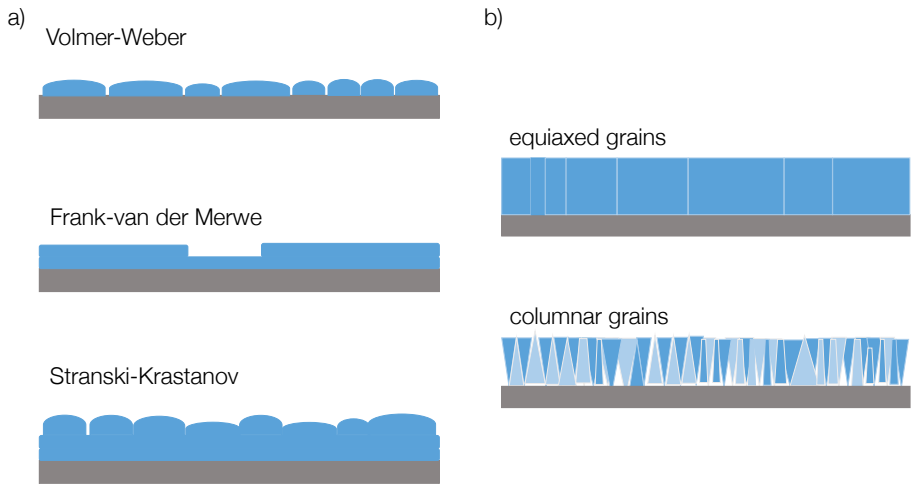

Figure 2.7. a) Scheme of the three possible growth modes, which can appear by growing the materials using sputter deposition: the Volmer-Weber-growth mode, which is the formation of 3-dimensional islands; the Frank-van der Merwe growth mode, where the material grows layer by layer (2-dimensional) and the Stranski-Krastanov growth mode, which is a mixture of the growth modes. b) The two possible grain growth modes in epitaxial films. Equiaxed grains or columnar grains can be formed, depending on the deposition temperature compared to the melting point of the deposited material.

growth modes, which can appear during the deposition processes.
There are three different growth modes, which can be distinguished: the Volmer-Weber-growth mode, which is the formation of 3-dimensional islands; the Frank-van der Merwe growth mode, where the material grows layer by layer (2-dimensional) and the Stranski-Krastanov growth mode, which is a mixture of the two previously mentioned growth modes (see Fig. 2.7 (a)).[43] The presence of a certain growth mode is primarily depending on the strength of the binding energy between the atoms and molecules of the sputtered material and their binding energy to the used substrate or buffer material. During sputter deposition mostly the Volmer-Weber growth mode appears, due to the usually higher energies of the sputtered molecules compared to the binding energy between the sputtered material and the substrate. For this

reason, sputter deposition commonly leads to the formation of polycrystalline films.[44]

Additionally, the conditions given during the deposition (e.g., deposition rate and/or temperature) lead to different grain structures. The two possible grain structures are shown in Fig. 2.7(b). The equiaxed grains are usually formed, when materials with a low melting point are sputter deposited at temperatures close to the melting point (e.g., Au, Cu, Al or Mn). For materials with a high melting temperature columnar grain structure appears (e.g., TiN).[44]

According to the observations by AFM measurements on different film thicknesses, as will be shown later, the Stranski-Krastanov growth mode is the most common growth mode of the materials presented in this theses.

2.2.3 Magnetic properties

Magneto-optical Kerr effect

The magneto-optical Kerr effect (MOKE), named after his inventor John Kerr (1877) [45], was used in order to investigate the magnetic properties of Co_2FeAl and Co_2FeGe. The Kerr-effect describes the change of the polarization plane of linearly polarized light, that is reflected on the surface of a magnetized sample.

The measurements were performed employing two different systems (see Fig. 2.8(a) and (b)). One system provides magnetic fields up to 300 mT, which can be applied perpendicular or parallel to the sample surface. The sample is mounted parallel to the incident laser beam, on a sample holder, which is mounted on a three dimensional xyz-translation table. The sample holder can be rotated automatically during the measurements by a step motor and adjusted to the right position between the magnetic poles. A more detailed description of the used setup is given in [46].

There are three basic types of MOKE, depending on the orientation between the incident light and magnetization with respect to the sample surface: The polar contribution (PMOKE) is a result of the out-of-plane oriented magnetization component (perpendicular to the sample surface), the longitudinal contribution (LMOKE), appears in case if the magnetization M of the sample is parallel to the incident light and to the sample surface and transversal MOKE,

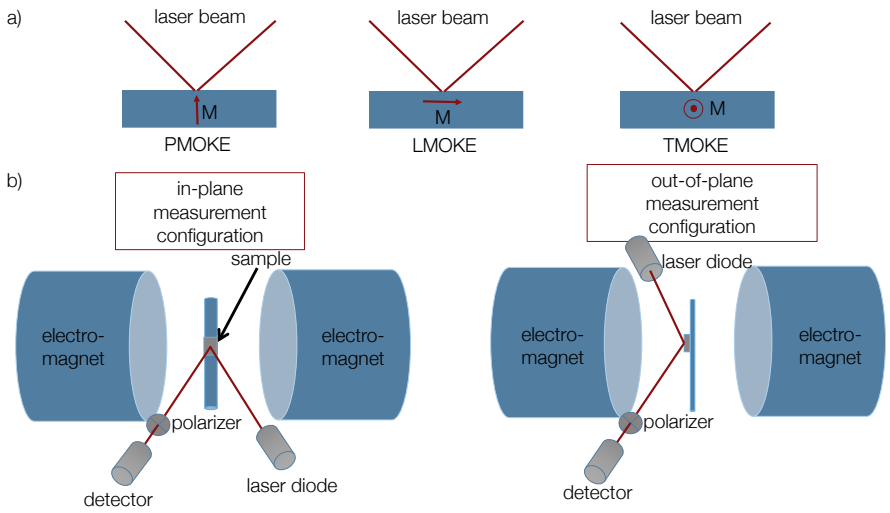

Figure 2.8. a) The three types of MOKE observed using the vectorial MOKE setup. The magnetic field can be applied perpendicular or parallel to the sample surface. Two detectors in different geometry, measure the PMOKE and LMOKE contribution simultaneously. b) MOKE setup, providing magnetic field up to 2 Tesla. The sample can be mounted parallel or perpendicular to the applied magnetic field.

which occurs if the magnetization is perpendicular to the incident plane of light and parallel to the sample surface (see Fig. 2.8(a)). In the vector MOKE system, two detectors in different geometry (45° and 0° relative to the surface normal of the sample) were used to detect the MOKE signal. The used laser wavelength is λ=488 nm. By applying the magnetic field perpendicular and parallel to the sample surface the coercivity and easy axis of magnetization can be determined.

The second MOKE system provides magnetic fields up to 2 Tesla. The sample is mounted on a sample holder in the centre of the setup and can be manually placed parallel or perpendicular to the magnetic field, as shown in Fig. 2.8(b). In both orientations the angle between the laser and the surface normal is around 60°. The used laser wavelength in this MOKE setup was λ=635 nm.

Vibrating Sample Magnetometry

The vibrating sample magnetometer (VSM) was introduced in 1959 by Simon Foner.[47] Here, the induced induction, generated by the magnetic moment of a sample, vibrating in a uniform magnetic field, is detected.

The used setup is embedded in a closed cycle He-cryostat with integrated superconducting coils, which provide magnetic fields up to 7 Tesla. The sample is mounted on a non-magnetic sample holder, which is centered between two pick-up coils and can be moved sinusoidally. The geometry and number of the used pick-up coils can also be adjusted to the individual needs, as described in [48]. The signal is detected as a periodic induction voltage, resulting from the changes of the magnetic flux through the coils, due to the vibrating magnetic dipole. Lock-In amplifiers are used for the detection of the magnetic moments, leading to a sensitivity of about 1 μemu.

Due to the high possible magnetic fields, the VSM measurements were in particular carried out for the hard magnetic Mn-Fe-Ge compound.

Alternating Gradient Magnetometry

Alternating gradient magnetometry (AGM) was partly used for the determination of the magnetic moments of the investigated materials. The method was introduced after the previously described VSM by P. J. Flanders in 1988 and provides higher sensitivity, which can exceed 10^{-8} emu.[49] The sample is attached with grease to the thin glass fibre sample holder, which incorporates a piezoelectric element. A DC field is used in order to magnetize and demagnetize the samples. An alternating gradient field is applied to the sample simultaneously, exerting a force, which is proportional to the field gradient and the magnetic moment of the sample. The resulting mechanical deflection of the sample holder is detected as a voltage output of the piezoelectric element. The signal was amplified, by operating close to the mechanical resonance frequency of the sample holder (quartz fibre). A translational XYZ-stage was used, in order to position the magnetic material precisely in the centre of the alternating gradient field coils and the magnets. This is especially important when measuring a material with low coercive field, since the AC field, caused by the gradient coils, increases with increasing offset along the gradient axis, and thus, can influence the magnetization of the non-centered sample.[49]

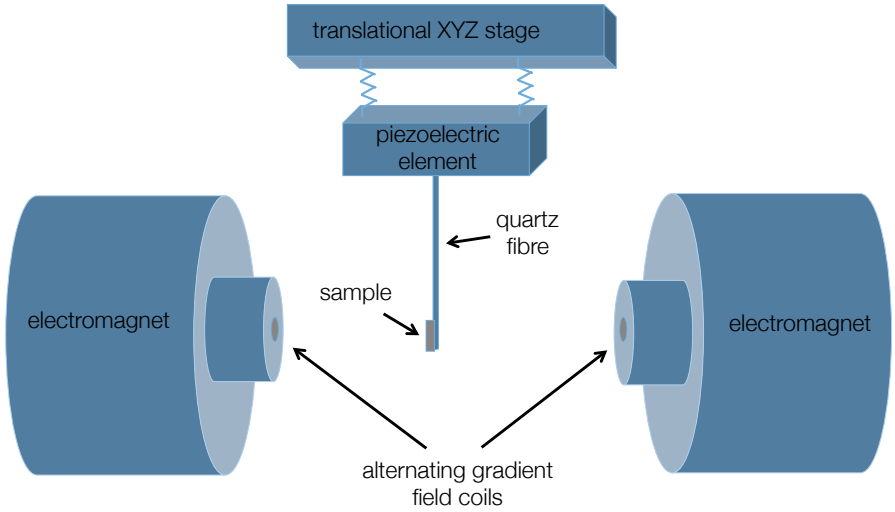

Figure 2.9. Sketch of the used AGM setup. The sample is mounted with grease to the thin glas fibre sample holder, which incorporates a piezoelectric element and can be centered by the translational XYZ-stage between the gradient coils and the magnets. An alternating gradient field is applied, leading to a deflection of the sample holder, due to the interaction with the magnetic material. The deflection is detected as a voltage output of the piezoelectric element, which is connected to the sample holder.

Since the maximal possible magnetic field, provided by this system, is 14 kOe, the samples with low coercive fields were investigated using the AGM. A sketch of the measurement setup is shown in Fig. 2.9.

X-ray Absorption and X-ray Circular Dichroism

X-ray absorption spectroscopy (XAS) and x-ray magnetic circular dichroism (XMCD) measurements were performed at the Beamline 4.0.2 of the Advanced Light Source (Berkeley, CA, USA). X-ray spectroscopy provides quantitative information about the local structure, the magnetic properties of the samples, as well as the shape of the valence and conduction bands.[1] XAS and XMCD measurements were used, in order to investigate the element specific magnetic behavior of the materials.

The incident beam of monochromatic soft x-rays (100 eV to 2000 eV) penetrates into the sample and interacts with the core level electrons of the

contained elements. The ejected photoelectrons, the photons generated by the interaction between the x-rays and the sample or the transmitted beam, are analyzed. Grounding the sample and measuring the resulting drain current resulting from the photoemission, is called the total electron yield (TEY) technique. Due to the limited mean free path of the electrons in the material, this technique is surface-sensitive (2–5) nm. Another possibility is to detect the fluorescence photons, which are emitted due to the interaction with x-rays. In this case, a photo diode is placed behind the sample, converting the incoming photons to a current. The so called luminescence mode (LM) is sensitive to the whole sample volume. In this work only the TEY measurements are shown and analyzed.

The XMCD spectroscopy uses the difference in the absorption of circularly polarized light, in dependence on the orientation of its helicity to the magnetization direction of the absorbing material. Due to the spin-orbit coupling, the incident photons transfer their angular momentum to the orbital and spin momentum of the photoelectrons, which is transferred to an unoccupied state above the Fermi level. Hence, this method is one of the few ways to determine the spin and orbital moment of the elements in the sample independently, together with the use of magneto-optical sum rules.[50] For the calculations, the XA intensities were normalized to the direct beam intensity and to the post edge jumpheight of $\eta = 1$. A detailed description of the used sum rule analysis is given in [51]. A detailed review on the XMCD measurement technique is given in [52].

Anomalous Hall Effect

The anomalous Hall effect (AHE) was discovered by Edwin Herbert Hall in 1879. During his investigations on 3d-ferromagnets Co, Fe and Ni he found, that the measured Hall voltage $U_{\mathrm{AHE}} = U_{xy}$ is strongly correlated with the magnetization of the material.[53] After this discovery, in 1954 Karpus and Luttinger delivered the first explanation for the AHE and proposed it to be a result of the spin-orbit interaction and inter-band mixing of the spin polarized electrons in ferromagnets.[54] Currently, the AHE is explained through the concept of Berry-phase [55], which is an intrinsic and band structure related mechanism, as well as through the extrinsic mechanisms of skew-scattering and side-jump.[56, 57] Both extrinsic mechanisms are a

result of spin dependent asymmetric scattering of the spin polarized electrons on phonons and impurities in the crystal lattice.

The anomalous Hall effect measurements were performed in a closed cycle He^4-cryostat. The superconducting coils of this system, provide magnetic fields up to 4 Tesla. The temperature can be varied in the range of 300 K to 2 K. The magnetic field $\vec{B}$ was applied perpendicular to the film plane (see Fig. 2.10(b)) and strong enough to saturate the films magnetically. The magnetic films were patterned into Hall-bars (see Fig. 2.10(c)) using UV-lithography and Ar-ion etching. Thin Ta/Au contacts (5 nm Ta and 30 nm Au) were sputter deposited on top of the patterned Hall-bars, in order to provide the connection (via Au wire bonds) to the chip carriers, which were implemented into the sample holder of the cryostat. An AC current of 100 µA was applied in-plane to the sample surface (x-direction), using contacts 1 and 2 (see Fig. 2.10(c)). The Hall voltage U_{xy} was detected transversal to the current direction (y-direction). Additionally the resistivity of the sample was measured, using contacts, parallel to the current direction.

The resistivity ρ was calculated using the following formula:

$$\rho = \frac{U_{xx} \cdot w \cdot d}{L \cdot I} \tag{2.6}$$

with the measured longitudinal voltage U_{xx}, the applied current $I = 100\,\mu$A, the film thickness d and the Hall-bar width $w = 1.2$ mm and length $L = 3$ mm.

The **anomalous Hall resistivity** can be deduced from the measured Hall voltage U_{xy} through:

$$\rho_{xy} = \frac{U_{xy} \cdot d}{I} \tag{2.7}$$

The Hall-resistivity of a ferromagnet is a sum of the contribution from the ordinary Hall effect ρ_{OHE} and the anomalous Hall effect contribution ρ_{AHE}. Thus, it is:

$$\rho_{xy} = \rho_{\mathrm{OHE}} + \rho_{\mathrm{AHE}} = R_0 B_z + R_S M_z \tag{2.8}$$

with the Hall coefficient R_0, which scales linearly with the out-of-plane component of the applied magnetic field B_z and the anomalous Hall coefficient R_S, which scales linearly with the out-of-plane component of the magnetization M_z. The anomalous Hall effect contribution ρ_{AHE} dominates in the low field area. After reaching the saturation of the magnetization, the Hall voltage reveals a slight linear increase, which can be attributed to the ordinary Hall

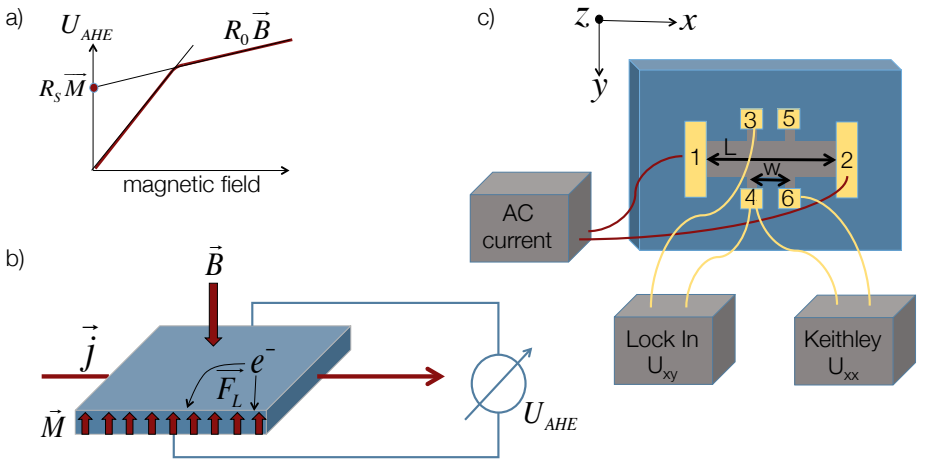

Figure 2.10. a) Sketch of the Hall resistivity curve for a ferromagnet. The Hall voltage U_{AHE} increases linearly with increasing magnetic field and reaches a saturation value, when the magnetization is saturated. Further increase or decrease of the Hall voltage after reaching the saturation, can be attributed to the contribution of the ordinary Hall effect. b) Schematic overview of the AHE measurement. c) Sketch of the measurement setup used for the AHE measurements.

effect contribution ρ_{OHE}. Thus, the Hall coefficient R_0 can be extracted from a linear fit to the measured Hall voltage in the high field area, as shown in Fig. 2.10(a).

In order to address the possible misalignment of the contacts on the sample surface, the Hall resistivity ρ_{xy} was calculated as follows:

$$\rho_{xy}(\vec{B}) = \frac{\rho_{xy}(\vec{B}_{\downarrow}) + \rho_{xy}(\vec{B}_{\uparrow})}{2} \tag{2.9}$$

with $\rho_{xy}(\vec{B}_{\downarrow})$ and $\rho_{xy}(\vec{B}_{\uparrow})$, the magnetic field sweep from +4 T to −4 T and −4 T to +4 T, respectively. Beside the observation of switching behavior, AHE measurements were used to determine the Hall constant values R_0, the charge carrier densities n and mobilities μ, which play an important role for the characterization of the electrical behavior of the material. The presence of linear Hall voltage in the AHE measurements at high fields (see Fig. 2.10(a)) is attributed to the ordinary Hall effect. The slope $\frac{\Delta U_{\mathrm{AHE}}}{\Delta B}$ of the linear fit to the

measured Hall voltage U_{AHE} gives the Hall constant by using the following formula:

$$R_0 = \frac{\Delta U_{\mathrm{AHE}}}{\Delta B} \cdot \frac{d}{I} \tag{2.10}$$

with B the magnetic field, d the layer thickness and I the applied current.

With the calculated Hall constant and the measured resistivity ρ, the charge carrier density n and mobility μ were determined using the formula:

$$n = -\frac{1}{R_0 \cdot e} \tag{2.11}$$

and

$$\mu = \frac{1}{\rho \cdot e \cdot n} \tag{2.12}$$

where e is the elementary charge.

2.2.4 Determination of perpendicular magnetic anisotropy

The uniaxial perpendicular anisotropy energy K_{u} is obtained using the relation

$$K_{\mathrm{u}} = \frac{\mu_0 H_{\mathrm{K}} M_{\mathrm{S}}}{2} \tag{2.13}$$

with the vacuum permeability constant μ_0, the anisotropy field H_{K}, defined as the field needed to saturate the magnetization in the magnetic hard direction, and the saturation magnetization M_{S}.[1] However, the investigated Mn-based compounds showed hard magnetic behavior and strong anisotropy, so that it was not possible to saturate these compounds in the direction of magnetic hard axis. Even at 7 T applied field saturation could not be reached, which is why another approach was applied in order to calculate the perpendicular anisotropy energy K_{u}.

The assumption of a homogeneously magnetized sample and torque equilibrium ($\tau_{\text{Zeemann-energy}} + \tau_{\text{anisotropy}} = 0$) [1], leads to the following equation:

$$B_{\mathrm{ext}} M_{\mathrm{S}} \sin(\alpha) - 2K_{\mathrm{u}} \sin(\psi)\cos(\psi) = 0 \tag{2.14}$$

$$\Leftrightarrow \quad B_{\mathrm{ext}} M_{\mathrm{S}} \sin(\alpha) = K_{\mathrm{u}} \sin(2\psi) \tag{2.15}$$

with B_{ext} the external magnetic field; M_{S} the saturation magnetization; K_{u} the uniaxial anisotropy energy constant and α: the angle between the magnetization M and the external field. The angles ψ and θ are illustrated in

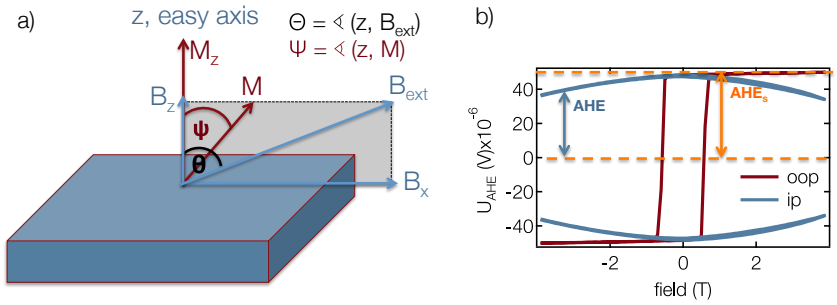

Figure 2.11. a) Measurement configuration for the determination of the anisotropy energy K_u. B_{ext}, B_x and B_z give the applied external magnetic fields. M is the direction of the resulting tilted magnetization out of the easy axis direction M_z. b) The normalized in-plane (blue) and out-of-plane (red) AHE measurement curves. The signal-height at zero field is the saturation value AHE_s. The signal changes (marked as AHE) with increasing field (applied 90 degree to the easy axis) (in-plane measurement), resulting from the tilt of the magnetization out of the easy axis.

Fig. 2.11(a). The anomalous Hall voltage in saturation (AHE_s) is given, when the sample is saturated in the easy axis of the magnetization (perpendicular to the film plane). By applying a field ($B_x = B_{ext}$) in direction of the magnetic hard axis, the magnetization can be slightly tilted away from the easy axis, leading to a decrease of the Hall voltage AHE (see inset in Fig. 2.11(b)). Since ψ is the angle between the actual magnetization direction and the easy axis of the magnetization, it can be calculated using $\psi = \arccos(\frac{M}{M_s}) = \arccos(\frac{AHE}{AHE_s})$. The angle between the surface normal and the external magnetic field is set to $\theta = \arctan(\frac{B_x}{B_z})$. According to this, α is the difference between θ and ψ. Implementing this into the equation 2.15, the anisotropy energy can be calculated using:

$$\frac{K_u}{M_s} = \frac{B_{ext}\sin(\theta - \psi)}{\sin(2\psi)} \tag{2.16}$$

Accordingly, the slope of a linear fit of $|B_{ext}|\sin(\theta-\psi)$ plotted against $\sin(2\psi)$ gives the relation of $\frac{K_u}{M_s}$. Knowing the saturation magnetization M_s, it is possible to determine the anisotropy energy K_u.

2.2.5 Resistivity measurements

Besides the anomalous Hall effect measurements, the 4-terminal method was used in order to determine the resistivity of the thin films.[58] In this method, 4 contact needles are placed on the sample surface. The resistivity of the films can be determined using the measured voltage U, the applied current values I and the film thickness d with the following equation:

$$\rho = \frac{U}{I} \cdot \frac{\pi d}{ln(2)} \tag{2.17}$$

This method is valid in presence of a constant layer thickness, under the assumption of infinitesimal contact areas and an equidistant positioning of the contacts. [58]

Chapter 3

Mn-based Heusler compounds

Fully spin polarized, ferrimagnetic, materials attracted a lot of interest in the recent years due to their possible application in nonvolatile memories and field programmable logic devices. The low magnetic moment, resulting from the ferrimagnetic ordering of the atomic magnetic moments in the investigated compounds, together with the resulting low stray fields, are desired for spintronic applications. Additionally, materials with perpendicular magneto-crystalline anisotropy, which is important in order to maintain the thermal stability at shrinking device sizes, are in the focus of scientific research.
For this purpose, detailed characterization of the ternary compounds $Mn_{4-x}Fe_xGe$ with ($0.3 \leq x \leq 1$) and Mn-Fe-Ga was carried out and is presented in this chapter. The investigations focus on the influence of deposition processes, composition and the used substrates on the crystallographic, magnetic and electrical properties of the compounds. The aim of reaching almost compensated ferrimagnetism, combined with high perpendicular magnetic anisotropy was achieved for both materials. The high roughness and Stranski-Krastanov growth mode of the Mn-based compounds is challenging in view of the applicability of these materials in future logic and memory devices. Therefore, the influence of a buffer layer (TiN) on the film growth and an additional deposition procedure (2-step process) were investigated.

3.1 Introduction

In order to realize energy-efficient spin-torque devices, as for example high-density magnetic recording media, the search for suitable materials is still ongoing. The requirements on the materials properties are very demanding. High Curie temperatures should be provided in order to maintain functionality at least at room temperature. Strong perpendicular uniaxial anisotropy K_u is needed in order to achieve thermal stability in a time frame of 10 years. Low magnetization values lead to a reduction of stray fields and thus reduce the sensitivity to disturbances. Low magnetic damping constant α and high spin polarization are necessary in order to enable high switching frequencies and effect amplitudes, when using the materials in spintronic devices.[5, 6]

For this reason, the tetragonally distorted Heusler compounds have attracted great interest in the field of spintronics. Mn-based Heusler compounds are promising candidates, providing all of the required properties, which is why extensive research on this material class has been performed and is still ongoing, where $Mn_{3-x}Ga$ is the most popular and very well investigated compound.[18–21, 59–62]. It is a ferrimagnetic material, which was shown to provide high spin polarization and out-of-plane magnetization direction (measured for $Mn_{3-x}Ga$ ($0.15 \leq x \leq 2$).[18–20] The magnetic behavior of $Mn_{3-x}Ga$ can be tuned by adding an additional element to the compound. Fe doped Mn-Ga is calculated to be 95 % spin polarized at the Fermi level for the cubic phase (Mn_2Fe_1Ga).[30] This, combined with the predicted low total magnetization $M = 1.03\,\mu_B$/f.u. [30] and high Curie temperature $T_C = 550\,K$ (lowest measured value for $Mn_{1.4}Fe_{1.6}Ga$) make this material promising to serve as an electrode in magnetic tunnel junctions (MTJ's).[63] However, no detailed experimental results, regarding the influence on the structure or the magnetic properties, for Fe doped Mn-Ga are present in literature and thus are investigated in this work. Substituting Fe for Mn leads to an enhancement of the magnetic moment. The measured magnetic moment of pure Mn_3Ga (prepared by arc melting) is $1\,\mu_B$/f.u. The Fe-rich Fe_2Mn_1Ga shows the highest magnetic moment of $3.5\,\mu_B$/f.u. among all Fe doped Mn-Ga compositions.[63] The transition from the cubic $D0_3$ into the tetragonal $D0_{22}$ phase takes place at deposition temperatures above 500 °C.[61] Hence, the

choice of the right deposition temperature is an important criterion in terms of the crystallographic properties and will be addressed in this chapter.

Recently $Mn_{3+x}Ge$ also attracted the interest of the researchers, due to its small magnetic moment, which was predicted for the tetragonally distorted structure (73 kA/m [64]), owing to almost compensated ferrimagnetism, combined with sharp magnetization switching, large perpendicular magnetic anisotropy ($> 2.29\,MJ/m^3$) and low damping constant ($\alpha = 9 \cdot 10^{-4}$).[22] The reported Curie temperature value is high ($> 865\,K$) [65] and the calculations of the spin-dependent density of states for the $D0_{22}$ Mn_3Ga and Mn_3Ge revealed, that the Fermi level E_F is located below the pseudo gap for the majority spin states for Mn_3Ga, whereas, due to the higher number of valence electrons, E_F lays in the pseudo gap for Mn_3Ge. Adding valence electrons to the material shifts the Fermi level in the minority spin state of Mn_3Ge into the band gap above the Δ_1 band, leading to a fully spin polarized Δ_1 band at E_F.[22] The fully spin-polarized Δ_1 bands make $Mn_{3+x}Ge$ even more promising compared to $Mn_{3-x}Ga$, where the spin polarization is reported to be around 40% to 58%.[22, 23, 64, 66–68]

This work focuses on the investigation of Fe doped $Mn_{4-x}Ge$. Theoretical calculations predict $Fe_{3-x}Mn_xGe$ ($0.25 < x < 2.75$) to be ferrimagnetic with a spin polarization of P=94% in the tetragonally distorted phase.[69] According to the calculations of Wollmann et al. for Mn_2FeGe, this compound provides low magnetization of $-0.06\,\mu_B$ per formula unit (f.u.) for a tetragonality of c/a = 2.05 and an out-of-plane lattice constant of $c = 7.42$ Å.[70]

Targeting the use of these materials as magnetic electrodes in MTJs, adjacent conductive layers are needed, which act as an electric lead. In case of a Heusler bottom electrode, the conducting underlayer has to act as a seed layer for the Heusler, allowing high-quality crystalline growth. Thus, TiN was investigated as a possible seed-layer. Sputter deposited TiN exhibits low electrical resistivity (16 μΩ cm) and a surface roughness below 1 nm.[71, 72] Thus, it provides a good electrical connection to the MTJ. High thermal (melting point 2950 °C [44]) and chemical stability, which prevents chemical reactions of TiN with the on top deposited material, are another benefit of TiN as a seed-layer. The lattice constant of TiN (fcc structure) is 4.24 Å and therefore suitable for various Heusler compounds. It was already shown, that TiN is a suitable seed-layer for $Mn_{3-x}Ga$ and Co_2FeAl.[73]

3.2 The ternary $Mn_{4-x}Fe_xGe$ compound

The influence of **Fe** doping on the structural, magnetic and electrical properties of the **$Mn_{4-x}Ge$** compound was investigated, focusing on $Mn_{4-x}Fe_xGe$ ($0.3 \leq x \leq 1$), since the tetragonally distorted structure was only achieved in this stoichiometry range. It is shown that $Mn_{4-x}Fe_xGe$ combines the required properties to serve as an electrode in high-density STT-MRAM applications. This section is based on Niesen et al.[74].

Preparation

The $Mn_{4-x}Fe_xGe$ thin films were deposited in the BESTEC sputtering chamber. DC magnetron co-sputtering from pure Mn, Fe and a Ge targets was used to prepare the samples, in Ar atmosphere at a pressure of 1.7×10^{-3} mbar. Mn-Fe-Ge series with $Mn_{2-x}Fe_xGe$, $Mn_{3-x}Fe_xGe$ and $Mn_{4-x}Fe_xGe$ were realized by varying the power values applied to the targets during sputtering. The sample stoichiometries were determined using x-ray fluorescence (XRF) spectroscopy, measured on 40 nm thin Mn-Fe-Ge films.

The tetragonally distorted structure has been formed for the $Mn_{4-x}Fe_xGe$ with $0.3 \leq x \leq 1$. Therefore, our studies focus on this composition range. The optimum deposition temperature to achieve the tetragonally distorted phase was determined to be above 405 °C. Therefore the thin films were deposited at 405 °C or 450 °C, depending on the prior determined crystallization temperature of the specific stoichiometry. On top of the Heusler compound a 2 nm thick Si layer was deposited to prevent the material from degradation. The thin films were deposited on MgO (100) ($a_{MgO} = 4.21$ Å) single crystalline substrates, in order to investigate the compatibility of this material to MgO, which is commonly used as barrier material in magnetic tunnel junctions.

3.2.1 Structural properties

A sketch of the atomic positions in the tetragonally distorted $D0_{22}$crystal structure of $Mn_{4-x}Fe_xGe$ compound, is shown in Fig. 3.1. Similar to the $L2_1$ structure, the atomic occupation of the $D0_{22}$ follows certain rules.[75] The Mn atoms occupy two different Wyckoff positions: Mn_I is sitting at the 2b

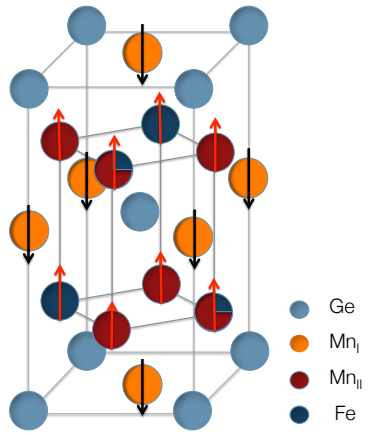

Figure 3.1. Sketch of the tetragonally distorted crystal structure ($D0_{22}$) of the ferrimagnetic $Mn_{4-x}Fe_xGe$ compound. Wyckoff position 2a is occupied by Ge (light blue spheres), Mn_I occupies positions 2b (orange spheres) and Mn_{II} (red spheres) is sharing the 4d position with the Fe atoms (dark blue spheres).

(0, 0, 1/2) position and Mn_{II} occupies 4d (0, 1/2, 1/4). According to the electron occupation rule,[75] Fe will preferably occupy the 4d position, since it possesses more electrons than Mn. Depending on the Fe content in the sample, the 4d position therefore will be shared between the two elements (Mn and Fe). Ge, as the main group element, occupies the 2a (0, 0, 0) Wyckoff position (cf. Fig. 3.1).

XRD patterns of 20 nm thin Mn-Fe-Ge films (Fig. 3.2(a)) reveal the fundamental (004) reflex of the $D0_{22}$ structure for all investigated stoichiometries, thus confirming the epitaxial growth ([001] direction) of the deposited material. Additionally the patterns show a reflection near $2\theta = 70°$, which is identified as the (220) reflection of the Mn-Fe-Ge, showing that a small amount of the material does not grow epitaxially. The superlattice (011) line was detected at $2\theta = 26°$ ($\psi = 61°$and $\phi = 0°$), where $\phi = 0°$ corresponds to $[100]_{MgO}$, revealing $D0_{22}$ ordering of the compound.

Pole figures of the (011), (112) and (004) reflections are depicted in Fig. 3.2(d) and reveal the texture of the Mn-Fe-Ge films. Due to the four-fold symmetry imposed by the cubic substrate, the ϕ-range of the pole-figure measurements was limited to $0 \leq \phi \leq 180°$. From the (011) and (112) pole-figure plots the in-plane crystallographic orientation can be determined to $[100]_{\text{Mn-Fe-Ge}} \parallel [100]_{MgO}$. In the (004) pole-figure the intensity distribution up to $\psi = 10°$ around the [100]MgO direction is shown. The maxima are at $\psi \approx 5°$ and $\phi = 45°$ which indicates that the compound nucleates slightly misoriented to the substrate lattice. Therefore, mosaicity might be present in

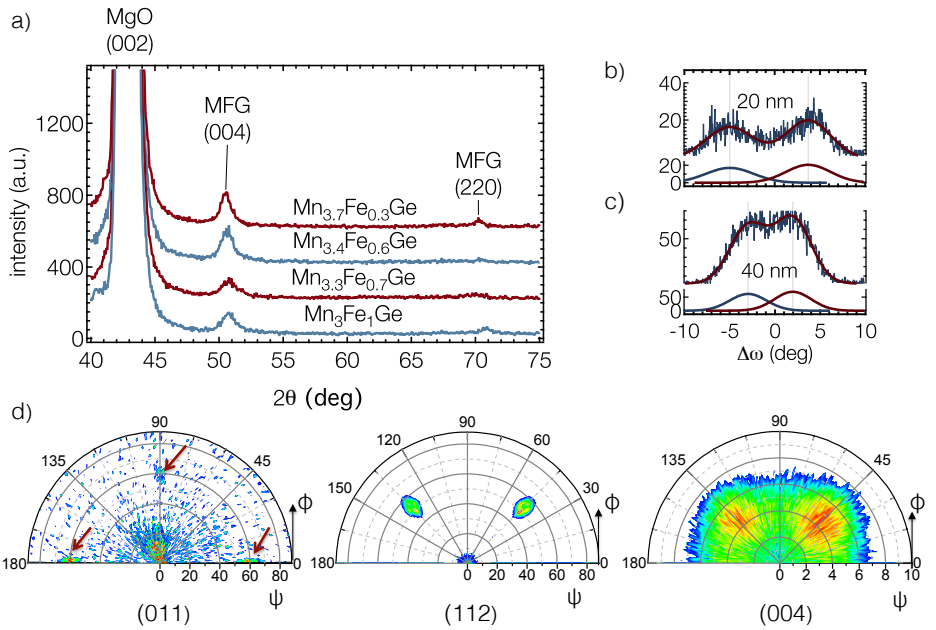

Figure 3.2. a) X-ray diffraction patterns of the $Mn_{4-x}Fe_xGe$ compounds. For the 20 nm thin films the fundamental (004) diffraction peak and the (220) reflection of the tetragonally distorted structure are observable. b) Rocking curve of the (004) peak for 20 nm thin $Mn_{4-x}Fe_xGe$ (here exemplarily shown for $Mn_{3.3}Fe_{0.7}Ge$). c) Rocking curve of the (004) peak for 40 nm thin $Mn_{4-x}Fe_xGe$. d) Pole figures of the (011), (112) and (004) reflections. From rocking curves, showing double peaks, and the (004) pole figure it can be concluded, that four equivalent c-axis orientations exist, which are tilted by few degree from the (001)-MgO direction. The presence of the (011)-peak confirms the $D0_{22}$ structure. The (112)-peak reveals epitaxial growth and the in-plane orientation of the compound.

these films, leading to increased stress and imperfections. A more detailed investigation of the (004) reflection, using rocking curves for 20 nm and 40 nm thicknesses (see Fig. 3.2(b) and (c)) revealed, that the distance between the two maxima is reduced with increasing film thickness (from 8.7° to 4.95°), indicating that the misalignment is caused by high lattice mismatch between the substrate and the compound ($\frac{a_{MgO}-a_{MFG}}{a_{MgO}} = 9.5\%$). With increasing thickness, the influence of the substrate reduces as the lattice of the compound relaxes.

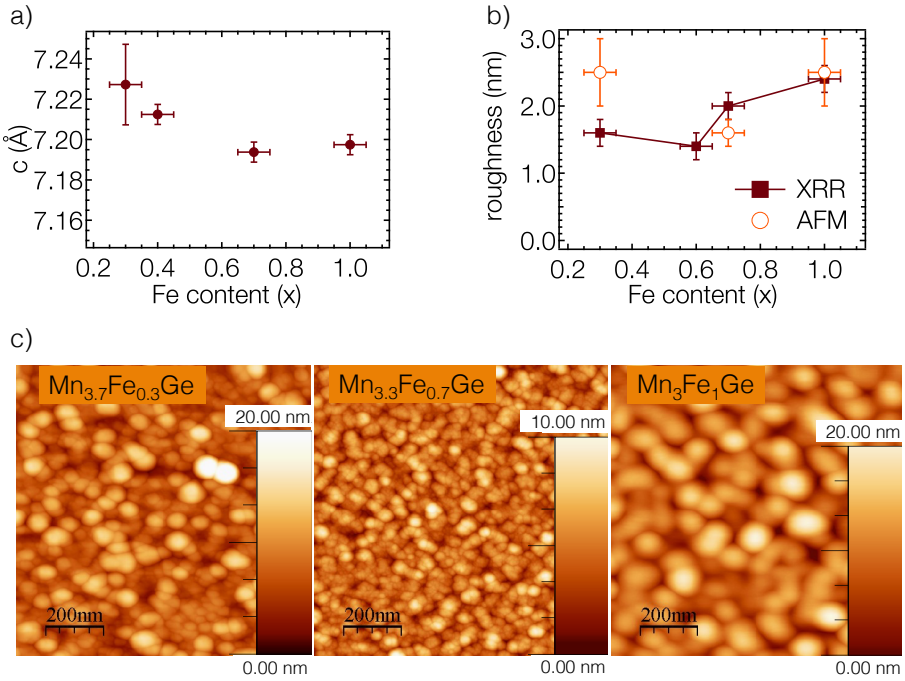

Figure 3.3. a) Lattice constant c of the Mn-Fe-Ge thin films in dependence on the stoichiometry. The lattice constant values were calculated using the position of the (004) reflection, showing that the lattice constant decreases with increasing Fe content. b) Roughness values determined using XRR and AFM measurements. c) $1\,\mu m^2$ AFM scans for three different $Mn_{4-x}Fe_xGe$ stoichiometries. The minimum roughness of (1.6 ± 0.2) nm was achieved for $Mn_{3.3}Fe_{0.7}Ge$.

The out-of-plane lattice constant, calculated from the position of the (004) fundamental peak, slightly varies in dependence on the Fe content (see Fig. 3.3(a)). $Mn_{3.7}Fe_{0.3}Ge$ showed the highest value of $7.23\,Å \pm 0.02\,Å$ The lowest value of $7.19\,Å \pm 0.01\,Å$ was determined for $Mn_{3.3}Fe_{0.7}Ge$. The in-plane lattice constant was exemplarily measured for these two stoichiometries using the position of the (112) line, measured at $2\theta = 41.5°$, the polar angle $\psi = 53°$ and the azimuthal angle $\phi = 45°$. The calculated in-plane lattice constant is $3.81\,Å \pm 0.01\,Å$ for both stoichiometries.

The roughness values of Mn-Fe-Ge, extracted from XRR measurements, are shown in Fig. 3.3(b). It should be noted that the roughness is around

Table 3.1. Summary of the magnetic properties of Mn-Fe-Ge extracted from out-of-plane magnetization and AHE hysteresis loops. The magnetization values M_S and M_{tot} are determined from the contribution of the hard magnetic phase.

$Mn_{4-x}Fe_xGe$	$\mu_0 H_c$ (T)	S_R	M_S (kA/m)	$M_{tot}(\mu_B/f.u.)$	K_u (MJ/m^3)
x = 1	1.61 ± 0.05	0.9	72 ± 7	0.16 ± 0.02	0.30 ± 0.03
x = 0.7	1.83 ± 0.05	0.94	64 ± 6	0.14 ± 0.01	0.36 ± 0.04
x = 0.6	2.58 ± 0.05	0.9	35 ± 3	0.08 ± 0.01	0.26 ± 0.03
x = 0.3	3.64 ± 0.05	0.72	38 ± 4	0.09 ± 0.01	- -

2 nm independent on the stoichiometry and thickness, which is an important parameter for the implementation of this material into magnetic tunnel junctions (MTJs). High roughnesses of the bottom electrode, leads to high roughness of the thin (≈ 1 nm) isolating barrier material, e.g. MgO, thus leading to short cuts (pin-holes) through the tunneling barrier and shunting of the tunneling-magneto-resistance (TMR) effect.

A more detailed investigation of the surface morphology was performed using AFM (see Fig. 3.3(b) and (c)). The determined rms roughness values are in agreement with the roughness determined using XRR. For Mn_3Fe_1Ge and $Mn_{3.7}Fe_{0.3}Ge$ the roughness is (2.5 ± 0.5) nm, which is probably a result of polycrystalline growth (grains of 100 nm and 150 nm) and deep trenches between neighboring grains. $Mn_{3.3}Fe_{0.7}Ge$ showed lower grain size and roughness of (1.6 ± 0.2) nm.

The density of Mn-Fe-Ge (extracted from XRR measurements) is 7.5 g/cm^3 for samples with ($0.4 \leq x \leq 1$) and slightly lower (7.4 g/cm^3) for Mn-Fe-Ge with the lowest Fe content ($x = 0.3$), which is in good agreement with the bulk density value reported for $Mn_{3+x}Ge$ (7.46 g/cm^3).[76]

3.2.2 Magnetic properties

The magnetic and electrical properties for $Mn_{4-x}Fe_xGe$ were investigated using the vibrating sample magnetometer (VSM) and the anomalous Hall effect measurements (AHE). Figure 3.4(a) shows a comparison of the hysteresis curves measured using VSM and AHE. The coercive fields of the compounds are in good agreement for both measurement techniques, but there is a noteworthy difference around 0 T field, between the VSM and the AHE measurements.

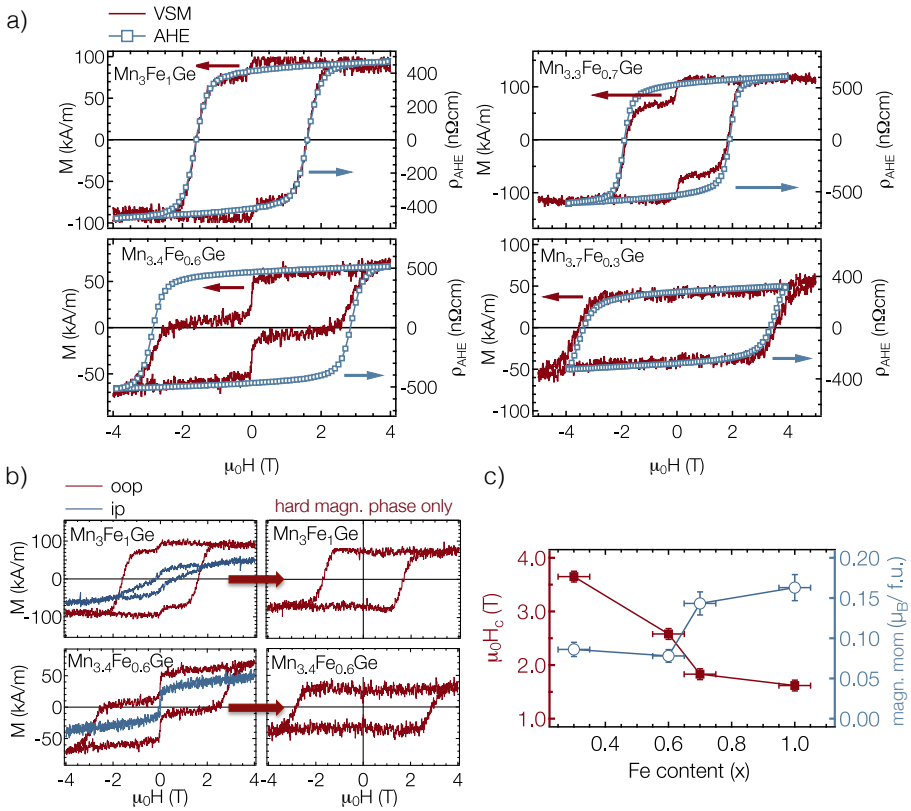

Figure 3.4. a) Comparison of the AHE and VSM measurements measured with out-of-plane applied magnetic field for four different stoichiometries of the $Mn_{4-x}Fe_xGe$ compound. b) VSM measurements performed with field applied in and out-of-plane to the sample surface, exemplarily shown for Mn_3Fe_1Ge and $Mn_{3.4}Fe_{0.6}Ge$. The resulting magnetization, of the hard magnetic phase only, is plotted in the right graphs. The observed soft magnetic contribution, only visible in the VSM measurements and not in the AHE measurements, is attributed to a secondary amorphous phase. c) Coercive field $\mu_0 H_c$ and total magnetic moments of $Mn_{4-x}Fe_xGe$ in dependence on the Fe content x.

Besides the compound with the lowest Fe content, all samples show an additional step in the VSM measurements around 0 T field, which is attributed to the presence of a second magnetic phase. This behavior is well known for the Mn-based compounds and was also observed for example in $Mn_{3-x}Fe_xGa$.[77, 78] Since the AHE measurements do not show such a feature, the second phase might be located at grain boundaries and has a high resistance, therefore not contributing to the AHE. Since XRD measurements did not reveal the presence of a second crystallographic phase, it was concluded that the second magnetic phase might be amorphous or nano-crystalline and therefore cannot be observed using the XRD.

However, the sample with the lowest Fe content does not show this behavior, despite the high roughness. The coercive field of $Mn_{4-x}Fe_xGe$ increases strongly with decreasing Fe content (see Fig. 3.4(c)) starting from 1.61 T for Mn_3Fe_1Ge and increasing to 3.64 T for $Mn_{3.7}Fe_{0.3}Ge$. Figure 3.4(b) exemplarily shows VSM measurements performed with field applied in and out-of-plane to the sample surface, for two different stoichiometries. The in-plane hysteresis curves show only the soft magnetic contribution, which was subtracted from the out-of-plane measurements, in order to extract the magnetization of the hard magnetic phase only. The resulting hysteresis curves are shown in Fig. 3.4(b). The squareness ratio S_R, i.e., the ratio of the remanent magnetization and the saturation magnetization, was determined from the VSM measurements after the subtraction of the soft magnetic contribution. The highest value of 0.94 was determined for $Mn_{3.3}Fe_{0.7}Ge$, which might be the result of slightly lower roughness of this sample. The determined S_R values are given in Tab. 3.1. The magnetization values M_{tot} of the ferrimagnetic compound are below 0.16 μ_B/f.u. for each stoichiometry and decrease with decreasing Fe content. The highest value of $(0.16 \pm 0.02)\ \mu_B$/f.u. was determined for Mn_3Fe_1Ge. $Mn_{3.4}Fe_{0.6}Ge$ and $Mn_{3.7}Fe_{0.3}Ge$ showed the lowest values of $(0.08 \pm 0.01)\ \mu_B$/f.u. and $(0.09 \pm 0.01)\ \mu_B$/f.u. The low magnetization values are close to the theoretically predicted value (0.06) μ_B/f.u for tetragonally distorted Mn_2Fe_1Ge.[70]

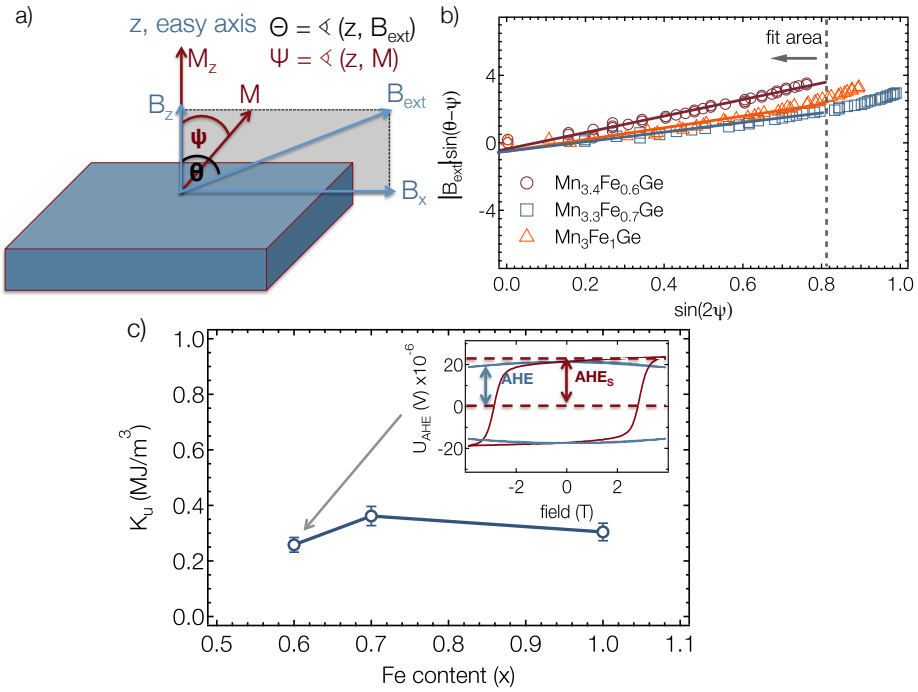

Figure 3.5. a) Measurement configuration for the determination of K_u. B_{ext}, B_x and B_z give the applied external magnetic fields and its in-plane and out-of-plane contribution respectively. M is the direction of the resulting tilted magnetization out of the easy axis direction M_z. b) $|B_{ext}|\sin(\theta-\psi)$ against $\sin(2\psi)$ and the corresponding linear fits. The slope of the linear fit gives the $\frac{K_u}{M_s}$ relation. c) Determined K_u values in dependence on the stoichiometry of Mn-Fe-Ge. The inset exemplarily shows the normalized in-plane (blue) and out-of-plane (red) AHE measurements. The signal-height at zero field is the saturation value AHE_s. The signal changes (marked as AHE) with increasing in-plane field, resulting from the tilt of the magnetization away from the easy axis of the magnetization.

Determination of the perpendicular magnetic anisotropy

The uniaxial perpendicular anisotropy energy K_u is usually obtained using the relation

$$K_u = \frac{\mu_0 H_K M_S}{2} \tag{3.1}$$

with the anisotropy field H_K and the saturation magnetization M_S. However, since it was not possible to saturate the Mn-Fe-Ge compound in the direction

of the magnetic hard axis (in-plane) with the maximum magnetic fields in our setups (7 T), another approach was applied in order to calculate the perpendicular anisotropy energy K_u (see Sec. 2.2.4). The slope of a linear fit of $|B_{ext}|\sin(\theta-\psi)$ plotted against $\sin(2\psi)$ (see Fig. 3.5(b)) gives the relation of $\frac{K_u}{M_s}$. Knowing the saturation magnetization M_s the anisotropy energy K_u can be determined. The resulting values are given in Fig. 3.5(c) and Tab. 3.1. $Mn_{3.7}Fe_{0.3}Ge$ showed no observable change of the AHE signal with field applied in-plane, which was attributed to high magneto-crystalline anisotropy. Still, for this reason it was not possible to evaluate a K_u value for this stoichiometry. Apart from that, the highest anisotropy value of $(0.36 \pm 0.04)\,MJ/m^3$ was determined for $Mn_{3.3}Fe_{0.7}Ge$. In comparison to the calculated values for other Mn-based ternary compounds, $Mn_{4-x}Fe_xGe$ shows similar magneto-crystalline anisotropy, as Mn_2PdGa or Mn_2RhSn.[70] Still, the determined anisotropy energy is lower than the reported experimental values for Mn_3Ge ($1\,MJ/m^3$).[22, 23] A summary of the magnetic properties determined from the VSM and the AHE measurements is given in Tab. 3.1.

Element specific magnetic properties:
X-ray absorption spectroscopy

The element specific magnetic moments, as well as the magnetic coupling between the elements were examined using XAS and XMCD measurements. In order to subtract the contribution of the soft magnetic phase (as detected in the VSM measurements), the spectra were taken at four different magnetic fields (see Fig. 3.6(a)). Simple calculations lead to a separation of the contribution from the soft magnetic (m) and the hard magnetic phase (M), as shown in Fig. 3.6(b). At the maximum applied field ± 3.75 T the sum contribution (M + m) and (−M−m) were determined. To examine the soft magnetic contribution a field of ± 0.1 T was used, yielding M − m and −M + m, respectively. At each field the signals were averaged over four scans, with circular polarization degrees of +90% and −90%. Only the contribution from the hard magnetic phase was used for further calculations and analysis. The resulting XAS and XMCD spectra are shown in Fig. 3.7(a). The measurements revealed ferromagnetic coupling of the total Mn and Fe magnetic moments. The pronounced structure of the Mn-XMCD signal is the superposition of the signals induced by the Mn atoms located at the 2b and 4d Wyckoff position.

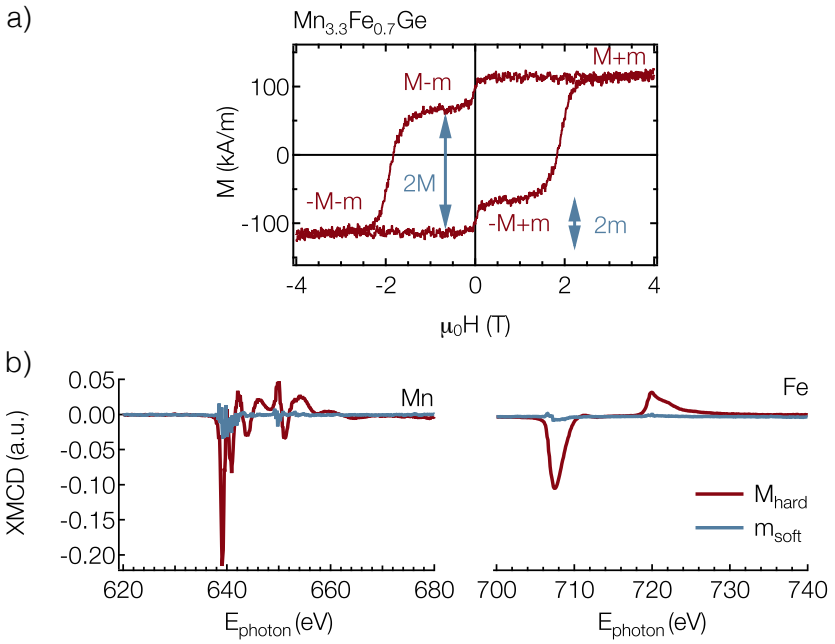

Figure 3.6. a) VSM magnetization measurement of the $Mn_{3.3}Fe_{0.7}Ge$ showing the contributions of the hard magnetic (M) and the soft magnetic phase (m) to the total magnetization of the compound. b) Corresponding XMCD spectra of the soft magnetic (light blue) and hard magnetic (red) phase. It is clearly visible, that the soft magnetic phase provides a small contribution to the Mn and Fe magnetic moments and therefore needs to be taken into account.

This structure confirms the antiferromagnetic ordering of the Mn atoms in this compound. The signal resulting from the soft magnetic phase shows the usual XMCD of a ferromagnet (Fig. 3.6 (b)) (blue curve). To determine the magnetic moment values sum rule analysis was carried out.[50] Normalized XAS spectra for the three investigated stoichiometries are shown in Fig. 3.7(a). Figure 3.7(b) shows the calculated magnetic moments, resulting from the hard magnetic and the soft magnetic phase. The Fe magnetic moments (per atom) M_{Fe}, calculated for the hard magnetic phase, are higher than the Mn magnetic moments M_{Mn}, as expected due to the antiferromagnetic ordering of the Mn sub-lattices and their mutual compensation. The magnetic moments for both elements (Mn and Fe), decrease with decreasing Fe amount x (see

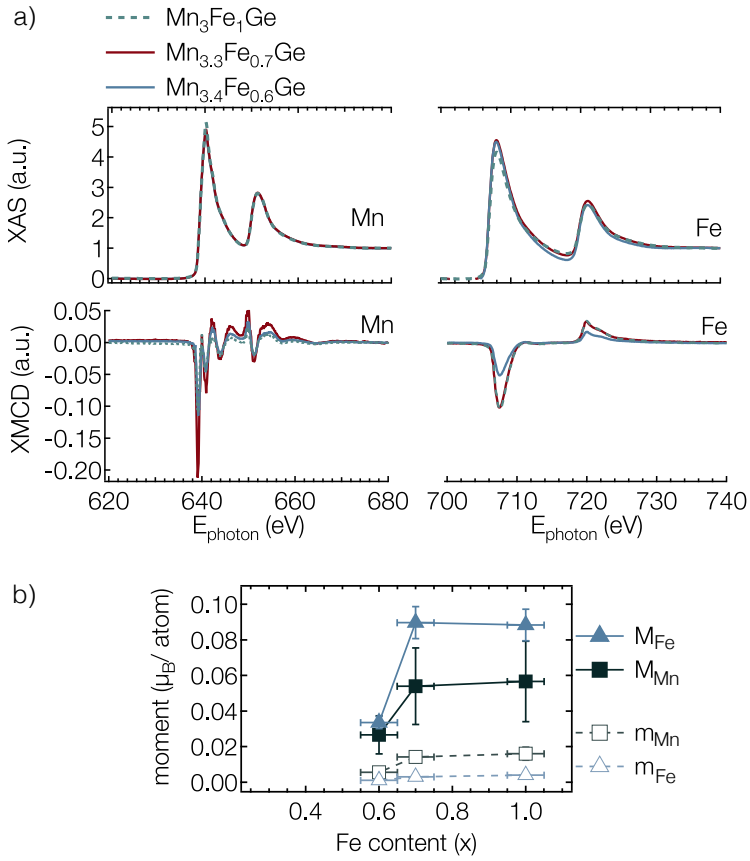

Figure 3.7. a) XAS and XMCD spectra of Mn and Fe measured in TEY. The spectra show no signs of oxidation of the Mn and Fe elements. The pronounced structure of the Mn-XMCD signal reveals the presence two Mn sub-lattices, which have slightly different absorption edges and couple anti-parallel to each other. The same sign of the Mn and Fe-XMCD signals shows the ferromagnetic coupling between Fe and the dominant Mn magnetic sublattice. b) Total magnetic moments of the hard magnetic (M_{Fe} and M_{Mn}) and the soft magnetic phase (m_{Fe} and m_{Mn}), determined using the sum rule analysis.

Table 3.2. Element specific magnetic moments (in μ_B/atom) of the hard magnetic phase M and the soft magnetic phase m, extracted from XAS and XMCD measurements.

sample	M_{Mn}	M_{Fe}	m_{Mn}	m_{Fe}
Mn_3Fe_1Ge	0.057 ± 0.020	0.088 ± 0.009	0.016 ± 0.003	0.004 ± 0.001
$Mn_{3.3}Fe_{0.7}Ge$	0.054 ± 0.020	0.090 ± 0.009	0.014 ± 0.003	0.003 ± 0.001
$Mn_{3.4}Fe_{0.6}Ge$	0.027 ± 0.010	0.033 ± 0.003	0.006 ± 0.001	0.001 ± 0.001

Fig. 3.7(b) and Tab. 3.2). This reveals a higher degree of compensation of the Mn and Fe magnetic moments for $Mn_{4-x}Fe_xGe$ with lower Fe contents.

However, there is a deviation between the total magnetic moments resulting from VSM and XMCD measurements. A possible reason for this is, that it was not possible to determine the exact magnetic moments from the XMCD measurements, since the exact concentration of the hard or the soft magnetic phase is unknown. Nevertheless, M_{Fe} and M_{Mn} show the same dependence on the composition (see Fig. 3.7(b)), as observed in the VSM measurements (see Fig. 3.4(c)), therefore confirming the correlation between the stoichiometry and the magnetic moments of $Mn_{4-x}Fe_xGe$.

3.2.3 Electrical properties

Beside the observation of switching behavior, AHE measurements were used to determine the Hall constant values R_0, the charge carrier densities n and mobilities μ (see Sec. 2.2.3 and Fig. 2.10(a)), which play an important role for the characterization of the electrical behavior of the material. The presence of linear Hall voltage in the AHE measurements at high fields is attributed to the ordinary Hall effect. The slope $\frac{\Delta U_{AHE}}{\Delta B}$ of the linear fit to the measured Hall voltage U_{AHE} gives the Hall constant by using the following formula:

$$R_0 = \frac{\Delta U_{AHE}}{\Delta B} \cdot \frac{d}{I} \tag{3.2}$$

with B the magnetic field, d the layer thickness and I the applied current.

With the calculated Hall constant and the measured resistivity ρ, the charge carrier density n and mobility μ were determined using the formula:

$$n = -\frac{1}{R_0 \cdot e} \tag{3.3}$$

Table 3.3. Resistivity ρ, Hall constant R_0, charge carrier density n and mobility μ of the $Mn_{4-x}Fe_xGe$ compound in dependence on the stoichiometry deduced from the ordinary Hall effect contribution in the AHE measurements. Thermal conductivity λ was calculated using the Wiedemann-Franz law. All measurements were performed at room temperature.

sample	ρ (μΩcm)	R_0 ($\frac{cm^3}{C} \cdot 10^{-3}$)	n ($\frac{1}{cm^3}$)	μ ($\frac{cm^2}{Vs}$)	λ ($\frac{W}{K \cdot m}$)
Mn_3Fe_1Ge	245	−0.133	$4.7 \cdot 10^{21}$	0.54	29.9±7.8
$Mn_{3.3}Fe_{0.7}Ge$	276	−0.187	$3.3 \cdot 10^{21}$	0.68	26.5±7.3
$Mn_{3.4}Fe_{0.6}Ge$	207	−0.065	$9.7 \cdot 10^{21}$	0.31	35.4±8.5
$Mn_{3.7}Fe_{0.3}Ge$	457	−0.224	$2.8 \cdot 10^{21}$	0.49	16.0±5.7

and

$$\mu = \frac{1}{\rho \cdot e \cdot n} \tag{3.4}$$

where e is the elementary charge.
The thermal conductivity λ of this compound was calculated using the Wiedemann-Franz law: [79]

$$\lambda = L \cdot T \cdot \sigma \tag{3.5}$$

with L the Lorenz factor, T the temperature during measurement and σ the conductivity of the sample. The Lorenz factor is assumed to be $L = L_0 = (\frac{\pi^2}{3})(\frac{k_B}{e})^2 = 2.44 \cdot 10^{-8} \frac{V^2}{K^2}$, according to the free electron model. However, this factor is strongly influenced by the material and temperature. Especially the phonon thermal conductivity and inelastic electron-phonon scattering are two contributions, that can cause deviations from L, ranging from values of $2.1 \cdot 10^{-8} \frac{V^2}{K^2}$ to $3.05 \cdot 10^{-8} \frac{V^2}{K^2}$.[80] Therefore, the deviation of L is estimated at $(\pm 0.5 \cdot 10^{-8}) \frac{V^2}{K^2}$. The errors of the resistivity, the Hall constant, the charge carrier density and mobility are around 1%.

All values were calculated from measurements performed at room temperature and are summarized in Tab. 3.3. The samples show high resistivity, which can be attributed to imperfections of the structure, mosaicity and scattering at grain boundaries. Accordingly, mobility and thermal conductivity is one order of magnitude lower, than the values for common metals, as for example Cu or Au. However, the low value of the charge carriers can be attributed to the half-metallicity of Mn-Fe-Ge.

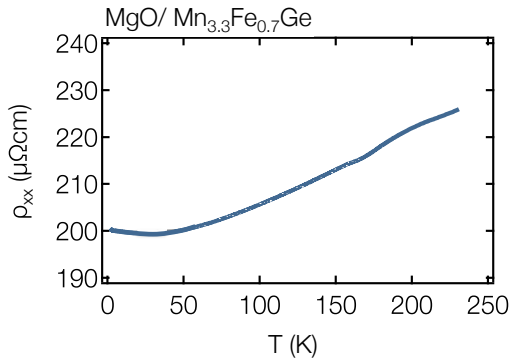

Figure 3.8. Temperature dependent resistivity measurements, exemplarily shown for $Mn_{3.3}Fe_{0.7}Ge$. The sample shows metallic behavior, which was observed for all investigated stoichiometries of Mn-Fe-Ge.

Temperature dependent resistivity measurements confirmed the metallic behavior for Mn-Fe-Ge. Figure 3.8 exemplarily shows the temperature dependent measurement for $Mn_{3.3}Fe_{0.7}Ge$.

3.2.4 Conclusion

In this section the investigated structural, magnetic and electrical properties of sputter deposited Mn-Fe-Ge thin films were presented . It was shown, that the tetragonally distorted phase can be achieved for sputter deposited $Mn_{4-x}Fe_xGe$ in the stoichiometry range of ($0.3 \leq x \leq 1$) and deposition temperatures of 405 °C and 450 °C. The compounds showed low magnetization (≤ 0.16 μ_B/f.u) and high coercive fields (up to 3.64 T). XAS and XMCD measurements revealed ferrimagnetic ordering of the Mn magnetic moments in the Mn-Fe-Ge thin films and ferromagnetic coupling of the Mn and Fe magnetic moments. Anomalous Hall effect measurements showed sharp magnetization switching. The resistivity ranges between 207 μΩcm and 457 μΩcm depending on the stoichiometry. The high resistivity of the Mn-Fe-Ge thin films was explained by imperfections in the crystalline structure. Due to this, the calculated Hall constants R_0 and thus the charge carrier mobility μ, as well as the thermal conductivity λ are one order of magnitude lower compared to the values of common metals. The low charge carrier density value n can be explained by the half-metallicity of this material. The measured anisotropy energy K_u is around 0.3 MJ/m^3. The highest value of (0.36±0.04) MJ/m^3 was determined for $Mn_{3.3}Fe_{0.7}Ge$. The anisotropy of $Mn_{3.7}Fe_{0.3}Ge$ must be even higher, since no tilt of the magnetization out of the easy axis was observable, even at an in-plane field of 4 T.

In summary, the structural, magnetic and electrical properties of $Mn_{4-x}Fe_xGe$ are sensitive to the stoichiometry, providing a possibility to adjust the properties to the individual needs. The strongest challenge is the high roughness of $Mn_{4-x}Fe_xGe$, which is probably a result of the high misfit between the compound and the MgO substrate, leading to strain and dislocations in the thin films. Still, Mn-Fe-Ge is a promising material to serve as a bottom electrode in perpendicular magnetic tunnel junctions (pMTJs), providing high stability agains external magnetic fields, due to its large coercive fields and low magnetic moments.

3.3 The ternary Mn-Fe-Ga compound

In this section the preparation and investigation of crystallographic, structural and magnetic properties of the ternary Mn-Fe-Ga compound thin films will be presented. The influence of different compositions (stoichiometric and off-stoichiometric Mn-Fe-Ga), substrates and deposition temperatures on the material properties was analyzed. The main focus is on stoichiometric $Mn_{3-x}Fe_xGa$ with ($0.3 \leq x \leq 1$), where the tetragonally distorted structure appears to be most stable. In order to improve the surface properties, an alternative deposition process was carried out. Its impact on the structural and magnetic properties will be shown in a separate section. Mn-Fe-Ga combines the required properties to serve as an electrode in spintronic devices, as e.g. MTJs. This section partially includes results from Niesen et al.[77]

Preparation

Mn-Fe-Ga thin films were prepared in the BESTEC sputtering system using DC magnetron co-sputtering from a pure Mn, Fe and a $Mn_{45}Ga_{55}$ composite target. The amount of Mn, in the Mn_yFe_xGa compound, was varied in the range of $1.5 \leq y \leq 3$ and the amount of Fe in the range of $0.3 \leq x \leq 1$. Deposition temperatures from 190 °C to 595 °C were chosen in order to achieve crystalline growth and the tetragonally distorted phase of Mn-Fe-Ga. MgO(100) ($a_{MgO} = 4.21$ Å) and $SrTiO_3$(100) (STO) ($a_{STO} = 3.91$ Å) single crystalline substrates were utilized. Additionally TiN buffered Mn-Fe-Ga thin films on MgO and STO substrates were prepared. The TiN layers (30 nm) were deposited using reactive sputtering in a mixed Ar and N_2 atmosphere which results in stoichiometric TiN thin films. During the sputtering process a N_2 flow of 2 sccm and an Ar flow of 20 sccm was used, leading to a deposition pressure of 1.6×10^{-3} mbar. The stoichiometry of TiN was verified via density, resistivity, and x-ray absorption spectroscopy measurements. Further information on the TiN seed-layer is given in [73]. On top of the Heusler compound a 2 nm thin MgO or Si (as indicated) layer was deposited to prevent the surface from contaminations.

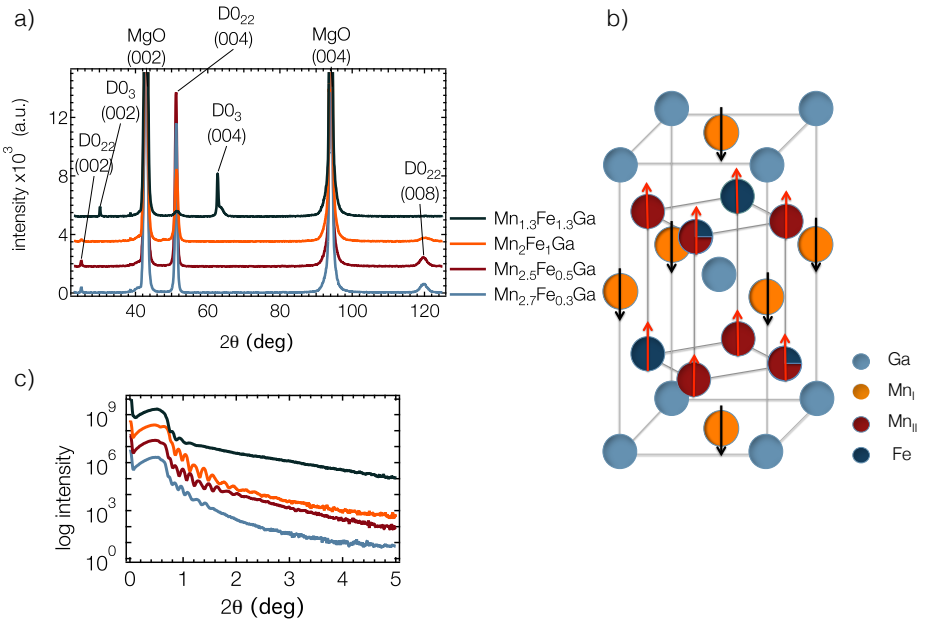

Figure 3.9. a) XRD patterns of the stoichiometric $Mn_{3-x}Fe_xGa$ and the off-stoichiometric $Mn_{1.3}Fe_{1.3}Ga$. The $D0_{22}$ ordering was achieved for the stoichiometric compounds. b) Tetragonally distorted crystal structure ($D0_{22}$) of the ferrimagnetic $Mn_{3-x}Fe_xGa$ compound. Wyckoff position 2a is occupied by Ga, Mn_I occupies positions 2b, and Mn_{II} is sharing the 4d position with Fe. c) XRR patterns of the stoichiometric $Mn_{3-x}Fe_xGa$ and the off-stoichiometric $Mn_{1.3}Fe_{1.3}Ga$.

3.3.1 Structural properties

XRD measurements revealed a strong dependence of the crystalline structure on the Fe amount in the Mn-Fe-Ga. Figure 3.9(b) shows the structure for the tetragonally distorted phase ($D0_{22}$) and exemplary the XRD (a) and XRR (c) patterns of the stoichiometric $Mn_{3-x}Fe_xGa$ and the off-stoichiometric $Mn_{1.3}Fe_{1.3}Ga$. The crystallinity and structure of this compound strongly depends on its composition, as described below. A summary of all investigated stoichiometries is given in Fig. 3.10. The dependence of the lattice constant c on the Mn content in the compound for thin films deposited on MgO substrates is shown in Fig. 3.10(a). The $D0_{22}$ structure was only achieved for

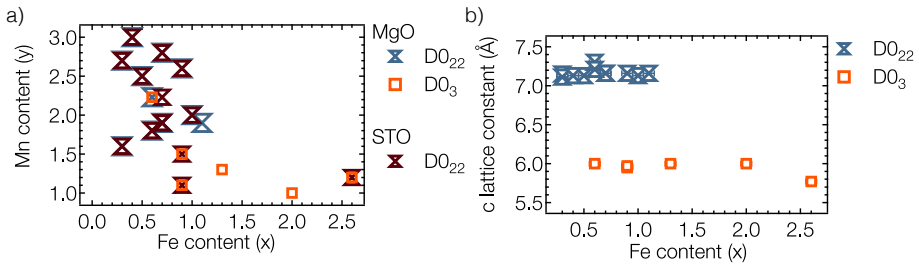

Figure 3.10. a) Overview of all investigated compositions and the determined crystal structures for thin films deposited on MgO and STO substrate for the deposition temperature of 450 °C. b) The dependence of the lattice constant c on the Fe content in the compound for thin films deposited on MgO substrates.

stoichiometric $Mn_{3-x}Fe_xGa$. Especially on MgO substrates, off-stoichiometric Mn_yFe_xGa leads to a mixture of the cubic $D0_3$ and the tetragonally distorted $D0_{22}$ phase. The formation of the $D0_{22}$ crystal structure of $Mn_{3-x}Fe_xGa$ was achieved for the composition range $0.3 \leq x \leq 1$ on MgO and STO substrates (Fig. 3.10(a)) (in agreement with the previously reported data [63]), as well as the TiN seed-layer. The dependence of the out-of-plane lattice constant and the crystal structure upon the Fe and Mn amount in Mn-Fe-Ga for films deposited at 450 °C on MgO and STO substrates, is given in Fig. 3.10(b). With decreasing Fe content, the tetragonally distorted structure ($D0_{22}$) is formed. The measured in-plane and out-of-plane lattice constants (in analogy to Sec. 3.2) are $a = (3.90 \pm 0.01)$ Å and $c = (7.15 \pm 0.04)$ Å for Mn-Fe-Ga for both substrate types, leading to a c/a ratio of 1.8. Increasing the Fe content x in the composition, leads to a formation of the cubic phase ($D0_3$) ($c = 6.00$ Å) on MgO substrates (Fig. 3.10(a) and (b)). On STO the $D0_{22}$ crystallographic phase is formed for every tested composition of Mn-Fe-Ga (see Fig. 3.10(a)). This can be attributed to the low lattice mismatch of the in-plane lattice constant of STO ($a_{STO} = 3.91$ Å) to the in-plane lattice constant of the tetragonally distorted structure (0.3% − 3%).

The roughness values, extracted from XRR measurements (the graphs for $Mn_{3-x}Fe_xGa$ are exemplarily shown in Fig. 3.9(c)) for thin films deposited on MgO, range between 1.7 nm measured for $Mn_{1.3}Fe_{1.3}Ga$ and 1.5 nm determined for the stoichiometric $Mn_{3-x}Fe_xGa$. On STO substrates the roughness is around 0.8 nm for the stoichiometric $Mn_{3-x}Fe_xGa$ and 4.0 nm for the off-

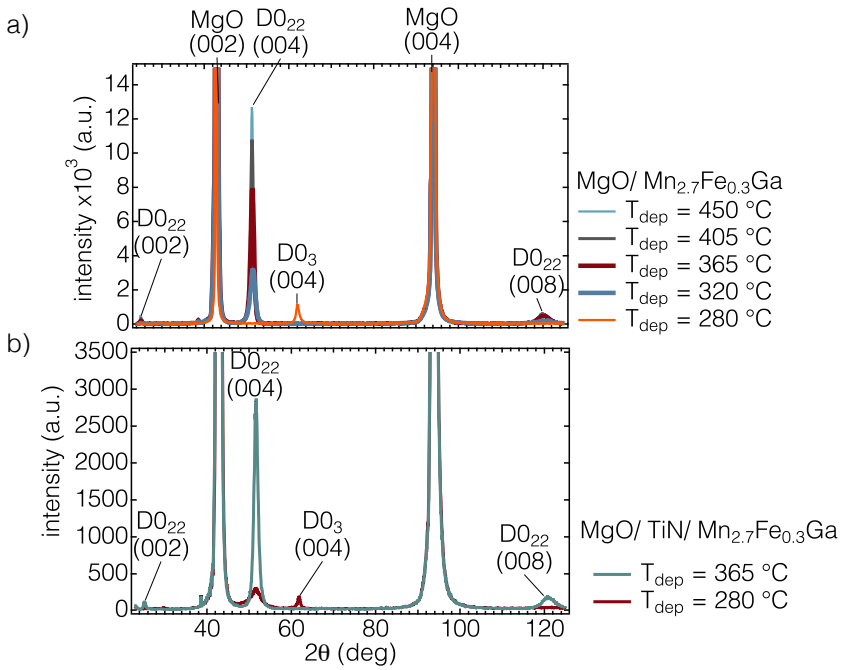

Figure 3.11. a) Dependence of the crystal structure on the deposition temperature investigated for $Mn_{2.7}Fe_{0.3}Ga$. The transition from the cubic $D0_3$ ($a = c = 6.00$ Å) into the tetragonally distorted $D0_{22}$ phase was observed for deposition temperatures above 320 °C. b) Deposition temperature dependence for TiN buffered $Mn_{2.7}Fe_{0.3}Ga$. For clarity, the XRD patterns for only two chosen deposition temperatures are shown.

stoichiometric $Mn_{1.3}Fe_{1.3}Ga$, again due to the presence of cubic structure in this composition and therefore the high lattice mismatch between the substrate and the compound.

The dependence of the crystal structure on the deposition temperature was only investigated for $Mn_{2.7}Fe_{0.3}Ga$, since this composition crystallized in the $D0_{22}$ structure on each tested substrate, as well as on the TiN seed-layer.

The transition from the cubic $D0_3$ ($a = c = 6.00$ Å) to the tetragonally distorted $D0_{22}$ phase, appears for deposition temperatures above 320 °C (Fig. 3.11(a) and Fig. 3.12(a)). For the tested deposition temperatures below 280 °C no crystalline growth was observed (not shown).

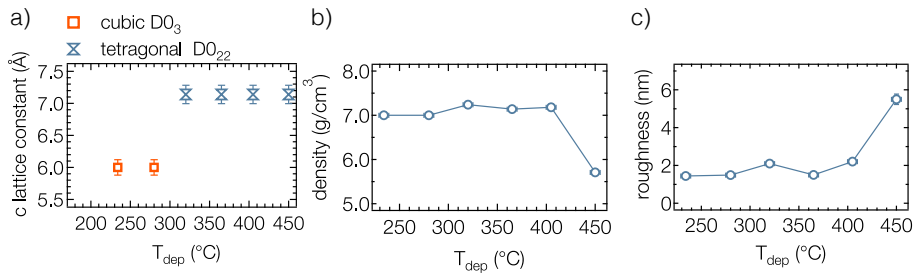

Figure 3.12. a) Dependence of the crystal structure, indicated by the determined out-of-plane lattice constant c, on the deposition temperature. The cubic structure ($D0_3$) is expressed by the squares, the cones give the tetragonally distorted structure ($D0_{22}$), which was found for T_{dep} >320 °C. b) Density dependence on the deposition temperature for $Mn_{2.7}Fe_{0.3}Ga$ deposited on MgO. c) Roughness dependence on the deposition temperature. Above 400 °C a decrease of the density accompanied by an increase in roughness are observed which are explained by Stranski-Krastanov growth, which results in deep grain boundaries.

The density and roughness of $Mn_{2.7}Fe_{0.3}Ga$ also depend on the deposition temperature (see Fig. 3.12). The density is (7.10±0.14) g/cm^3 for all deposition temperatures up to 400 °C (Fig. 3.12(b)). It changes to (5.71±0.11) g/cm^3 for the highest deposition temperature of 450 °C. Taking into account the high roughness value for this deposition temperature (see Fig. 3.12(c)) of 5.50 nm, measured using XRR measurements, the determined density value might be incorrect. As will be shown later (AFM measurements), the high roughness is a result of island growth and deep grain boundaries between the single grains. Since XRR measurements deliver an average value over the whole sample area, the determined density value of the compound might be lowered by the low density, which is present at grain boundaries.

In order to increase the applicability of this compound in future magnetic memory and logic devices, a TiN seed-layer was tested. Figure 3.11(b) shows XRD patterns for two different deposition temperatures of $Mn_{2.7}Fe_{0.3}Ga$ on TiN. It reveals, that the deposition on TiN ($a_{TiN} = 4.24$ Å) leads to a mixture of cubic ($D0_3$) and the tetragonally distorted phase ($D0_{22}$), depending on the Mn-Fe-Ga composition and the deposition temperature. Since the $D0_{22}$ phase for $Mn_{2.7}Fe_{0.3}Ga$, deposited on TiN, already appears at a deposition temperature of 280 °C (Fig. 3.11(b)), TiN obviously influences the crystalline

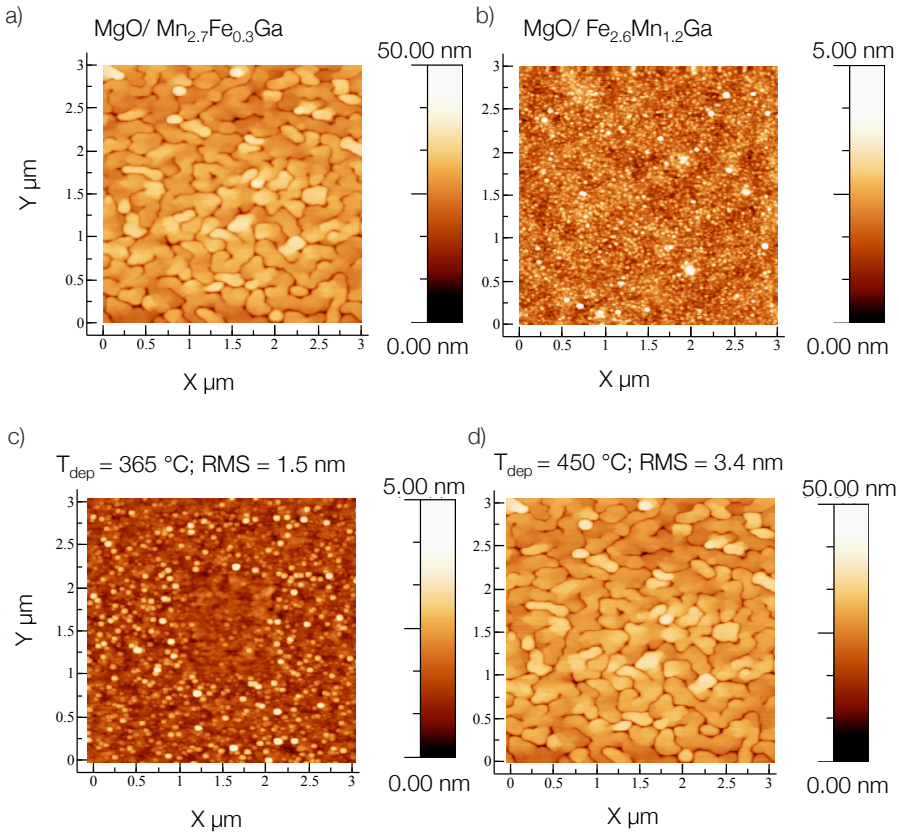

Figure 3.13. Composition and temperature dependence of the surface morphology. a) $Mn_{2.7}Fe_{0.3}Ga$ ($D0_{22}$ structure) and b) $Fe_{2.6}Mn_{1.2}Ga$ ($D0_3$ structure) deposited on MgO substrates. The determined roughness values are a) 3.40 nm and b) 0.80 nm. c) Surface morphology of $Mn_{2.7}Fe_{0.3}Ga$ deposited at 365 °C and d) 450 °C. The determined roughness values are given in the figure.

growth of this compound leading to a lower formation temperature for the tetragonally distorted phase. Similar behavior was observed for the Mn-Ga compound.[73] Since $Mn_{2.5}Fe_{0.5}Ga$ crystallizes in a mixture of the cubic and the tetragonally distorted phase and Mn_2Fe_1Ga forms the cubic phase on TiN, these compositions are not suitable for the use in combination with a TiN buffer layer.

Surface properties

The surface topography of the samples was investigated using AFM. The dependence of the surface morphology on the crystallographic structure for (a) the tetragonally distorted and (b) the cubic $Fe_{2.6}Mn_{1.2}Ga$ thin films is illustrated in Figure 3.13. Both films were deposited on MgO substrates and at 450 °C. The cubic $Fe_{2.6}Mn_{1.2}Ga$ compound forms small grains and a smooth surface. The determined rms roughness for this stoichiometry and deposition temperature is 0.80 nm. The measured rms roughness of the tetragonally distorted $Mn_{2.7}Fe_{0.3}Ga$ is 3.40 nm.[1] The roughness of Mn-Fe-Ga is strongly influenced by the lattice mismatch of the formed structure and the used substrate. The determined rms roughness of all investigated, tetragonally distorted $Mn_{3-x}Fe_xGa$ films deposited on MgO is around (3.00±0.05) nm. In comparison, equivalent films (deposited at the same temperature and with the same stoichiometry) on STO substrates, revealed no island growth and low roughness of (0.43±0.05) nm (not shown), which can be attributed to the low lattice mismatch with the in-plane lattice constant of the tetragonally distorted Mn-Fe-Ga.

Besides the chosen stoichiometry and the resulting crystallographic structure of the compound, the deposition temperature influences the surface properties of Mn-Fe-Ga. Figure 3.13 (c) and (d) shows a comparison of $Mn_{2.7}Fe_{0.3}Ga$ deposited at 365 °C and 450 °C. As can be seen, lowering the deposition temperature leads to reduced roughness (see Tab. 3.4). Small grains are formed, which are not separated by deep grain boundaries and thus build a smooth surface.

In order to investigate the growth mode of Mn-Fe-Ga, especially focusing on the correlation between roughness and thickness of the material, a thickness series of the $Mn_{3.7}Fe_{0.3}Ga$ was examined. Figure 3.14 shows AFM micrographs of $Mn_{3.7}Fe_{0.3}Ga$ deposited at 450 °C for three different thicknesses. As can be seen, the surface morphology transitions with increasing layer thickness. The 10 nm thin film (see Fig. 3.14(a)) shows small grains and a smooth surface. Hence, it can be concluded that for low thicknesses Frank-van der Merwe growth mode is dominating. With increasing film thickness the growth mode

[1] It has to be indicated, that the applied roughness determination using histograms of the line by line analysis from AFM measurements, leads to an underestimation of the roughness values, especially for samples which consist of big grains with steep grain boundaries.

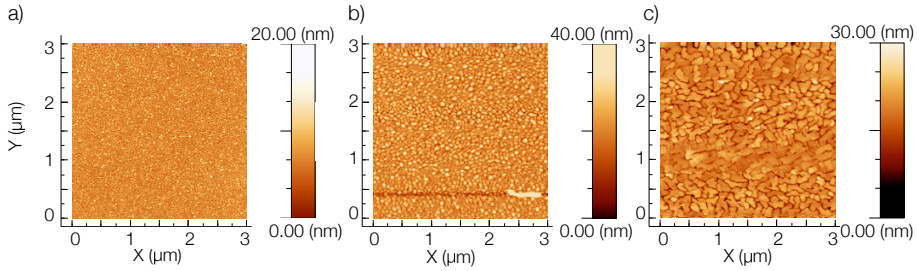

Figure 3.14. Atomic force micrographs of $Mn_{3.7}Fe_{0.3}Ga$ deposited at 450 °C on MgO (001) substrates with thicknesses of a) 10 nm, b) 16 nm and c) 24 nm. The surface morphology is strongly influenced by the layer thickness. At 10 nm film thickness small grains and a smooth surface are observed, leading to the assumption that for low thicknesses Frank-van der Merwe growth mode is dominating. With increasing film thickness the growth mode changes and the material starts to form bigger grains. At 16 nm thickness the first nuclei are formed, initializing the Stranski-Krastanov growth mode, also observed for higher layer thicknesses.

Table 3.4. Summary of the measured roughness values using AFM and XRR for $Mn_{2.7}Fe_{0.3}Ga$ thin films (40 nm), deposited at two different temperatures.

substrate	T_{dep} (°C)	$roughness_{AFM}$ (rms)	$roughness_{XRR}$
MgO	365	1.50±0.05 nm	1.5±0.1 nm
MgO	450	3.40±0.05 nm	5.5±0.1 nm
TiN	450	3.54±0.05 nm	–

changes and the material starts to form bigger grains. The 16 nm thin film (see Fig. 3.14(b)) already shows larger grains. Evidently at this thickness the first nuclei are formed, initializing the Stranski-Krastanov growth mode, usually observed for higher layer thicknesses (see Fig. 3.14(c)).

The structure of Mn-Fe-Ga deposited on a TiN seed-layer also shows a strong dependence on the composition. As previously mentioned, TiN buffered Mn_2Fe_1Ga crystallizes in the cubic $D0_3$ phase. Due to the high lattice mismatch of the cubic phase with the lattice constant of TiN (8.3%), island growth and high roughness (8.6 nm) appears (Fig. 3.15). The TiN buffered $Mn_{2.7}Fe_{0.3}Ga$, crystallized in the $D0_{22}$ phase, shows a similar morphology and roughness value as the unbuffered sample (see Tab. 3.4).

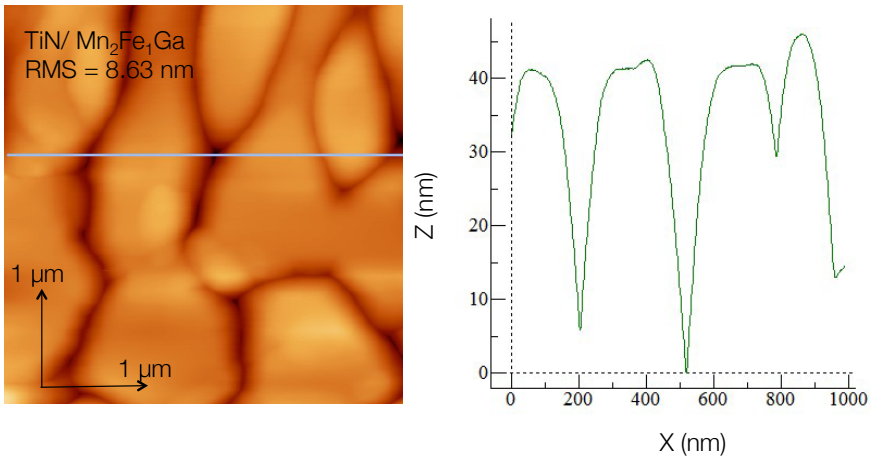

Figure 3.15. Atomic force micrographs of TiN buffered Mn_2Fe_1Ga, crystallized in the cubic $D0_3$ phase, leading to a high lattice misfit between the buffer layer and the material itself. The determined rms roughness is 8.6 nm. A line scan profile is shown on the right side, taken at the position marked by the blue line. The lateral grain sizes, estimated from this profile, are around 200 nm to 300 nm.

Improving the surface properties: The 2-step method

The biggest challenge, in terms of achieving high functionality of the novel material, is that high deposition temperature is needed in order to improve the magnetic properties, as for example the switching behavior (as will be shown later). The surface properties however, and particularly the roughness, strongly increase with increasing deposition temperatures and thus the deposition temperature needs to be as low as possible.

In order to avoid this predicament, different methods were investigated, in order to improve the magnetic and the surface properties at the same time, and hence, to increase the applicability of Mn-Fe-Ga in spintronic devices.

One common approach to achieve smoother surfaces is the deposition of a thin seed layer of the material itself at high temperatures, so that the right structure of the compound is already formed, followed by the deposition of the remaining thin film at lower temperatures. However, this approach did not lead to any improvement of the surface properties of $Mn_{3-x}Fe_xGa$

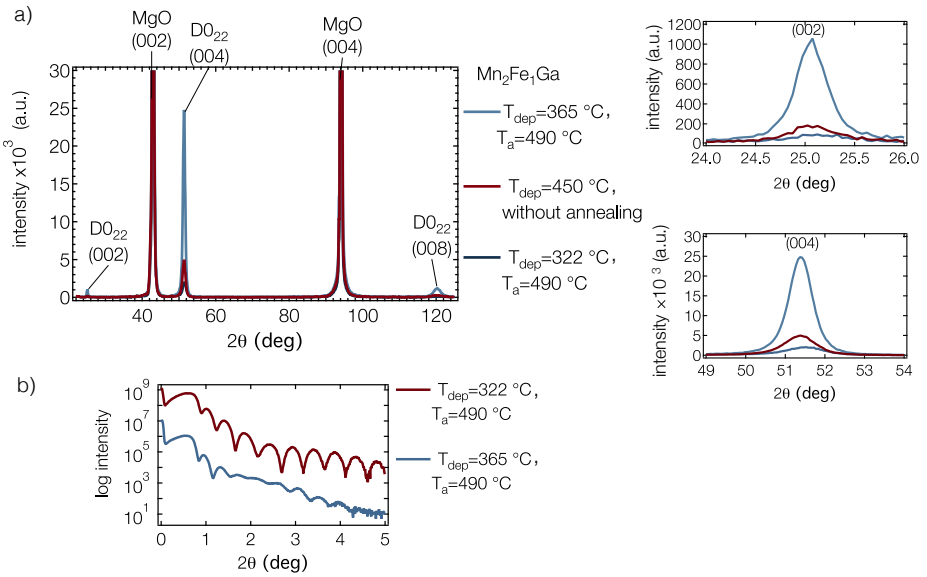

Figure 3.16. a) Comparison of XRD patterns for Mn_2Fe_1Ga with and without the 2-step preparation process and between two different initial deposition temperatures. The right graphs show a cut-out of the complete XRD measurement, around the (002) and the (004) peak of Mn_2Fe_1Ga. The highest peak intensity shows Mn_2Fe_1Ga deposited at 365 °C and in-situ post annealed at 490 °C, revealing that this sample shows the highest crystallinity. b) XRR graphs for Mn_2Fe_1Ga prepared using the 2-step deposition process for two different initial deposition temperatures. The slower decay of the oscillations amplitude measured for Mn_2Fe_1Ga deposited at a lower temperature (322 °C) is indicating the lower roughness of this sample.

(roughness of the resulting thin films was still around (3±1) nm and additional crystallographic phases appeared for all investigated compositions). Hence, various deposition processes were carried out, in order to decrease the surface roughness while maintaining the structural and magnetic properties of the compound. Successful improvement of the surface properties was achieved by the 2-step preparation process, which will be referred to as the **2-step method**.

In the first step the substrate was heated during deposition close to the structural ordering temperature of $Mn_{3-x}Fe_xGa$ into the tetragonally distorted phase. In a second step, the sample was in-situ post annealed at high tem-

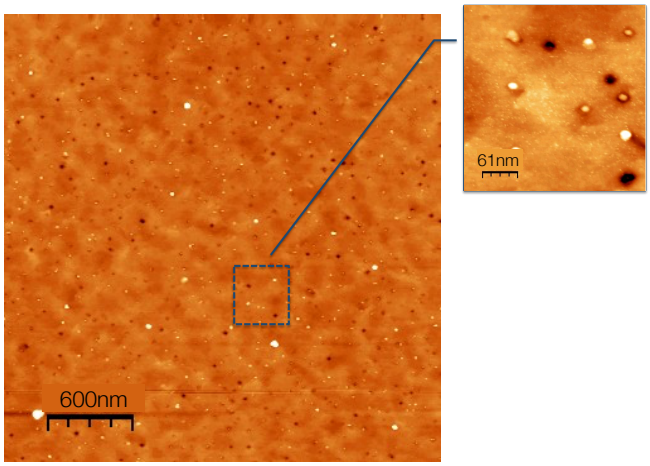

Figure 3.17. Atomic force micrographs of Mn_2Fe_1Ga deposited at 365 °C and in situ post annealed at 490 °C for 1 hour. The determined roughness is 0.6 nm. The right micrograph shows a closer look into the marked area.

peratures for 1 hour. Different initial deposition temperatures in the range of 250 °C $\leq T_{dep} \leq$ 365 °C and different post annealing temperatures were tested, in order to investigate and identify the optimal procedure.

The 2-step method had varying influence on the different stoichiometries of $Mn_{3-x}Fe_xGa$. In most cases and on both tested substrate types, this deposition method led to a phase change into the non magnetic $D0_{19}$ crystallographic phase and to the formation of additional crystallographic phases. Solely for the Mn_2Fe_1Ga an improvement of the surface morphology, without impairing the crystallinity, was achieved. Thus, in the following, only the results for this composition will be presented.

Figure 3.16 shows a comparison of XRD patterns for Mn_2Fe_1Ga with and without the 2-step preparation processes. As can be extracted from the XRD patterns (Fig. 3.16(a)), lowering the initial deposition temperature reduces the crystallinity of the sample (lower intensity of the $(004)_{MFG}$ peak). Increasing the post annealing temperature led to increased roughness and additional crystallographic phases. The roughness of the two shown samples, determined using XRR (see Fig. 3.16(b)), is 0.40 nm for the initial deposition temperature of 322 °C and 0.60 nm for 365 °C. The roughness values were confirmed using

AFM measurements, which showed a smooth surface (for both deposition temperatures) and roughness values of 0.43 nm for the sample deposited at 322 °C and 0.60 nm for the sample deposited at 365 °C. Fig. 3.17 exemplarily shows the surface morphology of the sample deposited at 365 °C and in situ post annealed at 490 °C.

Due to the trade-off between roughness and crystal quality of the material, the sample deposited at a higher initial deposition temperature was chosen, even though the roughness of the sample with lower initial deposition temperature is slightly lower. As it will be shown in the next section, higher crystalline quality is more important for sharp magnetic switching and thus preferable for further investigations and integration of this material into future applications. As a conclusion, the optimum parameters for the 2-step process are: initial deposition at 365 °C and in-situ post annealing at 490 °C.

3.3.2 Magnetic and electrical properties

In the following sections the magnetic and electrical properties of the off-stoichiometric Mn_yFe_xGa and the stoichiometric $Mn_{3-x}Fe_xGa$ are presented. It will be shown, that the magnetic properties are strongly influenced by the composition, the crystallinity and the surface properties of the material. The influence of the 2-step process on the magnetic properties of the material will be pointed out in a separate section, confirming the previously identified optimum deposition parameters in terms of implementation of $Mn_{3-x}Fe_xGa$ into future applications.

Alternating Gradient Magnetometry and X-Ray Magneto Circular Dichroism measurements

Figure 4.6(a) shows the magnetic moments extracted from AGM measurements for the off-stoichiometric Mn_yFe_xGa and the stoichiometric $Mn_{3-x}Fe_xGa$. The influence of Fe doping on the magnetic moments is different for the two composition types.

The stoichiometric $Mn_{3-x}Fe_xGa$ shows increasing total magnetic moments with increasing Fe content x, which is in line with the observations for Mn-Fe-Ge (see Sec. 3.2). A magnetic moment of $(0.51 \pm 0.05)\,\mu_B$/f.u. was determined for $Mn_{2.7}Fe_{0.3}Ga$. Mn_1Fe_2Ga, which crystallizes in a mixture of

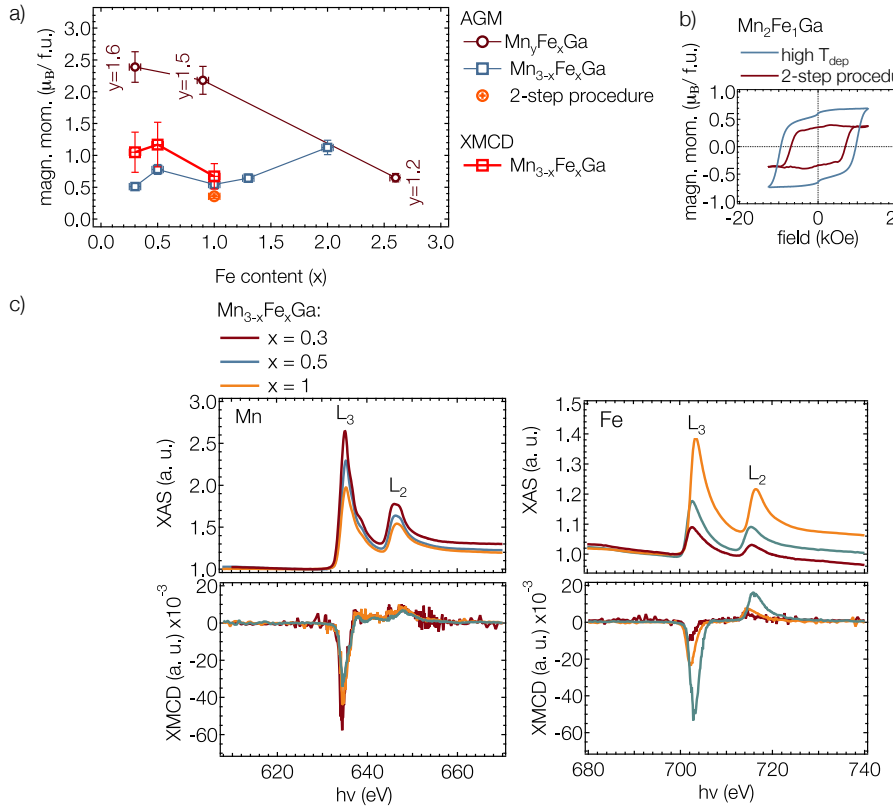

Figure 3.18. a) Total magnetic moments μ_B/f.u. of stoichiometric $Mn_{3-x}Fe_xGa$ and off-stoichiometric Mn_yFe_xGa determined using AGM and XMCD measurements. Additionally the measured magnetic moment for Mn_2Fe_1Ga, deposited using the 2-step procedure, was implemented in the graph for comparison. b) Comparison between the out-of-plane AGM hysteresis curves for Mn_2Fe_1Ga deposited using the usual deposition at $T_{dep} = 450\,°C$ and the 2-step deposition procedure (Mn_2Fe_1Ga, deposited at 365 °C, followed by an in-situ post annealing process at 490 °C). c) XAS and XMCD measurements of Si capped $Mn_{3-x}Fe_xGa$ thin films.

the cubic $D0_3$ and the tetragonally distorted phase $D0_{22}$, showed the highest magnetic moment of $(1.12 \pm 0.1)\ \mu_B$/f.u.

Opposite behavior was observed for the off-stoichiometric Mn_yFe_xGa: the magnetic moments decrease with increasing Fe content. The compound with the lowest Fe content ($Mn_{1.6}Fe_{0.3}Ga$, $D0_{22}$) shows the highest magnetic moment value of $(2.39 \pm 0.2)\ \mu_B$/f.u. and the sample with the highest Fe

amount ($D0_3$ $Mn_{1.2}Fe_{2.6}Ga$) shows a total magnetic moment of (0.65 ± 0.06) μ_B/f.u. The values are summarized in table 3.5.

All samples show a feature in the M(H) curves around 0 Oe field (see inset in Fig. 3.18(a) (blue curve)), which was attributed to the presence of a second phase (soft magnetic) inside the Mn-Fe-Ga thin films (similar to the Mn-Fe-Ge see Sec. 3.2). Identical behavior was reported for Mn_2Fe_1Ga.[78] XRD patterns of these samples did not reveal the reflections of any additional crystallographic phase, thus it can be concluded that the second phase is amorphous or nanocrystalline and might be located at the grain boundaries, as also observed and concluded for Mn-Fe-Ge (see Sec. 3.2).

The feature in the AGM measurements is much less pronounced for the Mn_2Fe_1Ga prepared using the 2-step procedure (see inset in Fig. 3.18(b) (red curve)). This was attributed to the low roughness of the sample prepared using the 2-step method, where no deep grain boundaries were observed using AFM. This confirms that the amorphous, soft magnetic phase must be located at the grain boundaries, observed for Mn_2Fe_1Ga deposited using the conventional sputtering deposition. The determined magnetic moment for Mn_2Fe_1Ga, deposited using the 2-step procedure, is (0.36 ± 0.04) μ_B/f.u. (see Fig. 3.18(a)) which is lower than the value determined for the Mn_2Fe_1Ga, deposited at high temperature.

The element specific magnetic properties were investigated using XAS and XMCD measurements. A detailed description of the data evaluation is given in the Sec. 2.2.3.

Normalized XAS spectra for the three investigated stoichiometries are shown in Fig. 3.18(c). The measurements reveal ferromagnetic coupling of the total Mn and Fe magnetic moments. The structure of the Mn-XMCD signal shows multiple features between the L_3 and L_2 absorption edges, which is a result of the slightly different absorption edges for the two Mn sublattices, confirming the antiferromagnetic ordering of the Mn atoms in this compound. Compared to the Mn-XMCD signal of the $Mn_{4-x}Fe_xGe$ compound (see Sec. 3.2), the $Mn_{3-x}Fe_xGa$ signal is less pronounced. A possible reason is the lower degree of compensation due to the lower amount of Mn atoms in $Mn_{3-x}Fe_xGa$, leading to a higher occupation of the 4d Wyckoff position by Fe atoms.

The determined values of the magnetic moments are given in Tab. 3.5 and Fig. 3.18(a). The total magnetic moments extracted from the XMCD measurements are in agreement (within the error bars) with the values de-

Table 3.5. Summary of the total magnetic moments of Mn-Fe-Ga deposited at high temperatures, extracted from out-of-plane AGM hysteresis loops and XMCD measurements. Mn_2Fe_1Ga, deposited using the 2-step procedure, reveals the lowest magnetic moment. Combined with the low roughness and the improved magnetic switching behavior this sample can be declared as the most promising composition for applications.

$Mn_{3-x}Fe_xGa$	structure	m_{AGM} (μ_B/f.u.)	m_{XMCD} (μ_B/f.u.)
$Mn_{2.7}Fe_{0.3}Ga$	$D0_{22}$	0.51 ± 0.05	1.05 ± 0.32
$Mn_{2.5}Fe_{0.5}Ga$	$D0_{22}$	0.78 ± 0.08	1.17 ± 0.35
Mn_2Fe_1Ga	$D0_{22}$	0.54 ± 0.05	0.67 ± 0.20
Mn_2Fe_1Ga (2-step)	$D0_{22}$	0.36 ± 0.04	0.67 ± 0.20
Mn_1Fe_2Ga	$D0_3$ and $D0_{22}$	1.12 ± 0.10	
Mn_yFe_xGa	structure	m_{AGM} (μ_B/f.u.)	m_{XMCD} (μ_B/f.u.)
$Mn_{1.3}Fe_{1.3}Ga$	$D0_3$ and $D0_{22}$	0.64 ± 0.06	0.77 ± 0.23
$Mn_{1.2}Fe_{2.6}Ga$	$D0_3$	0.65 ± 0.06	
$Mn_{1.5}Fe_{0.9}Ga$	$D0_3$	2.18 ± 0.20	
$Mn_{1.6}Fe_{0.3}Ga$	$D0_{22}$	2.39 ± 0.20	

termined from AGM hysteresis curves. The highest magnetic moment of $(1.17 \pm 0.35)\ \mu_B$/f.u. was calculated for $Mn_{2.5}Fe_{0.5}Ga$. The lowest value of $(0.67 \pm 0.20)\ \mu_B$/f.u.was determined for Mn_2Fe_1Ga.

The determined total magnetic moment of the 2-step sample is in agreement (within the error limits) with the value determined for Mn_2Fe_1Ga deposited at high temperature.

Anomalous Hall Effect measurements

The coercivity, the squareness ratio and the resistivity of the Mn-Fe-Ga thin films were deduced from AHE measurements performed in a 4-terminal arrangement and carried out in a closed-cycle He-cryostat. The Hall resistivity ρ_H was determined using the procedure described in Sec. 2.2.3 and evaluated using the following formula:

$$\rho_H = \frac{E_{xy}}{j_{xx}} = \frac{U_{xy} \cdot d}{I_{xx}} \tag{3.6}$$

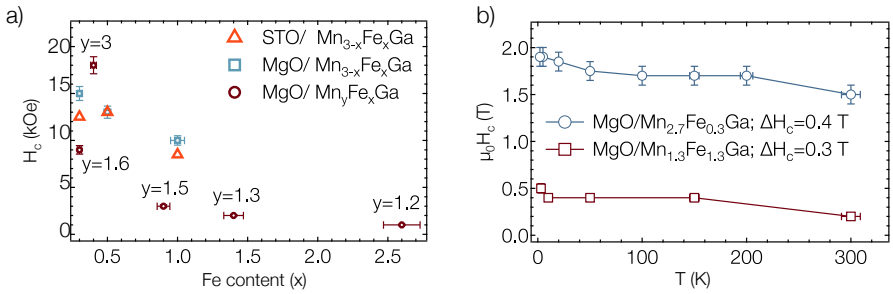

Figure 3.19. a) Coercive field dependence on the Fe content x in Mn-Fe-Ga extracted from AHE measurements. b) Coercive fields of $Mn_{2.7}Fe_{0.3}Ga$ and $Mn_{1.3}Fe_{1.3}Ga$ in dependence on the temperature.

with U_{xy} the measured Hall voltage, d the film thickness and I_{xx} the applied current. A detailed description of the measurement technique is given in Sec. 2.2.3.

Figure 3.19(a) shows coercivity fields, extracted from out-of-plane AHE hysteresis curves for stoichiometric and off-stoichiometric Mn-Fe-Ga deposited on MgO and STO substrates. Coercivity up to 18 kOe can be reached by tuning the composition. With increasing Fe content the coercivity decreases. The highest value (18 kOe) was measured for the off-stoichiometric $Mn_{3.0}Fe_{0.4}Ga$. The lowest value of 2 kOe showed the cubic $Mn_{1.3}Fe_{1.3}Ga$.[2]

The evolution of the coercive field with temperature is shown in Fig. 3.19(b). Both compositions show a significant change of the coercivity with decreasing temperature ($\Delta H_c = 0.4$ T for $Mn_{2.7}Fe_{0.3}Ga$ and $\Delta H_c = 0.3$ T for $Mn_{1.3}Fe_{1.3}Ga$). The strongest increase takes place at temperatures below 50 K.

Figure 3.20(a) shows out-of-plane AHE hysteresis curves (after symmetrization) for stoichiometric $Mn_{3-x}Fe_xGa$ and off-stoichiometric $Mn_{1.3}Fe_{1.3}Ga$ deposited on MgO and STO substrates. Coercive fields, and the overall shape of the magnetic hysteresis $\mu_0 H_c$ (see Fig. 3.20(b)) for $Mn_{3-x}Fe_xGa$, deposited

[2] It should be noted, that the coercive fields were calculated from AHE measurements after subtracting a present symmetrical contribution from the measurements (symmetrization), attributed to the presence of a magnetoresistive effect (MR). The MR effect is strongly connected to the resistivity of the samples.[81] The difference in the MR effect contribution for the different samples, is a result of different grain structures and defects. Both strongly influence the conduction mechanisms inside the thin films, which in turn influence the MR effect.

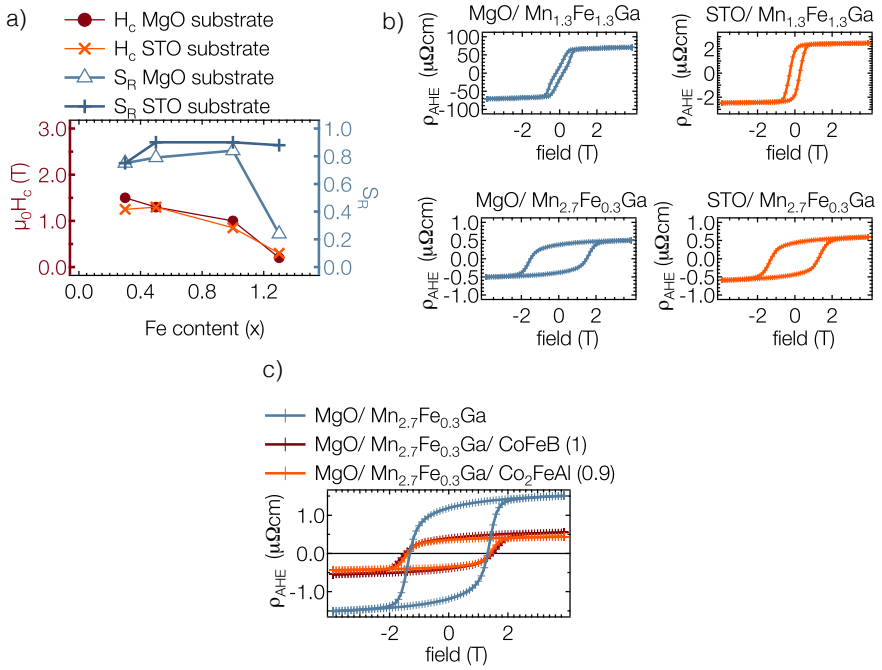

Figure 3.20. a) Coercivity $\mu_0 H_c$ and squareness ratios S_R in dependence on the Fe content x in $Mn_{3-x}Fe_xGa$. b) Out-of-plane AHE hysteresis curves for stoichiometric $Mn_{2.7}Fe_{0.3}Ga$ and off-stoichiometric $Mn_{1.3}Fe_{1.3}Ga$ deposited on MgO and STO substrates, after symmetrization. Coercive fields, and the overall shape of the magnetic hysteresis are in agreement. The small variations of the coercivity values can be explained by differences in the roughness of $Mn_{3-x}Fe_xGa$ deposited on the two different substrate types. c) Influence of a thin Co_2FeAl or Co-Fe-B interlayer on the magnetic and electrical properties. The added interlayer reduces the effective height of the AHE. The coercivity of the whole stack is increased, compared to the coercivity of a single $Mn_{2.7}Fe_{0.3}Ga$ layer by 0.1 T for Co_2FeAl and by 0.2 T for CoFeB. No additional switching was observed, which could be attributed to separate switching of the soft magnetic electrode.

on MgO and STO are in agreement. The small variations of the coercivity values can be explained by differences in the roughness of $Mn_{3-x}Fe_xGa$ deposited on the two different substrate types. The squareness ratio S_R, e.g. the remanence value divided by the saturation value, is also in a good agreement for both substrate types. The values range between 0.8 and 0.9 and increase

with increasing Fe amount for the stoichiometric and tetragonally distorted $Mn_{3-x}Fe_xGa$. The off-stoichiometric $Mn_{1.3}Fe_{1.3}Ga$ deposited on MgO substrate shows the lowest S_R of 0.25. On STO, the sample with the same stoichiometry shows higher S_R and therefore an improved switching behavior.

The commonly used tunneling barrier material in devices, as for example MTJs are metal-oxides, as MgO or AlO_x. Since Mn has a strong affinity to oxygen, the implementation of Mn-based compounds as an electrode into MTJs is quite challenging. Hence, the influence on the magnetic properties of $Mn_{3-x}Fe_xGa$ by a thin soft magnetic interlayer (Co_2FeAl and CoFeB), which could be integrated into the layer stack in order to prevent oxidation of the Mn-based compound, was investigated. Figure 3.20(c) shows a comparison between the AHE hysteresis curves of $Mn_{2.7}Fe_{0.3}Ga$ with a 1 nm thin CoFeB and a 0.9 nm thin Co_2FeAl layer on top. The Co-based compounds with the chosen thicknesses were investigated in prior and provide perpendicular magneto crystalline anisotropy. The added interlayer reduces the effective height of the AHE. The coercivity of the whole stack is slightly higher than the coercivity of a single $Mn_{2.7}Fe_{0.3}Ga$ layer by 0.1 T for Co_2FeAl and by 0.2 T for CoFeB. No additional switching or step in the measurements was observed, which could be attributed to separate switching of the soft magnetic electrode. Hence, the soft magnetic materials can be pinned by using them in combination with the hard magnetic Mn-Fe-Ga compound.

The influence of the deposition temperature T_{dep} on the magnetic properties of stoichiometric Mn-Fe-Ga was tested using $Mn_{2.7}Fe_{0.3}Ga$, which appeared to be the most stable regarding the crystallization in the tetragonally distorted phase, according to previous investigations. Figure 3.21(a) shows the measured AHE hysteresis curves for all investigated deposition temperatures. The extracted values of S_R (red curve) and $\mu_0 H_c$ (blue curve) are shown in Fig. 3.21(b). Both parameters are strongly correlated with the structure, which is formed at a certain T_{dep}. At low deposition temperatures, where the cubic $D0_3$ phase is formed, the squareness ratios and the coercivity values range between 0 and 0.4. Below the phase transition temperature $T_{dep} = 320\,°C$ both parameters strongly decrease. For temperatures $T_{dep} > 350°C$, the squareness ratio and the coercivity increase due to the formation of the tetragonal phase. The squareness ratio increases with increasing deposition temperature to the maximum value for $T_{dep} = 450\,°C$. The coercivity shows

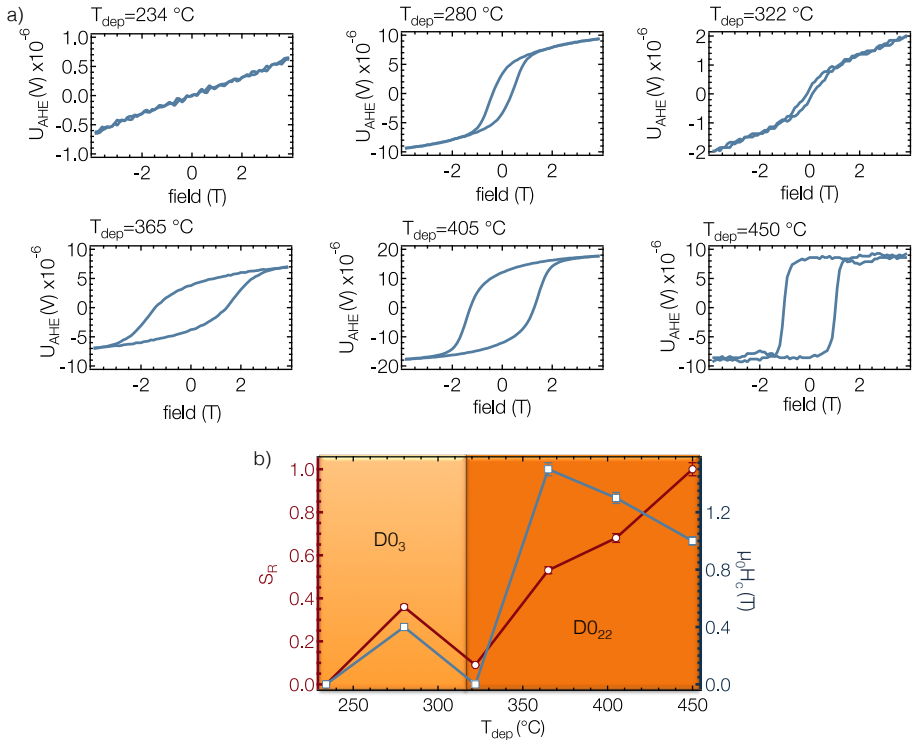

Figure 3.21. a) Out-of-plane AHE hysteresis curves for $Mn_{2.7}Fe_{0.3}Ga$ deposited at different substrate temperatures. b) S_R (red curve) and $\mu_0 H_c$ (blue curve) in dependence on the deposition temperature. Both parameters are correlated with the structure, which is formed at a certain T_{dep}. For low deposition temperatures, $D0_3$ phase, the squareness ratios and the coercivity values are low. For temperatures above 350 °C S_R and $\mu_0 H_c$ increase, due to the structural transition into the $D0_{22}$ phase.

the maximum value of 1.6 T at the formation temperature of the $D0_{22}$ phase T_{dep} =350 °C and decreases with further increase of T_{dep}.

The measured resistivity of the Mn-Fe-Ga deposited on MgO and STO substrates is shown in Fig. 3.22(a). All samples show high resistivity, which is dependent on the stoichiometry and the crystal structure. Tetragonally distorted compounds show resistivities in the range of 300 μΩcm to 450 μΩcm at room temperature. Mn-Fe-Ga with the higher Fe content shows higher resistivity, for example the cubic and off-stoichiometric $Mn_{1.2}Fe_{2.6}Ga$ com-

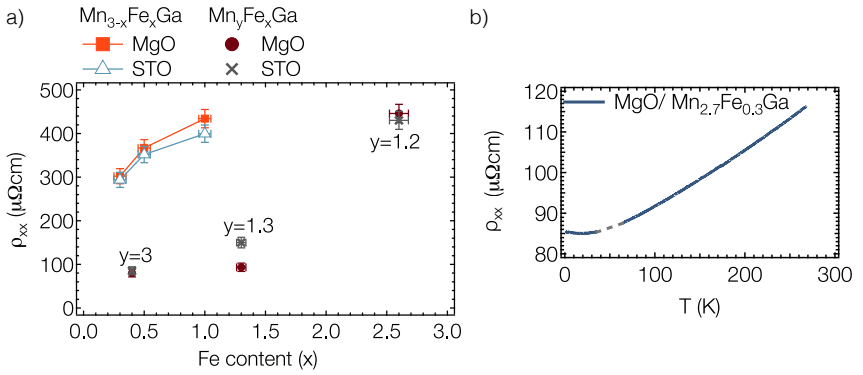

Figure 3.22. a) Resistivity ρ_{xx} of stoichiometric $Mn_{3-x}Fe_xGa$ and off-stoichiometric Mn_yFe_xGa deposited on MgO and STO substrates. All samples show high resistivity, which is dependent on the stoichiometry and the formed structure. Especially the $D0_{22}$ structured samples show high resistivities. Higher Fe content leads to higher resistivity, as observed for the cubic and off-stoichiometric $Mn_{1.2}Fe_{2.6}Ga$ (450 μΩcm). $Mn_{3.0}Fe_{0.4}Ga$ and $Mn_{1.3}Fe_{1.3}Ga$ ($D0_3$ structure), show lower resistivity values. The measured resistivities for samples deposited MgO or STO substrates are in good agreement. b) Temperature dependence of the resistivity measured on $Mn_{2.7}Fe_{0.3}Ga$.

pound shows resistivity of 450 μΩcm. The off-stoichiometric $Mn_{3.0}Fe_{0.4}Ga$ and $Mn_{1.3}Fe_{1.3}Ga$, also crystallized in the cubic structure, provide much lower resistivities, of around 100 μΩcm to 200 μΩcm. There is no significant difference of the resistivities for thin films deposited on MgO or STO substrates. The high resistivity might be a consequence of the high roughness. However, the increasing behavior with increasing Fe content is not correlated with higher roughness, and therefore might be caused by changes in the electronic structure, due to different number of valence electrons of Mn and Fe atoms.

Temperature dependent resistivity measurements revealed metallic behavior of this compound (see Fig. 3.22(b)). For all measured samples the resistivity decreases with decreasing temperature and approaches a minimum for temperatures below 25 K.

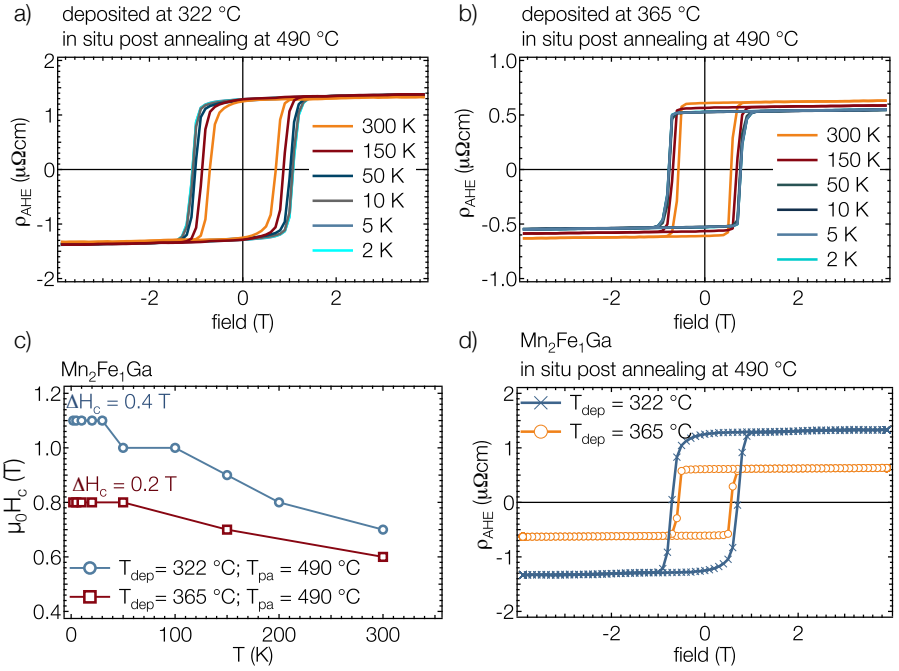

Figure 3.23. a) AHE hysteresis curves, measured at temperatures down to 2 K, for Mn_2Fe_1Ga, deposited at $T_{dep} = 322\,°C$. b) AHE hysteresis curves of Mn_2Fe_1Ga, deposited at $T_{dep} = 365\,°C$. c) Coercivity dependence on the measurement temperature for Mn_2Fe_1Ga, deposited at $T_{dep} = 322\,°C$ and $T_{dep} = 365\,°C$, both in situ post annealed for 1 hour at 490 °C. The effective height of the AHE is stable for the whole temperature range and the switching behavior is improved for samples deposited at the higher initial deposition temperature. The measurement temperature has a stronger impact on the coercivity of the sample deposited at 322 °C. d) Direct comparison of AHE measurements for Mn_2Fe_1Ga deposited at two different deposition temperatures, measured at 300 K. The switching behavior and the coercivity for the two deposition temperatures is different. The sample deposited at higher T_{dep} shows higher squareness ratio and lower coercivity ($\mu_0 H_C = 0.6\,T$), compared to the sample deposited at lower T_{dep}. The different switching and magnetic properties are attributed to the structural changes in the samples, initiated by the different deposition temperatures.

Influence of the 2-step deposition procedure on the magnetic and electrical properties

The following section, focuses on the influence of the 2-step-process **only for** Mn_2Fe_1Ga deposited at $T_{dep} = 322\,°C$ and $T_{dep} = 365\,°C$ and in-situ post annealed at 490 °C, which were identified as the optimum parameters in Sec. 3.3.1.

The 2-step procedure (T_{dep} =365 °C) optimized not only the crystallographic and surface properties, but also the switching behavior of Mn_2Fe_1Ga. The squareness ratio is 1 (compared to $S_R = 0.8$ for Mn_2Fe_1Ga deposited at 450 °C) and the coercivity at room temperature is slightly lowered to 0.6 T (compared to 1 T).

Figures 3.23(a) and (b) show the AHE hysteresis curves, measured at different temperatures down to 2 K for Mn_2Fe_1Ga prepared by the 2-step method for the different T_{dep}. The effective height is stable for the whole temperature range, the switching behavior is improved and the increase of coercivity with decreasing temperature is lowered to 0.2 T for the sample deposited at the higher initial deposition temperature. A direct comparison of AHE hysteresis curves, measured at 300 K, reveals a change of the switching behavior and the coercivity for the two deposition temperatures. The sample deposited at 365 °C shows higher squareness ratio ($S_R = 1$) and lower coercivity ($\mu_0 H_C = 0.6\,T$), compared to the sample deposited at 322 °C ($S_R = 0.96$ and $\mu_0 H_C = 0.74\,T$) (see Fig. 3.23(d)). Additionally, the measurement temperature has a stronger impact on the coercivity of the sample deposited at 322 °C (see Fig. 3.23(c)). These differences can be attributed to structural changes in the samples, initiated by the different deposition temperatures. Higher T_{dep} increase the crystallinity, which leads to an improvement of the switching behavior, but decreases the effective height of the AHE. Figures 3.24(a) and (b) show temperature dependence of the longitudinal resistivity ρ_{xx} for the previously described samples. At room temperature (300 K) Mn_2Fe_1Ga deposited at $T_{dep} = 365\,°C$ shows lower resistivity ($\rho_{xx} = 127\,\mu\Omega cm$), compared to the sample deposited at 322 °C ($\rho_{xx} = 410\,\mu\Omega cm$). At low temperatures the resistivity shows different behavior for the two deposition procedures. The sample deposited at the higher temperature reaches the lowest value of $\rho_{xx} = 113\,\mu\Omega cm$ at 55 K and stays stable for temperatures down to 2 K (see Fig. 3.24(a)). The sample deposited at 322 °C shows a minimum resistivity of

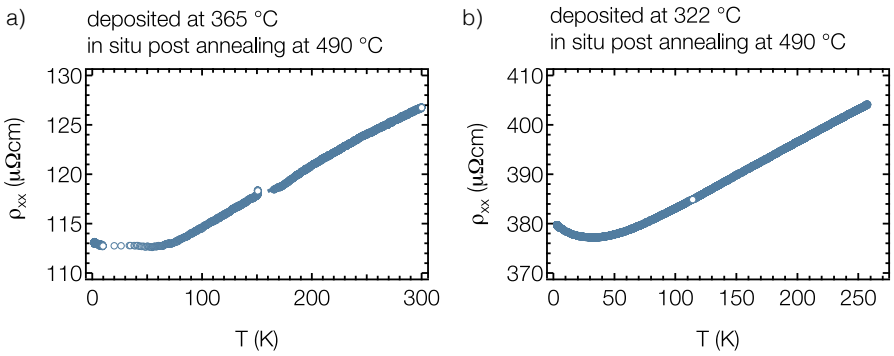

Figure 3.24. a) Temperature dependence of the resistivity for Mn_2Fe_1Ga deposited at $T_{dep} = 365\,°C$ and in-situ post annealed at 490 °C. b) Temperature dependence of the resistivity for Mn_2Fe_1Ga deposited at $T_{dep} = 322\,°C$ and in-situ post annealed at 490 °C. Mn_2Fe_1Ga deposited at $T_{dep} = 365\,°C$ shows lower resistivity, compared to the sample deposited at 322 °C. At low temperatures the sample deposited at the higher T_{dep} reaches the lowest value of ρ_{xx} =113 μΩcm at 55 K and stays stable for temperatures down to 2 K. The sample deposited at lower T_{dep} shows a minimum resistivity of $\rho_{xx} = 377\,\mu\Omega cm$ at 30 K, which is slightly increasing for lower temperatures. This was attributed to impurity scattering, which is dominating at low temperatures.

$\rho_{xx} = 377\,\mu\Omega cm$ at 30 K, which is slightly increasing for lower temperatures. This can be explained by impurity scattering, which is dominating at low temperatures.[82] The grain structure of both samples is identical (measured using AFM (not shown here)), leading to the assumption, that the lower crystallinity, and thus the higher amount of impurities, due to the unordered crystallographic areas, might be responsible for the different behavior.

In-plane measurements of the sample prepared using the 2-step procedure ($T_{dep} = 365\,°C$), showed decreasing Hall voltage at high magnetic fields.[3] This allows to determine the perpendicular magneto-crystalline anisotropy for Mn_2Fe_1Ga, fabricated using this particular preparation procedure. Figure 3.25(a) shows in-plane and out-of-plane AHE measurements for this sample, measured at room temperature. As previously mentioned (Sec. 2.2.4) the decreasing Hall voltage with increasing in-plane field is caused by the tilt of

[3] In contrast to the samples prepared in one step, where no change of the effect was observed even at maximum applied field (see Sec. 3.3.2)

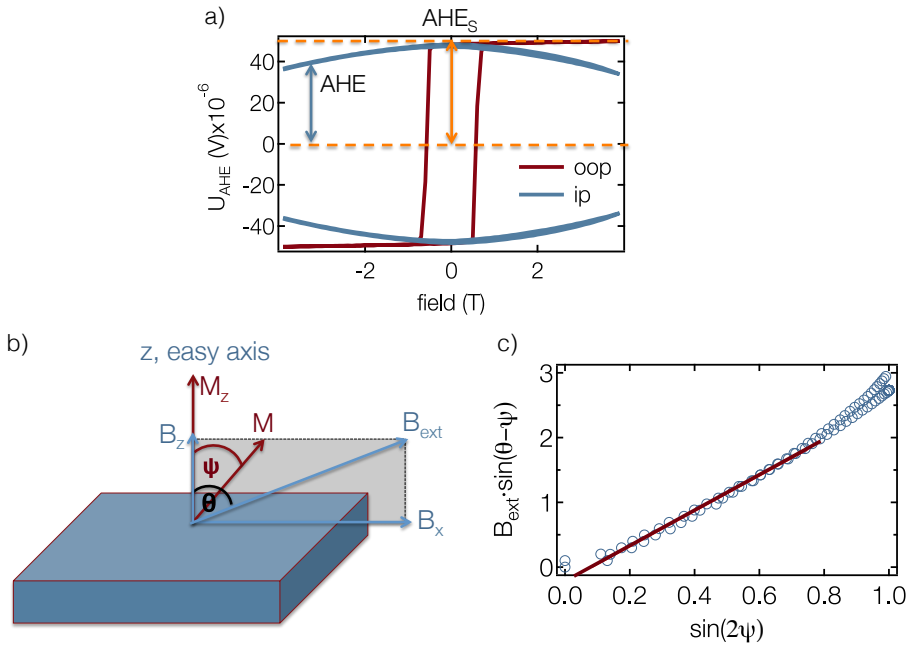

Figure 3.25. a) In and out-of-plane AHE measurements, measured at room temperature, for Mn_2Fe_1Ga deposited using the 2-step method and at $T_{dep} = 365\,°C$. The in-plane measurement curves show decreasing Hall voltage at high magnetic fields, which is a result of the slight tilt of the magnetization easy axis into the direction of the hard-magnetic axis. b) The geometries of the applied fields and tilt of the magnetization axes. c) The resulting graph of $\sin 2\psi$ plotted against $B_{ext}\sin(\theta-\psi)$, determined using equation 2.16. The slope of the corresponding linear fit (red line), gives the $\frac{K_U}{M_s}$ proportion.

the magnetization away from the magnetic easy axis. The measurement and evaluation technique is described in Sec. 2.2.4. The geometries of the applied fields and magnetization tilt are additionally illustrated in Fig. 2.11. The calculated values for $B_{ext}\sin(\theta-\psi)$ and $\sin 2\psi$, determined using equation 2.16, are plotted in Fig. 3.25(c). The slope of the corresponding linear fit, gives the $\frac{K_u}{M_s}$ proportion. The determined magneto-crystalline anisotropy of Mn_2Fe_1Ga is $(0.82\pm0.01)\,MJ/m^3$, which is close to the theoretically predicted value of $1.16\,MJ/m^3$.[70] High anisotropy energy is a necessary criterion for the implementation of the materials into spintronic devices, as MTJs, in order

to achieve thermal stability over at least a 10 years time frame. This criterion is thus fulfilled by the Mn_2Fe_1Ga compound.

3.3.3 Conclusion

In this section the structural, magnetic and electrical properties of sputter deposited Mn-Fe-Ga were presented. The difference between stoichiometric and off-stoichiometric samples, the influence of different substrate materials and deposition processes was investigated. Low roughness ($\leq 1\,\mathrm{nm}$) and the tetragonally distorted crystallographic phase ($D0_{22}$) were observed for each used deposition temperature and composition of the Mn-Fe-Ga on STO, whereas on MgO substrates the roughness showed strong dependence on the deposition temperature and the Mn-Fe-Ga composition. Strong PMA was confirmed for the tetragonally distorted structure. High coercive fields ($\mu_0 H_c \leq 2\,\mathrm{T}$) in the out-of-plane direction can be reached by tuning the composition. The magnetic and electrical properties are strongly influenced by the structure and stoichiometry of the sample. The lowest magnetic moment of $(0.51 \pm 0.05)\ \mu_B$/f.u. was determined for $Mn_{2.7}Fe_{0.3}Ga$. The resistivity of the stoichiometric samples is between $\rho_{xx} = 300\,\mu\Omega\mathrm{cm}$ and $\rho_{xx} = 410\,\mu\Omega\mathrm{cm}$. The lowest value ($\rho_{xx} = 90\,\mu\Omega\mathrm{cm}$) showed the off-stoichiometric $Mn_{3.0}Fe_{0.4}Ga$. Both composition types showed decreasing resistivity with decreasing Fe content in the samples.

Due to the high lattice misfit between the in-plane lattice constant of the $D0_{22}$ structure and the MgO substrates, the roughness of Mn-Fe-Ga deposited on MgO is very high (rms $> 2\,\mathrm{nm}$). Thus, a 2-step deposition process was carried out, in order to improve the surface properties of this compound. A successful improvement of the surface properties was achieved for Mn_2Fe_1Ga, deposited at 365 °C, followed by an in-situ post annealing process at 490 °C. The roughness was lowered to a value of 0.6 nm, the magnetic moment and the resistivity also showed lower values of $(0.36 \pm 0.04)\ \mu_B$/f.u. and $\rho_{xx} = 127\,\mu\Omega\mathrm{cm}$. It was shown, that the 2-step process improves the switching behavior, as well as the stability of the coercive field with decreasing temperature. Hence, it can be concluded that the optimum thin film composition and preparation parameters for the implementation into spintronic devices are Mn_2Fe_1Ga, deposited at 365 °C on MgO substrate, followed by an in-situ post annealing process at 490 °C. In the final analysis, the utilization of

the 2-step process improved the necessary properties for the use of Mn_2Fe_1Ga in future spintronic devices. It was found that this method is sensitive to composition changes and did not work for all investigated stoichiometries of Mn-Fe-Ga.

Chapter 4

TiN buffered Co-based Heusler compounds

In this chapter the influence of post annealing temperature on the crystallographic and magnetic properties of sputter deposited Co_2FeAl (CFA) and Co_2FeGe (CFG) thin films is investigated, with the focus on achieving surface induced perpendicular magnetic anisotropy of these materials by additionally conducting thickness dependency studies.

The chapter is divided into two parts: TiN buffered Co_2FeAl will be presented first, followed by the preparation and the presentation of the structural, magnetic and electrical properties of the double layer stacks Co_2FeAl/ MgO.

In the second part the results for TiN buffered Co_2FeGe are given. The preparation and the characterization of this compound, starting with the influence of the post annealing temperature on the structural and magnetic properties, is presented first. In order to find the right composition for achieving PMA, two additional compositions were tested: Fe_2CoGe and $Fe_{1.5}CoGe$.

4.1 Introduction

As already mentioned in the previous chapters, there are high demands on materials, that can be used in future spintronic or magnetic storage devices. High crystalline ordering and smooth interfaces are the basic requirements on the possible thin film systems. Those properties can only be achieved, if the lattice mismatch between the material and the substrate or seed layer is sufficiently small. Moreover a metallic seed-layer can be used as a conduction layer in applications as magnetic tunnel junctions, which is desirable. Commonly used seed layers are Cr ($a_{\mathrm{Cr}} = 2.88\,\text{Å}$) and Pt ($a_{\mathrm{Pt}} = 3.92\,\text{Å}$).[83] Co_2FeAl, which has a lattice constant of $a_{Heusler} \approx 5.7\,\text{Å}$, was already proven to grow epitaxially on Cr or MgO buffer layers.[84, 85]

Besides the low roughness and epitaxial growth of the compound, an out-of-plane oriented easy axis of magnetization is advantageous, in order to realize the requested cell minimization for information storage devices. Hence, materials with high perpendicular magnetocrystalline anisotropy (PMA) are investigated intensively. Another desired property, is the enhancement of thermal stability, which plays an important role in the emerging field of spin caloritronics, i.e., the combination of spintronics and thermoelectrics. Within this research field, various new effects were found, that might enable waste heat recovery in computer devices.[86]

To achieve high PMA, crystalline ordering of the Heusler compounds is important. For this, post-annealing processes need to be carried out at temperatures up to 300 °C. Previous investigations revealed a decrease of the PMA after the post annealing processes at higher temperatures.[83] The same behavior was observed for the tunneling magneto resistance (TMR) effect. The decrease of the TMR-effect is often explained by diffusion processes of the buffer layer material into the ferromagnetic electrode.[84, 87] According to previous investigations on Co-based multilayer systems for films with thicknesses around 1 nm, the PMA is attributed to hybridization of the Co or Fe 3d and O 2p orbitals, in case a neighboring oxide layer is present.[15, 16, 83, 88] Therefore, investigations of perpendicularly magnetized Co-based bilayer systems are usually performed on AlO_x, MgO or $MgAl_2O_4$ capped layer stacks.[14–17] In this work, MgO was used as a capping layer, in order to provide the PMA in the bilayer systems and also in order to investigate the

compatibility of MgO as tunnel barrier and Co_2FeAl as the on top or above deposited electrode material.

The Co_2FeGe compound is already well investigated theoretically and experimentally for bulk samples and thin films. Theoretical calculations predict a spin polarization of 99.3% [12] and a low damping parameter ($\alpha < 0.0025$) [89]. However, only one publication addresses the investigation of perpendicular magnetic anisotropy of this compound, in the composition $Co_{20}Fe_{50}Ge_{30}$.[90] PMA was achieved for RF magnetron sputter deposited 1.2 nm thin CoFeGe, on MgO (001) single crystalline substrates. The thin films were post annealed for 2 hours at 250 °C with applied perpendicular magnetic field of 1400 Oe. $B2$ crystalline ordering and a perpendicular magnetic anisotropy energy of $2 \cdot 10^6\,\mathrm{erg/cm^3}$ was extracted.

Due to these promising properties Co_2FeGe was chosen for further investigations in this theses. In a first step, the focus is on the characterization and investigation of sputter deposited Co_2FeGe thin films with 40 nm and 20 nm thicknesses, as well as the influence of post annealing temperature on the crystallographic and magnetic properties. In a second step, the presence of PMA of Co_2FeGe is investigated in a thickness series with thicknesses around 1.2 nm, which is the reported thickness value, in order to achieve PMA in this compound.[90]

4.2 TiN buffered Co_2FeAl compound

In this section the structural and magnetic properties of TiN buffered Co_2FeAl thin films, deposited on single crystalline MgO (001) substrates will be presented. The investigations focus on the influence of post annealing temperatures on the magnetic properties of Co_2FeAl thin films. PMA was achieved for the 0.9 nm and 1 nm thin samples. The origin of the PMA was attributed to the band splitting at the Co_2FeAl/MgO interface. The magnetic moments, deduced from XMCD measurements, are in good agreement with the expected values. Increasing the post annealing temperature up to 500 °C led to an increase of the squareness ratio and coercivity of the samples. This section is based on Niesen et al.[91].

Preparation

The TiN thin films were deposited in the BESTEC UHV sputtering system. Reactive sputtering in an Ar-N_2 atmosphere results in stoichiometric TiN thin films. During the sputtering process a N_2 flow of 2 sccm combined with 20 sccm Ar was used, leading to a pressure during deposition of 1.6×10^{-3} mbar. Because of the low lattice mismatch with TiN (below 0.7 %), (001) MgO single crystalline substrates were used. The substrate temperature was set to 405 °C in order to achieve epitaxial growth of TiN. After TiN buffer layer deposition and cooling down to room temperature, the samples were transferred to another sputtering chamber (HV), without breaking the vacuum. Stoichiometric Co_2FeAl was deposited at room temperature from a composite target at an Ar pressure of 2.3×10^{-3} mbar. The stoichiometry of Co_2FeAl was verified using the ICP-OES element analysis, resulting in Co_2FeAl (to be precise: $Co_{2.03}Fe_{1.00}Al_{0.995}$ was measured). On top of the Co_2FeAl a 2 nm thick MgO layer was deposited. After preparation, the layer stacks were ex-situ vacuum annealed at a pressure lower than 2×10^{-7} mbar for one hour, at different post annealing temperatures T_{pa} followed by field cooling in a magnetic field of 650 mT applied perpendicularly to the sample surface.

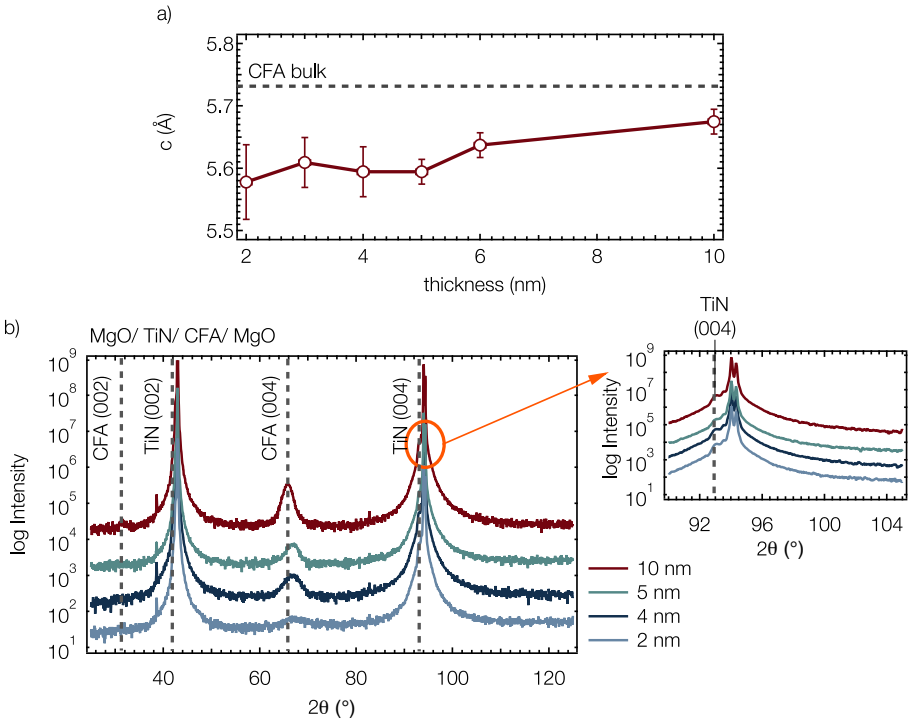

Figure 4.1. a) Out-of-plane lattice constant c measured using XRD scans. Decreasing layer thickness leads to decreasing c of the Co_2FeAl, due to the adjustment to the lattice of the TiN seed-layer. The bulk value of the lattice constant was reported by Gabor et al. [92]. b) XRD patterns of the TiN buffered Co_2FeAl (CFA) thin films for different layer thicknesses.

4.2.1 Structural properties

Figure 4.1 shows $\theta-2\theta$-scans of the as deposited Co_2FeAl layers with different thicknesses, deposited on 30 nm thick TiN seed-layers. The TiN diffraction peaks overlap with the MgO diffraction peaks, due to the low lattice mismatch (0.7 %). Only a shoulder was observable next to the MgO reflection. The estimated lattice constant of TiN (4.25 Å) is in good agreement with the reported value.[73] The (002) superlattice peak and the fundamental (004) reflection of the Co_2FeAl can be observed for the 10 nm sample, even in the as deposited state (see Fig. 4.1(b)). Measurements employing a 4-circle goniometer, revealed the absence of the (111) superlattice reflection, which would be an

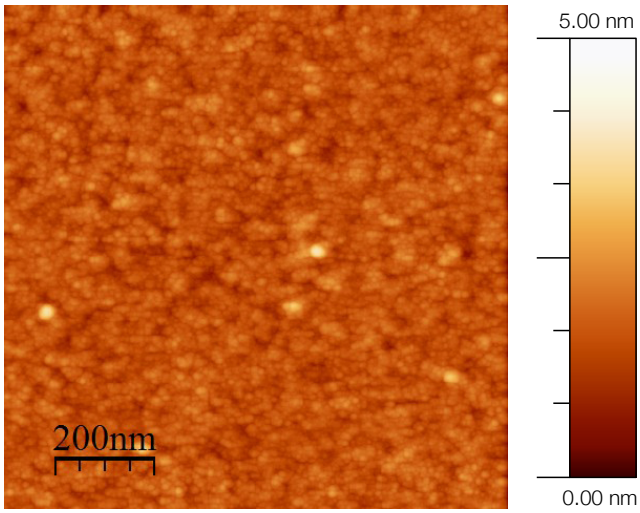

Figure 4.2. Atomic force microscopy image (1 μm^2) of a 10 nm thick Co_2FeAl layer deposited at room temperature on a 30 nm TiN seed-layer. The determined rms surface roughness is 0.3 nm.

evidence for the presence of the ordered Heusler $L2_1$ structure. However, partial $B2$ crystalline order is verified even in the as deposited state. With decreasing film thickness, the structure of Co_2FeAl adjusts to the lattice of TiN, leading to a decrease of the out-of-plane lattice constant (see Fig. 4.1(a)). Furthermore, the low out-of-plane lattice constant of 5.6 Å for the thin layers ($\leq$6 nm thickness), as well as the missing superlattice peak (002), point to the formation of the fully disordered $A2$ phase, in agreement with the literature.[93] For thicker films, epitaxial growth of the Co_2FeAl compound, rotated by 45° relative to the TiN seed-layer, was verified using a ϕ scan of the (202) reflection. The epitaxial relationship $Co_2FeAl(001)[100] \parallel TiN(001)[110]$ was therefore confirmed for these films. Atomic force microscopy measurements were used in order to investigate the surface properties and grain structure of TiN buffered Co_2FeAl. Figure 4.2 shows an AFM image of a 10 nm Co_2FeAl layer deposited at room temperature on a TiN seed-layer. The determined rms roughness of the film surface is (0.3 ± 0.05) nm. For low thicknesses the roughness does not significantly change. The measured rms roughness of the 1 nm thin Co_2FeAl is (0.4 ± 0.05) nm. The post annealing processes also do

not influence the roughness of CFA. The determined roughness of the 10 nm film, post annealed at 360 °C, is (0.3 ± 0.03) nm, and therefore fulfills the requirements for the use of this material as an electrode in spintronic devices as for example MTJs.

4.2.2 Magnetic properties

The magnetic properties were investigated using the magneto optical Kerr effect (MOKE) using a laser wavelength of λ=488 nm. The in- and out-of-plane hysteresis curves were measured by two detectors in different geometries. The measurements were performed using a system, which provides magnetic fields up to 300 mT. The measurement procedure is described in Sec. 2.2.3. The experimental setup is shown in Fig. 2.8(a).

Figure 4.3 shows the measured out-of-plane hysteresis curves for the three lowest layer thicknesses and four selected post annealing temperatures. The maximum slope of the Kerr rotation versus field curve increases for the 0.8 nm Co_2FeAl film, from 0.06$\frac{\text{mdeg}}{\text{mT}}$ to 0.16$\frac{\text{mdeg}}{\text{mT}}$ for T_{pa}= 280 °C to 340 °C, and drops to the initial value in case of further increase of the post annealing temperature. The absence of any remanence indicates that the out-of-plane direction is the magnetic hard axis, thus, for this layer thickness PMA could not be achieved. The 0.9 nm thin CFA film shows perpendicular magnetic anisotropy already at T_{pa}=325 °C. In case of the 1 nm thin film, PMA was achieved at T_{pa}=380 °C.

Figure 4.4 shows a comparison of the squareness ratio S_R, i.e., the ratio of the remanent magnetization and the saturation magnetization, and the coercive field H_C measured with magnetic field applied perpendicular to the film surface, for the 0.9 nm and 1 nm thick Co_2FeAl layers. The S_R of the 0.9 nm thin film increases with increasing post annealing temperature. It reaches the maximum value of one for T_{pa}=325 °C and remains stable for temperatures up to 500 °C. The coercive field of the 0.9 nm layer also increases with the post annealing temperature starting from values around 1 mT at 300 °C to 33 mT for T_{pa}=500 °C.

Compared to Cr buffered Co_2FeAl thin films, where the PMA was destroyed at a post annealing temperature of 375 °C [94], TiN buffered samples show high thermal stability at least for temperatures up to 500 °C. This property can be attributed to the thermal stability of the TiN seed-layers, which was confirmed in previous investigations.[73]

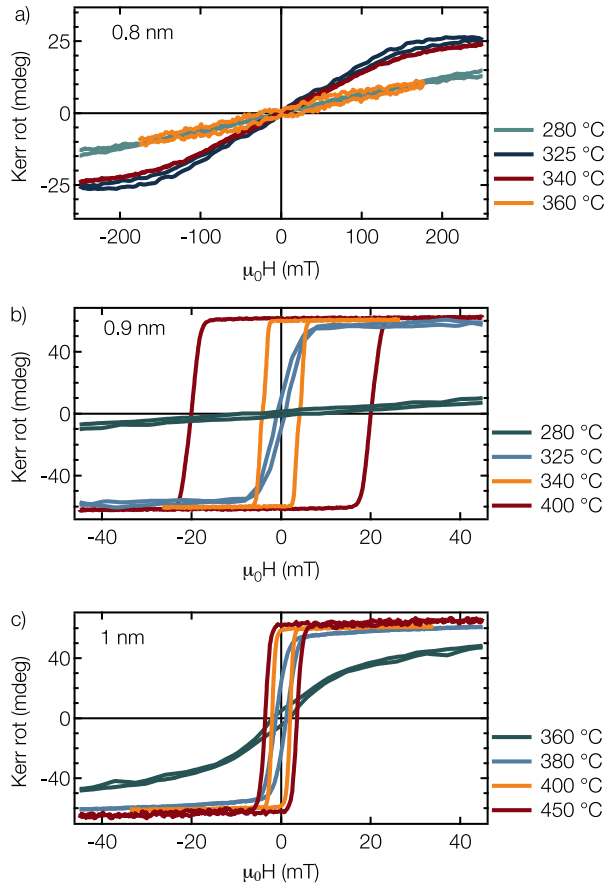

Figure 4.3. Out-of-plane hysteresis loops of TiN buffered Co_2FeAl layers, post annealed at temperatures between 280 °C and 450 °C. The Co_2FeAl layer thickness is a) 0.8 nm, b) 0.9 nm and c) 1 nm. The post annealing temperature has a strong influence on the magnetic properties of the compound. PMA was achieved for the 0.9 nm and 1 nm Co_2FeAl layer thickness.

Anisotropy measurements of in-plane magnetized 10 nm and 2 nm thin Co_2FeAl layers, revealed a two-fold magnetic anisotropy with the hard axis in $[\bar{1}10]$ and an easy axis in [110] direction of the Co_2FeAl (see Fig.4.5). Since the in-plane anisotropy is the same for both thicknesses, it can be concluded that the structure of the material does not significantly change with decreas-

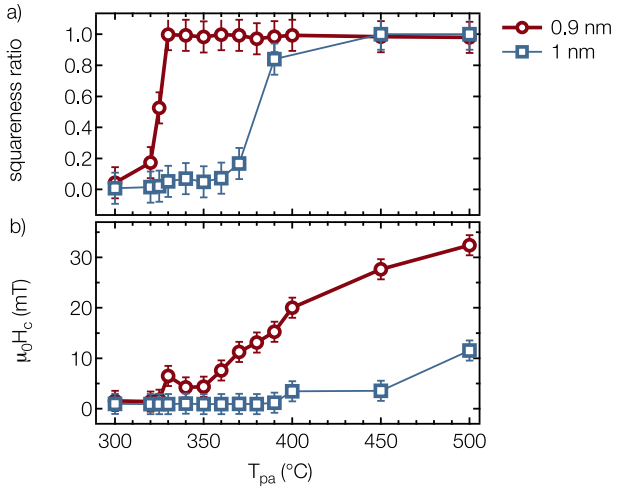

Figure 4.4. Dependence of a) the squareness ratio S_R and b) the coercive field $\mu_0 H_C$ for the 0.9 nm and 1 nm thick Co_2FeAl layers on the post annealing temperature T_{pa}. The 0.9 nm thin Co_2FeAl layer shows S_R of 1 and thus PMA at T_{pa} =320 °C. For T_{pa}>380 °C perpendicular magneto-crystalline anisotropy was also reached for the 1 nm thin Co_2FeAl layer. The coercivity increases with increasing T_{pa} for both layer thicknesses.

ing film thickness. The appearance of two-fold anisotropy for thin Co_2FeAl layers was observed for several substrates and buffer materials (in contrast to the four-fold anisotropy, which is usually expected for materials with cubic crystallographic structure).[14, 27, 92, 95, 96] Gabor et al. attributed the in-plane uniaxial anisotropy, to the presence of chemical disorder in the films. [92]. Wang et al. claimed, that the in-plane anisotropy is caused by the lattice misfit of −4.5% between the MgO and the Co_2FeAl.[96] The lattice misfit between the TiN seed-layer and the Co_2FeAl is around 6%, which is even higher compared to the MgO. Therefore, the uniaxial magnetic anisotropy might be caused by stress inside the Co_2FeAl, due to the lattice misfit between the Heusler and the seed-layer.

The chemical disorder, indicated by the crystallographic and XMCD measurements (see following section), could be another possible reason for the two-fold magnetic anisotropy.

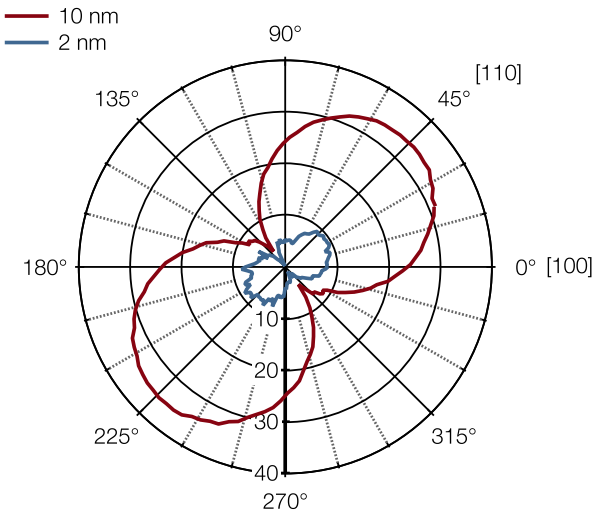

Figure 4.5. Azimutal angular dependence of the MOKE remanence (in mdeg) of TiN buffered 10 nm and 2 nm thin Co_2FeAl layers. An in-plane two-fold anisotropy with the easy axis oriented in [110] direction and the hard axis pointing into the [100] direction was observed. The Kerr signal of the 2 nm thin film was multiplied by a factor of 3 for a better comparison.

X-ray absorption spectroscopy

The element specific magnetic properties of TiN buffered Co_2FeAl, were investigated on a 1 nm thin layer. Surface sensitive total electron yield (TEY) was recorded at room temperature (sampling depth of 2 nm to 5 nm). The investigated sample was post annealed at 380 °C and is therefore out-of-plane magnetized. Figure 4.6 shows the XAS spectra of Co and Fe. I_+ and I_- are the measured intensities of the total sample current for parallel and antiparallel alignment of the magnetic field and the polarization. Both absorption edges (L_3 and L_2) of Co and Fe do not show any multiplet structures, which proves that the samples are free from oxidation. The resulting XMCD difference (I_+-I_-) is shown in the graphs below. To extract the element specific total magnetic moments (m_{tot}=m_{spin} + m_{orb}) sum rule analysis was carried out [50] leading to $m_{tot} = (1.38 \pm 0.22)\,\mu_B$/atom for Co and $m_{tot} = (2.68 \pm 0.22)\,\mu_B$/atom for Fe. The number of 3d holes, used for the analysis, was determined using SPR-KKR band structure calculations.[97] In case of Co_2FeAl the values are

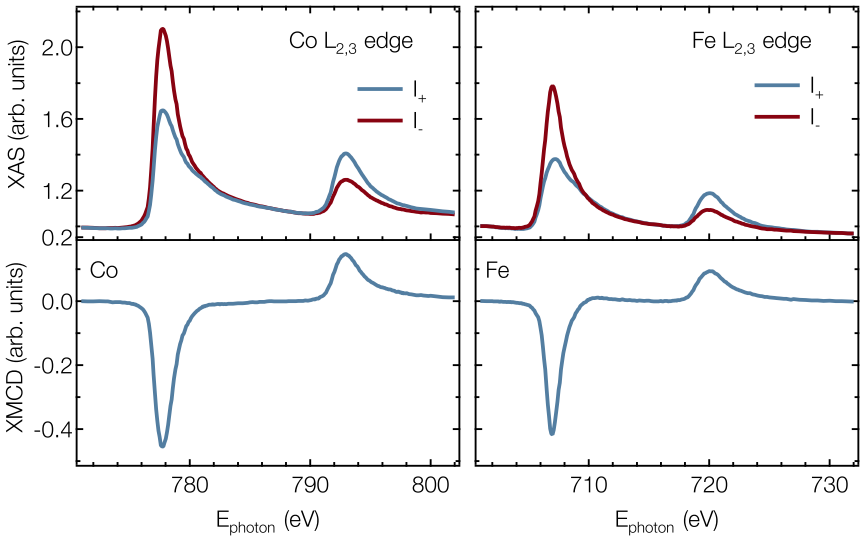

Figure 4.6. X-ray absorption and X-ray magnetic circular dichroism data of a 1 nm thin Co_2FeAl layer, post annealed at 380 °C. Co and Fe L_3 and L_2 edges do not show any multiplet structures, which is an evidence that both elements are not oxidized. Sum rule analysis yields to $m_{tot} = (1.38 \pm 0.22)\,\mu_B$/atom for Co and $m_{tot} = (2.68 \pm 0.22)\,\mu_B$/atom for Fe. The resulting total moment of Co_2FeAl is $(5.4 \pm 0.4)\,\mu_B$/f.u.

1.93 for Co and 3.29 for Fe. The magnetic moment of Co is higher than the predicted value of $1.14\,\mu_B$/atom and the evaluated value for Fe is lower, compared to the predicted value of $2.81\,\mu_B$/atom.[98] The enhancement of the Co orbital and total magnetic moment can be induced by an *A*2 like disorder of the crystalline structure [99], which is in agreement with the vanishing (002) reflex in the x-ray diffraction patterns (see Fig. 4.1). The resulting total moment of Co_2FeAl ($m_{Co_2FeAl} = 2 \cdot m_{Co} + m_{Fe}$) is $(5.4 \pm 0.4)\,\mu_B$/f.u. This corresponds to the reported value by Ebke et al. and the predicted value for Co_2FeAl of $4.99\,\mu_B$/f.u.[98] The deviation from the expected value, might be due to the enhancement of the Co orbital and total magnetic moment, caused by the chemical disorder inside of the films, as mentioned above.

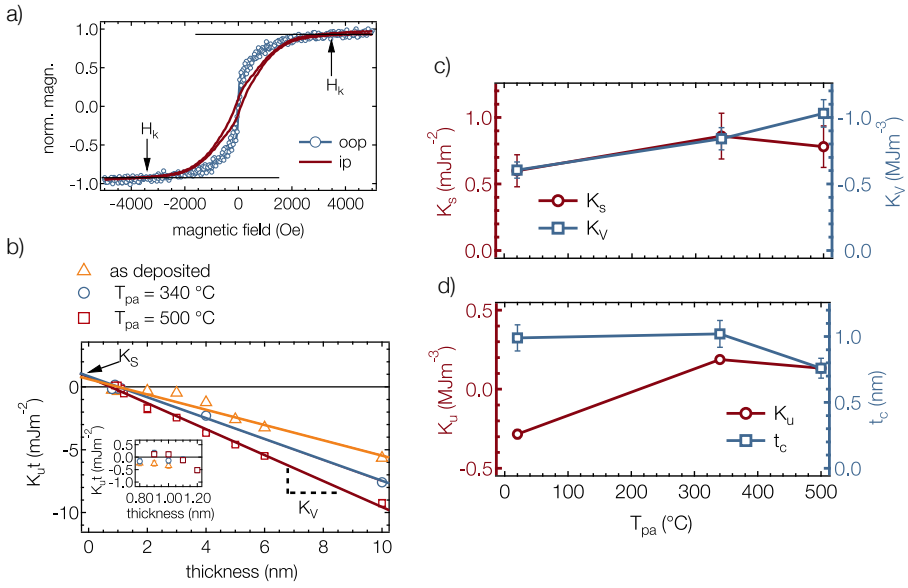

Figure 4.7. a) Normalized out-of-plane and in-plane magnetization curves for the 0.9 nm thin Co_2FeAl film. The arrows indicate the position at which the anisotropy field H_K is determined. b) $K_u t$ plotted against the layer thickness for the as deposited samples and two different post annealing temperatures. The inset shows a closer look into the lowest deposited film thicknesses. Slope and x-axis intersection of linear fits to the data are used to determine the bulk anisotropy energy density K_V and the interfacial anisotropy energy density K_S, respectively. c) Dependence on the post annealing temperature of the interfacial anisotropy energy density K_S (left axis) and the bulk anisotropy energy density K_V (right axis). d) The magnetic anisotropy energy density K_u of the 0.9 nm thin Co_2FeAl (left axis) and the calculated critical thickness t_c (squares) for the as deposited sample, as well as the two chosen post annealing temperatures (right axis).

Magnetic anisotropy

The perpendicular magnetic anisotropy energy density K_u was calculated using $K_u = \frac{\mu_0 M_S H_K}{2}$.[100] The saturation magnetization M_S of Co_2FeAl was obtained using AGM measurements and verified using vibrating sample magnetometry measurements (VSM) on a 10 nm thin Co_2FeAl layer. It is around (1140 ± 60) kA/m, which is in good agreement with the values measured by Ebke et al. for 20 nm thin, MgO buffered, Co_2FeAl (1099 kA/m) and Wen et al. for

Co_2FeAl films on a Cr buffer layer (1050 kA/m).[83, 97] H_K is the anisotropy field, i.e., the saturation field of the hard magnetic axis, deduced from the magnetometry and Kerr effect measurements. Figure 4.7(a) exemplarily shows AGM measurements with the magnetic field applied in the out-of-plane (oop) and in-plane (ip) direction, for an 0.9 nm thin Co_2FeAl film, as deposited. The arrows mark the positions, where the anisotropy field H_K is reached. It is set to be negative, if the easy axis of the magnetization is parallel to the sample surface. Therefore, K_u is positive for samples, which showed perpendicular magnetic anisotropy.

There are two contributions to the magnetic anisotropy energy density K_u: the bulk anisotropy energy density K_V and the interfacial anisotropy energy density K_S leading to the relation $K_u = K_V + \frac{K_S}{t}$, which is just a weighted average of the magnetic anisotropy energy of the interface and bulk.[100] Both contributions can be determined using a plot of $K_u t$ against the film thickness t (see Fig. 4.7(b)). The intercept of the linear fit at zero Co_2FeAl thickness, gives the interfacial anisotropy energy density K_S, the bulk anisotropy energy density K_V can be extracted from the slope.

Previous investigations of MgO buffered Co_2FeAl layers revealed, that the post annealing processes do not have significant influence on the magnetization.[97] Assuming a cubic structure with a lattice constant of 5.58 Å (measured for the 2 nm thin film) the calculated total magnetic moment, obtained using XMCD measurements, leads to a magnetization of $M_S = (1153 \pm 85)$ kA/m, which is in agreement with the value obtained using the VSM measurement. Therefore, the same magnetization value for all calculations of the magnetic anisotropy energy was used.

The values of K_S and K_V are plotted in Fig. 4.7(c). As can be seen, the interface anisotropy K_S for T_{pa}=340 °C is higher compared to the as deposited value. Here, a decrease of the interface anisotropy from (0.86 ± 0.16) mJm^{-2} for T_{pa}=340 °C, to (0.78 ± 0.15) mJm^{-2} for T_{pa}=500 °C was observed. The bulk anisotropy K_V is increasing from (-0.61 ± 0.05) MJm^{-3} for the as deposited sample, to (-1.03 ± 0.04) MJm^{-3} for T_{pa}=500 °C. The results show, that the bulk anisotropy is dominated by the demagnetizing field ($-\frac{1}{2}\mu_0 M_S^2$). The resulting deviation of 19.6 % to the demagnetizing field, can be a result of increased strains inside the Co_2FeAl films, due to the lattice mismatch with the TiN seed-layer.

The positive value of K_S confirms that the PMA is induced by the interface.[88] Additionally, the increase of K_S for T_{pa}=340 °C, indicates that especially the Co_2FeAl/MgO interface is responsible for the PMA, due to improvement of the lattice between the two materials with increasing temperature (see Fig. 4.7(d)).[15, 17, 101] The lowered interface anisotropy observed for T_{pa}=500 °C for all three investigated Co_2FeAl film thicknesses, combined with the observed non-linear behavior of K_ut (see inset in Fig. 4.7(b)), indicates that the thin Co_2FeAl layers might be influenced by interdiffusion, which is a possible reason for non-linear correlation between the magnetic anisotropy and the layer thickness. Same behavior was observed for the Co/Pt, Co/Pd or Co/Au multilayer systems.[100]

The critical thickness $t_c = -\frac{K_S}{K_V}$ is reached, when the interfacial anisotropy exceeds the bulk anisotropy (right axis of Fig. 4.7(d)). The maximum critical thickness, calculated with the values deduced from the linear fits, is 1.02 nm for the post annealing temperature of T_{pa}=340 °C. It decreases, with increasing post annealing temperature.

The maximum value of the perpendicular magnetic anisotropy energy density, measured for 0.9 nm thin Co_2FeAl post annealed at T_{pa}=340 °C is 0.19 MJ/m^3 (see left axis of Fig. 4.7(d)), which is comparable to the PMA values of CoFeB/MgO systems [13] and to the results of Wen et al. for Cr buffered Co_2FeAl thin films.[83]

4.2.3 Electrical properties

The resistivity values of the TiN/Co_2FeAl bilayer systems were measured using a four probe technique (see Sec. 2.2.3) and were conducted at room temperature. Under the assumption that the layer system is a parallel circuit, the resistivity of Co_2FeAl was calculated using the following formula:

$$\rho_{Co_2FeAl} = \frac{\rho_{TiN}\rho_{tot}}{\rho_{TiN} - \rho_{tot}} \tag{4.1}$$

with the resistivity of the TiN buffer layer ρ_{TiN} (determined using a single TiN layer, deposited during the same sputtering time) and the measured total resistivity of the layer system ρ_{tot}. Due to the fact, that the total resistance of the parallel circuit must be lower than the lowest value of partial resistance, the highest measured resistivity value of sputter deposited TiN single layer

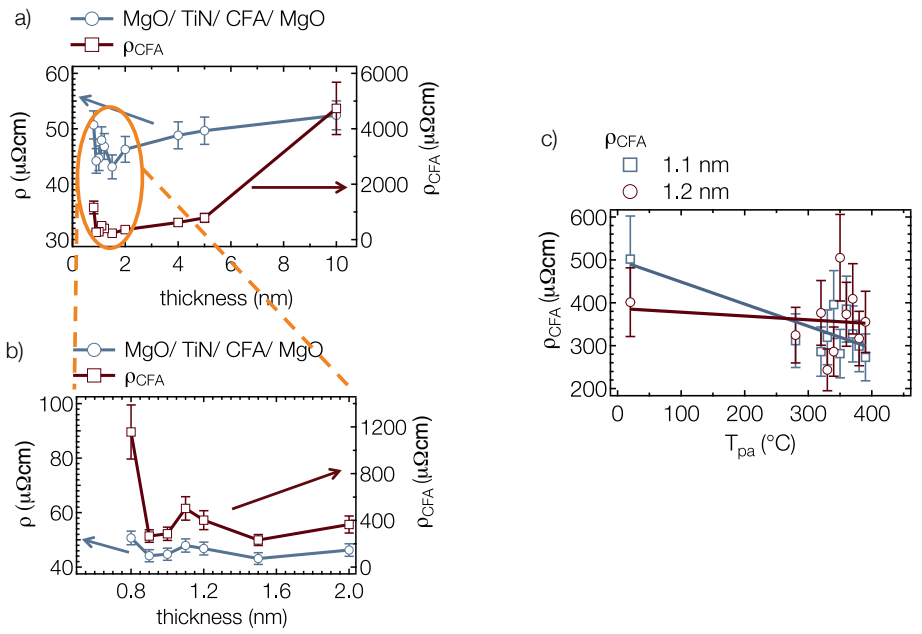

Figure 4.8. a), b) Left axis: Resistivity of the TiN buffered Co_2FeAl layer system (blue circles); Right axis: calculated resistivity of the Co_2FeAl thin films (red curve) in dependence on the film thickness. The resistivity of the whole layer system ranges between 46 μΩcm and 43 μΩcm for Co_2FeAl thicknesses of 0.9 nm to 2 nm and strongly increases for higher thicknesses. c) Comparison of the post annealing temperature dependence of the calculated resistivity for 1.1 nm and 1.2 nm thin Co_2FeAl films. Due to the high scattering of the resistivity values, it is not possible to determine the influence of T_{pa} on the resistivity for these two layer thicknesses.

(deposited under the same conditions as used for the buffer layer) was used for the calculations of the bilayer systems resistivity, which is (53 ± 10) μΩcm. A lower resistivity value of the TiN would lead to a negative resistivity of the CFA, and the calculations would not be valid.

Figure 4.8(a) and (b) show the measured resistivity values for the whole layer system (left axis) and the calculated resistivity of the Co_2FeAl single layer (right axis) in dependence on the thickness of the Co_2FeAl. As can be seen, the resistivity of the whole layer system ranges in between values of 46 μΩcm and 43 μΩcm for Co_2FeAl thicknesses of 0.9 nm to 2 nm. Only the system with 0.8 nm Co_2FeAl thickness and thicknesses higher than 2 nm show

increased resistivity. Still, the resistivity of the whole stack (TiN/ Co_2FeAl) is below 53 µΩcm. The calculated Co_2FeAl resistivities in the thickness range of 0.9 nm to 2 nm are 232 µΩcm to 370 µΩcm. The increased resistivity of the layer system with 0.8 nm Co_2FeAl can be explained by the fact, that the Co_2FeAl layer is not homogeneously distributed over the whole sample area and is not continuous. Hence, the insulating MgO layer might be located between the Co_2FeAl islands, thus, leading to an increase of resistivity. The 10 nm Co_2FeAl sample shows strong increase of the resistivity. Regarding that the measured resistivity of the whole stack equals to the resistivity of the assumed resistivity of the TiN layer, it is not possible to determine a convincing value for this Co_2FeAl layer thickness.

The influence of the post annealing temperature on the resistivity was investigated for the 1.1 nm and 1.2 nm thin Co_2FeAl layers (see Fig. 4.8(c)). Due to the high scattering of the resistivity values, it was not possible to determine the influence of T_{pa} on the resistivity for these two layer thicknesses of Co_2FeAl.

4.2.4 Conclusion

In this section the magnetic properties of TiN buffered Co_2FeAl thin films were investigated with the focus on the perpendicular magneto crystalline anisotropy. X-ray diffraction measurements confirmed partial *B*2 crystalline ordering of the Heusler compound on the TiN buffer layer even for the as deposited state. AFM measurements revealed low roughness of the bilayer systems of approximately 0.3 nm. Thickness and post annealing temperature dependence of the magnetic properties was investigated using MOKE measurements. In-plane anisotropy measurements revealed a two-fold in-plane magnetic anisotropy, which was attributed to chemical disorder and stress inside the films, caused by the high lattice mismatch between the TiN buffer layer and the Co_2FeAl thin films. PMA was achieved for the 0.9 nm and 1 nm thin samples. The origin of the PMA was attributed to the band splitting at the Co_2FeAl/MgO interface. The magnetic moments, deduced from XMCD measurements, are in good agreement with the expected values, although the Co magnetic moment is slightly higher. Increasing the post annealing temperature up to 500 °C led to an increase of the squareness ratio and coercivity of the samples. This indicates, that the layer systems are thermally

stable in the investigated temperature range. However detailed investigations of the interface anisotropy energy K_S, revealed decreasing behavior at for T_{pa}=500 °C, indicating that interdiffusion might be present at this post annealing temperature. The anisotropy energy density K_u is comparable to the previously observed values for Cr or MgO buffered Co_2FeAl and high enough for the possible use of this bilayer system in magnetic memory or storage devices.

The resistivity of the bilayer systems is below 50 μΩcm and stays stable for thicknesses between 0.9 nm and 2 nm and for temperatures up to 500 °C, which is advantageous for applications in electronic or spintronic devices.

With this, TiN is a suiting buffer material for the Heusler compound Co_2FeAl, improving the crystallinity, thermal stability and provides stability of the perpendicular anisotropy of this compound and therefore improving the applicability of Co_2FeAl in future spintronic devices.

4.3 TiN buffered Co_2FeGe compound

In this section, studies of TiN buffered Co_2FeGe thin films, deposited at room temperature using co-sputter deposition, are presented. The focus lies on the influence of post annealing temperature on the structural and magnetic properties of 10 nm and 20 nm thin Co_2FeGe films. In order to investigate the presence of perpendicular magnetic anisotropy (PMA) in sputter deposited Co_2FeGe films a thickness series with thicknesses of 0.8 nm, 0.9 nm, 1 nm, 1.1 nm, 1.2 nm, 1.5 nm and 2 nm was realized. Since this composition did not reveal any PMA, additional compositions (Fe_2CoGe and $Fe_{1.5}CoGe$) were investigated and will be introduced in the end of this section.

Preparation

The TiN buffered Co_2FeGe thin films were deposited in a BESTEC sputtering chamber. DC magnetron co-sputtering from pure Co, Fe and Ge targets was used to prepare the samples, in Ar atmosphere at a pressure of 1.7×10^{-3} mbar. The sample stoichiometries were determined using x-ray fluorescence (XRF) spectroscopy, measured on 40 nm thin Co_2FeGe films.

The TiN thin films preparation was conducted as described in Sec. 4.2. MgO (001) single crystalline substrates were used, because of the low lattice mismatch with TiN (below 0.7 %). The used substrate temperature was 405 °C in order to achieve epitaxial growth of TiN. On top of the Heusler compound a 2 nm thick Si layer was deposited to prevent the material from oxidation. After preparation, the layer stacks were ex-situ vacuum annealed at a pressure lower than 2×10^{-7} mbar for one hour at different post annealing temperatures T_{pa} followed by field cooling in a magnetic field of 650 mT.

4.3.1 Structural properties

Figure 4.9 shows $\theta - 2\theta$ XRD patterns of the TiN buffered Co_2FeGe layers for the as deposited state and different post annealing temperatures T_{pa}. As already mentioned in the previous sections, the TiN diffraction peaks overlap with the MgO diffraction peaks, due to the low lattice mismatch (0.7 %). Thus, only a small shoulder next to the MgO (004) reflection is visible. The

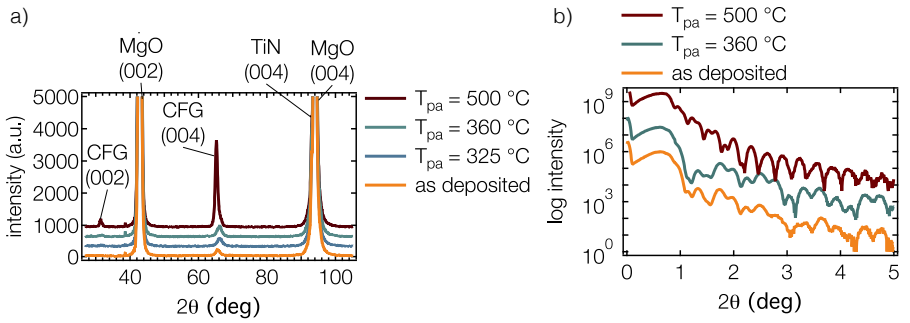

Figure 4.9. a) XRD patterns of TiN buffered, 20 nm thin Co_2FeGe films, deposited at room temperature and post annealed at different temperatures. For T_{pa} =500 °C the intensity of the fundamental (004) reflection is strongly increased, revealing an increase of the crystallinity of the sample. b) XRR measurements of the same samples for three chosen post annealing temperatures.

fundamental (004) reflection of the Co_2FeGe can be observed, even in the as deposited state (see Fig. 4.9(a)). For T_{pa} =500 °C the intensity of the fundamental (004) reflection is strongly increased. Thus the crystallinity of the sample increases for this post annealing temperature. The (002) superlattice peak appears after annealing the sample at 325 °C. Its intensity increases with increasing post annealing temperature, which is an evidence of an improved ordering and crystallization of the Co_2FeGe. The missing superlattice peak (002) for lower post annealing temperatures, points to the formation of the fully chemically disordered *A*2 phase.[93]

XRR measurements were carried out, in order to verify the roughness of the CFG thin films. Due to the multilayer system and therefore many parameters in the model, it was not possible to extract the exact roughness or density values of the single layers for this layer system from the XRR measurements (shown in Fig. 4.9 (b)). Hence, the surface roughness was investigated using AFM micrographs, as will be shown later. However, the absence of the dip in the XRR measurements, around $2\theta = 1.2$ deg for $T_{pa} = 500$ °C, indicates that a change of the interface properties is present. Figure 4.10 shows the evolution of the lattice constant *c* (Fig. 4.10(a)) and the FWHM (Fig. 4.10(b)) in dependence on T_{pa}. The lattice constant shows a minimum at $T_{pa} < 300$ °C, reaching 5.72 Å for $T_{pa} = 500$ °C, which is in agreement with the previously reported value.[102] The decrease of the lattice constant might be caused

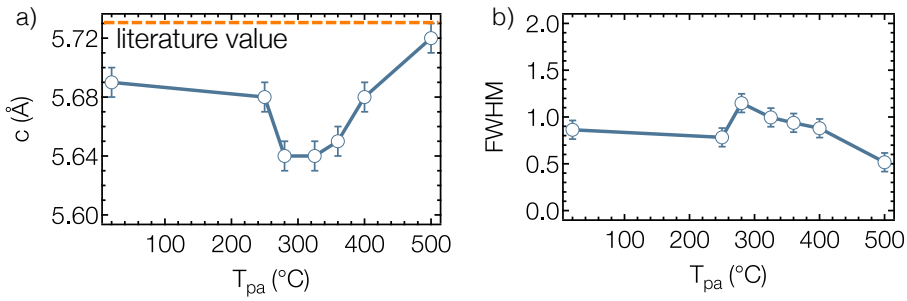

Figure 4.10. a) Lattice constant c of 20 nm thin Co_2FeGe in dependence on the post annealing temperature. b) FWHM of the rocking curves measured for the (004) Co_2FeGe-peak in dependence on the post annealing temperature.

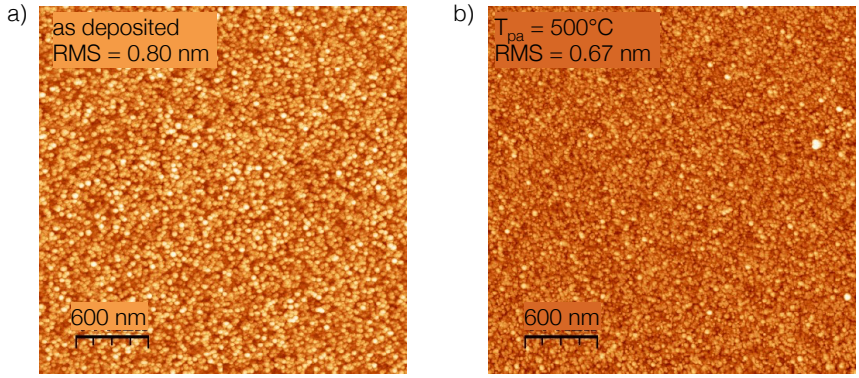

Figure 4.11. AFM micrographs ($3\,\mu m^2$) of 20 nm thin Co_2FeGe films for the as deposited state (a) and after the post annealing process at 500 °C (b). The determined rms roughness values are 0.8 nm for the as deposited sample and lower (0.67 nm) for the post annealed sample. Post annealing processes reduce the roughness without changing the overall surface morphology.

by a structural change or a redistribution of the atoms in the crystal lattice. The full width at half maximum (FWHM), extracted from the (004) reflection (see Fig. 4.10(b)) shows a maximum at $T_{pa} = 280\,°C$, indicating that the post annealing processes induce defects, e.g., dislocations or lattice misfit. For higher post annealing temperatures the FWHM decreases, indicating higher ordering degree with increasing T_{pa}.

In order to determine the surface roughness and investigate the grain structure of Co_2FeGe, AFM measurements were carried out. Figure 4.11 shows AFM micrographs of 20 nm thin Co_2FeGe, before and after annealing the sample at 500 °C. The determined rms roughness values are 0.8 nm for the as deposited sample and slightly lower (0.67 nm) for the post annealed sample. Regarding the grain structure, no obvious change was observed for these two post annealing temperatures.

4.3.2 Magnetic properties

The influence of the post annealing temperature on the magnetic properties of Co_2FeGe was investigated using a MOKE system, that provides magnetic fields up to 2 Tesla (see Sec. 2.2.3) and Fig. 2.8(b).

Figure 4.12(a) shows in-plane hysteresis curves of 20 nm Co_2FeGe layers for different post annealing temperatures. The extracted coercive fields and squareness ratios are plotted in Fig. 4.12(b) and (c). The measured values for 10 nm thin Co_2FeGe layers are added, in order to investigate the influence of the thickness. The coercivity of the Co_2FeGe for $T_{pa} \leq 500\,°C$ is increasing with increasing post annealing temperature in the range between $8\,Oe < H_C < 50\,Oe$ for the as deposited sample and $T_{pa} \leq 400\,°C$. After post annealing the sample at 500 °C, the coercive field increases by a factor of 10 for both layer thicknesses. The higher crystallinity, observed for the highest post annealing temperature of 500 °C is also visible in the magnetic behavior of Co_2FeGe with a drastic enhancement of the coercivity of this material. This also opens the possibility to adjust the magnetic properties of this compound to the individual needs, using different post annealing temperatures.

The squareness ratio, also determined from the MOKE hysteresis curves (Fig. 4.12(c)), does not significantly vary for the 20 nm thin Co_2FeGe and shows values around 1 even for the as deposited state. The 10 nm thin Co_2FeGe sample, reveals strong variations in dependence on the post annealing temperature. S_R decreases for temperatures up to $T_{pa} < 360\,°C$ and strongly increases for higher temperatures up to the maximum value of 1 for $T_{pa} = 500\,°C$. The dip in the squareness ratio is correlated with the behavior of the *c* lattice constant (see Fig. 4.10), indicating that the observed magnetic behavior is connected with the structural or crystallographic changes. The

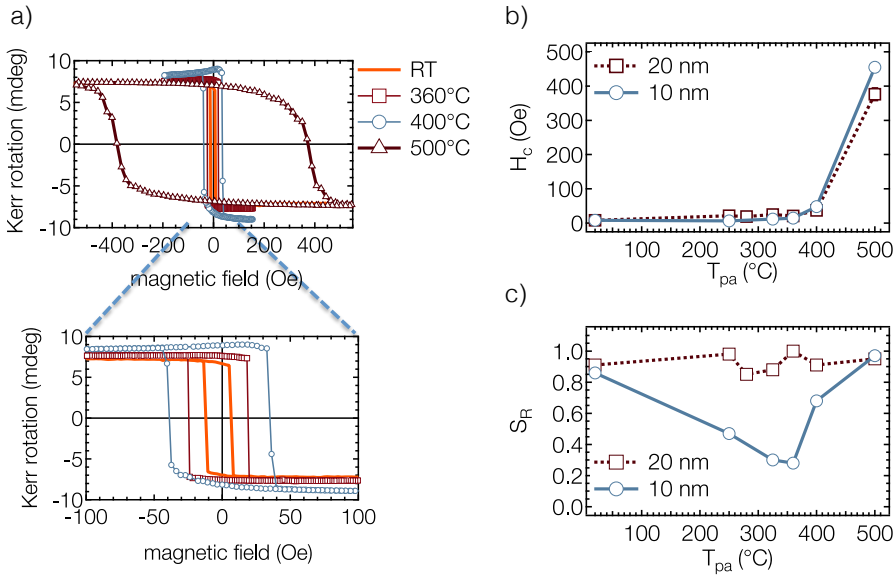

Figure 4.12. a) MOKE hysteresis curves comparison for 20 nm thin Co_2FeGe films post annealed at different temperatures up to 500 °C. b) Post annealing temperature dependence of the coercive field for 10 nm and 20 nm thin Co_2FeGe films. c) Post annealing temperature dependence of the squareness ratio for 10 nm and 20 nm thin Co_2FeGe films. At T_{pa}=500 °C the coercive field increases by a factor of 10 for both layer thicknesses. The structural change, observed for T_{pa}=500 °C is visible in the magnetic behavior of Co_2FeGe with a drastic enhancement of the coercivity.

increasing squareness ratio reinforces the assumption that a higher crystalline ordering is achieved for $T_{pa} = 400\,°C$ and $T_{pa} = 500\,°C$.

The atomic ordering in the crystal lattice influences the magnetic moments of the individual elements. Therefore, element specific magnetic behavior was investigated using XAS and XMCD measurements. Figure 4.13(a) shows the XAS and XMCD spectra of the 20 nm thin Co_2FeGe films post annealed at different temperatures. The spectra are shifted for better clarity. The spectra of both elements show no signs of oxidation in these samples. The bump in the Co spectra, approximately 4 eV above the L_3 absorption maximum (780 eV), is typical for Heusler compounds and an evidence of high crystalline ordering.[103] This is also supported by the fact, that this bump (additional peak) gets more pronounced for $T_{pa} = 500\,°C$, where the crystalline ordering

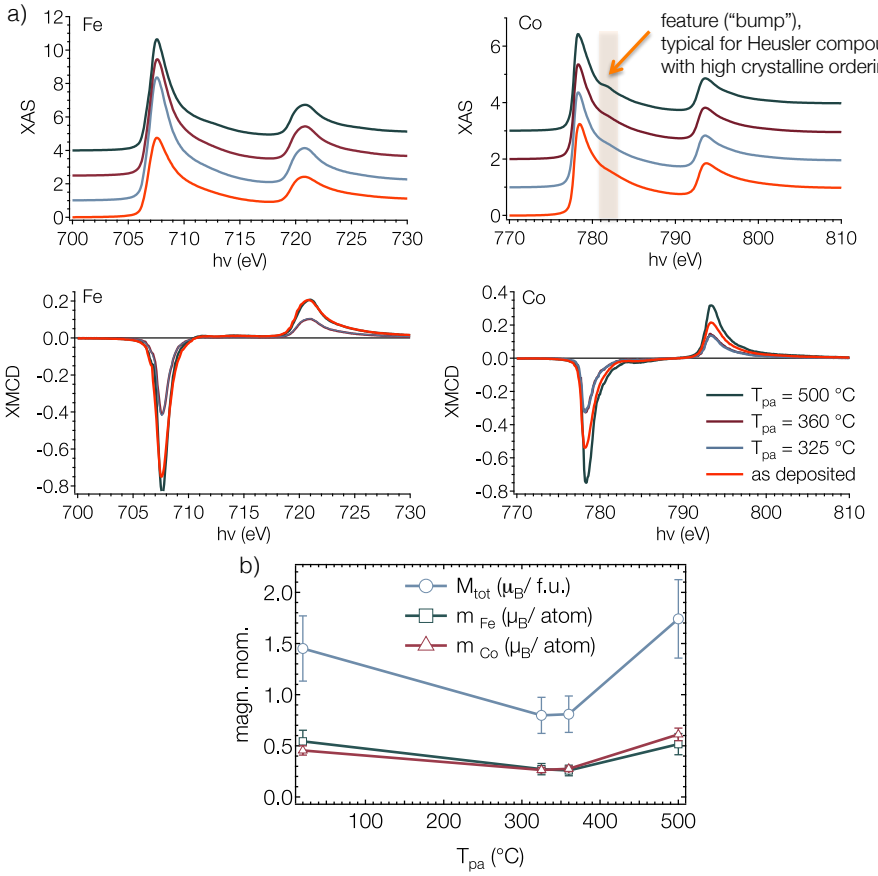

Figure 4.13. a) XAS and XMCD spectra of the Fe and Co elements in TiN buffered 20 nm thin Co_2FeGe films, for the as deposited state and three different post annealing temperatures. The observed feature ("bump", marked by an arrow) in the Co spectra for $T_{pa} = 500\,°C$, is an evidence of high crystalline ordering of the Heusler compound. b) Evaluated element specific magnetic moment values per atom (for Fe and Co) and the total magnetic moments per f.u. for Co_2FeGe in dependence on the post annealing temperatures.

is maximized, according to the XRD measurements. The appearance of this feature is explained by the hybridization of Co 3*d* and Ge 2*p* electronic states.[103] The magnetic moments were determined using the sum rule analysis, using the normalization and evaluation process, described in previous sections and given in [51].

The Co and Fe atoms show almost equal magnetic moments per atom for each post annealing temperature. The magnetic moments of both elements decrease slightly for temperatures up to 360 °C and increase for the highest post annealing temperature of 500 °C. The predicted value for the $L2_1$-type crystal structure of Co_2FeGe is around 5.7 μ_B/f.u.[104] Hence, the increasing magnetic moments are a hint to increasing atomic ordering of the compound with increasing post annealing temperature. At 500 °C the highest atomic order is achieved and therefore the magnetic moment of 1.8 μ_B/f.u. is reached. However, compared to the reported value for $L2_1$-type crystal structure of Co_2FeGe [104], the determined value for Co_2FeGe thin films is much lower. Possible reasons could be structural imperfections and distortion, due to the lattice misfit with the TiN buffer layer, as well as structural change to crystallographic phases with higher chemical disorder.

4.3.3 Outlook: Towards perpendicular magnetic anisotropy in Co-Fe-Ge

Thickness series of Co_2FeGe with thicknesses of 0.8 nm, 0.9 nm, 1 nm, 1.1 nm, 1.2 nm, 1.5 nm and 2 nm were realized and post annealed at 360 °C and 500 °C, with the aim of achieving perpendicular magneto crystalline anisotropy for this material. However, all samples showed in-plane oriented easy magnetization axis or were non-magnetic.

In order to test, whether PMA can be achieved for the Co-Fe-Ge system, preliminary investigations on different stoichiometries were carried out. In order to be able to investigate the crystallographic structure for these two stoichiometries, 20 nm thick films were prepared. In order to determine the bulk value of the magnetization for the two compositions, AGM measurements were also performed on the 20 nm thick films. MOKE measurements were used in order to identify the right film thickness, for achieving PMA in this compound. Figure 4.14 shows the XRD patterns of the two tested stoichiometries $Fe_{1.5}CoGe$ and Fe_2CoGe in the as deposited state, the AGM hysteresis curves for the same samples, as well as MOKE measurements of the samples, that exhibit an out-of-plane oriented magnetic easy axis.

As can be seen from the XRD patterns, Fe_2CoGe shows high crystallinity even in the as deposited state. Compared to $Fe_{1.5}CoGe$, the intensity of the

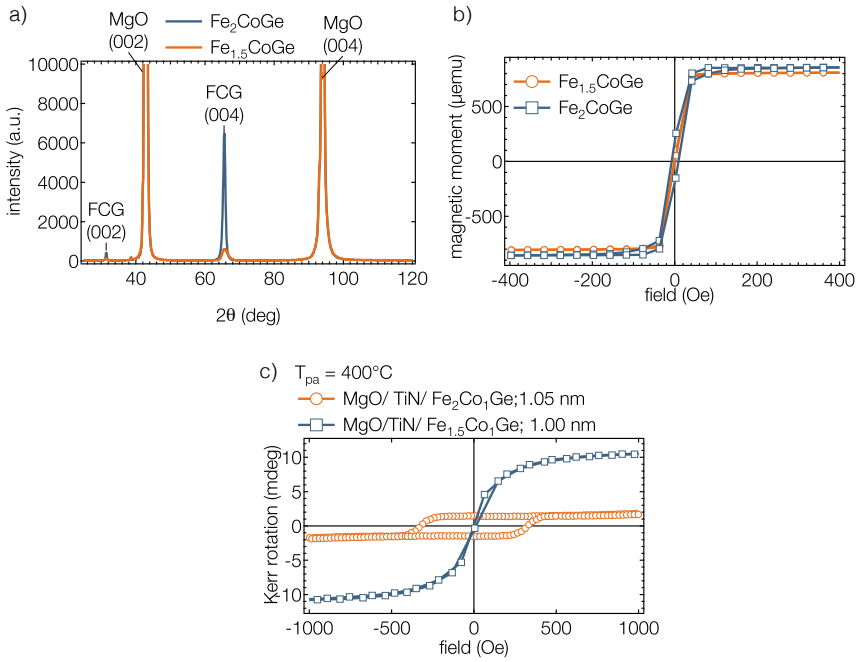

Figure 4.14. a) XRD patterns of the two tested stoichiometries $Fe_{1.5}CoGe$ and Fe_2CoGe in the as deposited state. b) In-plane AGM hysteresis curves for 20 nm thin $Fe_{1.5}CoGe$ and Fe_2CoGe. c) Out-of-plane MOKE measurements of 1.05 nm thin Fe_2CoGe and 1 nm thin $Fe_{1.5}CoGe$, both post annealed at 400 °C.

(004) reflection of Fe_2CoGe is one order of magnitude higher, which is an evidence for high crystallinity of this compound.

The magnetization and magnetic behavior for this compounds was tested using AGM and MOKE measurements. The 20 nm thin $Fe_{1.5}CoGe$ and Fe_2CoGe films show comparable magnetization values (given in Tab. 4.1). The measured total magnetic moments are in good agreement (within the error limits) with the reported values, where the element specific magnetic moments were determined to be Co = 1.43 μ_B/atom, Fe = 2.88 μ_B/atom, and Ge = 0.01 μ_B/atom.[12] Especially Fe_2CoGe shows high agreement with the predicted value for the $L2_1$ structure (see tab. 4.1), which is an evidence for high chemical ordering in these films, even in the as deposited state.

Table 4.1. Comparison of the magnetization values determined using AGM, calculated total magnetic moments, and squareness ratios (in-plane measured hysteresis curves) for as prepared Co-Fe-Ge 20 nm thin films.

sample	M (kA/m)	M (μ_B/f.u.)	S_R
Co_2FeGe	200 ± 22	1 ± 0.1	0.9
$Fe_{1.5}CoGe$	1100 ± 121	5.46 ± 0.8	0.3
Fe_2CoGe	1163 ± 128	5.77 ± 0.8	0.07

Thickness series of 0.9 nm, 1 nm, 1.05 nm, 1.1 nm, 1.2 nm and 2 nm for these two compositions of CFG were realized and investigated using MOKE measurements. PMA was achieved for 1.05 nm thin Fe_2CoGe film, after post annealing the sample at 400 °C (see Fig. 4.14(c)).

Ferromagnetic resonance (FMR) (in-plane) measurements[1] on $Fe_{1.5}CoGe$ revealed low magnetic damping, even in the as deposited state. The minimum value of $\alpha = 0.0047$ was measured for the 15 nm thin film, which is close to the reported value of $\alpha < 0.0025$.[89] Lower and higher thicknesses revealed increasing damping constants. The 20 nm thin $Fe_{1.5}CoGe$ showed a magnetic damping of $\alpha = 0.0055$. Further investigations and post annealing temperature dependence of the damping and magneto crystalline anisotropy for this compound are planed for future work.[2]

4.3.4 Conclusion

In this section the structural and magnetic properties of TiN buffered Co_2FeGe thin films were investigated. X-ray diffraction measurements confirmed partial B2 crystalline ordering even for the as deposited state. AFM measurements revealed roughness of the bilayer systems of approximately 0.8 nm. The influence of the post annealing temperature of the structural properties and magnetic properties revealed a decrease of the c lattice constant for temperatures up to 360 °C, which was attributed to chemical disorder and stress inside the films. High crystalline ordering was observed for the post annealing temperature of 500 °C. The coercivity is also strongly influenced by the post annealing process and shows a strong increase up to 400 Oe for the 20 nm

[1] Performed at the Technische Universität Kaiserslautern by Dr. Andrés Conca Parra
[2] Dr. Andrés Conca Parra, Technische Universität Kaiserslautern

thick and to 470 Oe for the 10 nm thick Co_2FeGe, after post annealing at 500 °C. XMCD measurements revealed low magnetic moments for Co and Fe, leading to a low total magnetic moment ($1.8\,\mu_B$/f.u.) of this compound. Since no PMA for the Co_2FeGe compound was observed, two additional stoichiometries of this compound were examined. Fe_2CoGe revealed high crystallinity even in the as deposited state. The magnetization for this stoichiometry is much higher, compared to the Co_2FeGe thin films. PMA was achieved for Fe_2CoGe at a thickness of 1.05 nm after post annealing the sample at 400 °C.

Therefore, TiN buffered Fe-Co-Ge is a promising material for spintronic applications, showing low roughness, high crystallinity, low magnetic damping constant and perpendicular magnetic anisotropy at low thicknesses. For a better comparison with other compounds, more detailed investigations of the surface morphology, the electrical and magnetic properties of Fe_2CoGe need to be carried out. These results only provide the first tests of the properties of Co-Fe-Ge.

Chapter 5

Summary & Outlook

This work is mainly aiming to find and investigate *novel* materials with strong perpendicular magnetic anisotropy, which can also serve as a potential electrode for future spintronic applications, as well as magnetic memory devices.

The theses is divided in two parts: The investigation of Mn-based, tetragonally distorted compounds Mn-Fe-Ge and Mn-Fe-Ga, and the investigation of TiN buffered Co-based Heusler compounds Co_2FeAl and Co_2FeGe. The Mn-based compounds are predicted to show high PMA, as an intrinsic property, due to their tetragonally distorted crystal structure. For the Co-based Heusler compounds, surface induced PMA can be achieved by reducing the thickness down to 1 nm.

Through systematical variation of the preparation or materials parameters, as deposition temperature, stoichiometry, thickness or post annealing temperatures, PMA was observed for all materials, investigated in this work. In the following, a summary of the properties will be given separately for each of the investigated materials.

The Mn-Fe-Ge compound shows the desired tetragonally distorted phase in the stoichiometry range of ($0.3 \leq x \leq 1$) and deposition temperatures of 405 °C and 450 °C. Low magnetization ($\leq 0.16\ \mu_B$/f.u) and high coercive fields (up to 3.64 T) make this compound very promising for future sensor or spintronic applications.

The anisotropy constant K_u was determined to be around 0.3 MJ/m^3. The highest value of (0.36 ± 0.04) MJ/m^3 was determined for $Mn_{3.3}Fe_{0.7}Ge$.

$Mn_{3.7}Fe_{0.3}Ge$ did not reveal any measurable tilt of the magnetization out of the easy axis, even at an in-plane field of 4 T, thus indicating, that the anisotropy energy of this composition must be higher, which might be one possible issue for future investigations.

The resistivity of this compound ranges between 207 μΩcm and 457 μΩcm. The high resistivity of the Mn-Fe-Ge thin films was attributed to the presence of imperfections in the crystalline structure.

The strong sensitivity of the structural, magnetic and electrical properties of $Mn_{4-x}Fe_xGe$ to the composition, makes the Fe content x a handle to adjust the materials properties to the individual needs. However, the high roughness of the sputter deposited $Mn_{4-x}Fe_xGe$ is one issue, which needs to be solved. Still, Mn-Fe-Ge is a promising material to serve as a bottom electrode in perpendicular magnetic tunnel junctions, providing high stability agains external magnetic fields, due to its large coercive fields and low magnetic moments.

For Mn-Fe-Ga the difference between stoichiometric and off-stoichiometric samples, as well as the influence of different substrates and deposition processes was investigated. On STO, low roughness (≤ 1 nm) and the tetragonally distorted crystallographic phase ($D0_{22}$) was observed for each used deposition temperature and composition of the Mn-Fe-Ga, whereas on MgO substrates the roughness showed strong dependence on the deposition temperature and the Mn-Fe-Ga composition. It was shown, that the magnetic and electrical properties of this compound are strongly influenced by the structure and stoichiometry. High PMA was confirmed for the tetragonally distorted films, combined with high coercive fields ($H_c \leq 20$ kOe). The lowest magnetic moment (0.51 ± 0.05) μ_B/f.u. was determined for $Mn_{2.7}Fe_{0.3}Ga$. For stoichiometric $Mn_{3-x}Fe_xGa$ ($0.3 \leq x \leq 1$) the resistivity values are comparable to the resistivity measured for $Mn_{4-x}Fe_xGe$. The lowest value ($\rho_{xx} = 90$ μΩcm) showed the off-stoichiometric $Mn_{3.0}Fe_{0.4}Ga$. Both composition types (stoichiometric and off-stoichiometric) showed decreasing resistivity with decreasing Fe content in the samples.

The high lattice misfit between the in-plane lattice constant of the $D0_{22}$ structure and the MgO substrates leads to high roughness of Mn-Fe-Ga deposited on MgO (rms > 2 nm). An improvement of the surface properties of this compound was achieved by using a **2-step deposition process** involving moderate deposition temperatures T_{dep} and post annealing at $T_{pa} > T_{dep}$. Suc-

cessful refinement of the surface properties and magnetic switching behavior was achieved for Mn_2Fe_1Ga. Compared to the Mn_2Fe_1Ga deposited at high temperature (roughness of 3.4 nm), the roughness was lowered to a value of 0.6 nm. The magnetic moment and the resistivity also showed lower values of (0.36 ± 0.04) μ_B/f.u. and $\rho_{xx} = 127\,\mu\Omega$cm. Another advantage of the 2-step process, is the improved switching behavior, as well as the stability of the coercive field with decreasing temperature. Thus, the most promising compound for future applications is identified to be Mn_2Fe_1Ga, prepared using a 2-step process during sputter deposition.

The TiN buffered Co_2FeAl thin films were investigated with the focus on the perpendicular magneto crystalline anisotropy. Partial $B2$ crystalline ordering was confirmed even for the as deposited state. Low roughness of the bilayer systems (of approximately 0.3 nm) was measured using AFM. Thickness and post annealing temperature dependence of the magnetic properties was investigated using MOKE measurements. PMA was achieved for the 0.9 nm and 1 nm thin samples. The origin of the PMA was attributed to the band splitting at the Co_2FeAl/ MgO interface. The magnetic moments were deduced from XMCD measurements and showed good agreement with the expected values, although the calculated Co magnetic moment is slightly higher. Post annealing temperatures up to 500 °C were used and led to increasing squareness ratio and coercivity of the samples. This shows, that the layer systems are thermally stable in the investigated temperature range. The highest anisotropy energy density K_u of 0.19 MJ/m^3 was determined for 0.9 nm thin Co_2FeAl, post annealed at T_{pa}=340 °C. This value is comparable to the previously observed values for Cr or MgO buffered Co_2FeAl and also high enough for the possible use of this bilayer system in magnetic memory or storage devices. The measured resistivity of the bilayer systems is below 50 $\mu\Omega$cm and stays stable for thicknesses between 0.9 nm and 2 nm for temperatures up to 500 °C, which is advantageous for applications in electronic or spintronic devices.

In the last section, the structural and magnetic properties of **TiN buffered Co_2FeGe thin films** were presented. Partial $B2$ crystalline ordering, even for the as deposited state, was confirmed. AFM measurements revealed roughness of approximately 0.8 nm. Strong influence of the post annealing

temperature on the structural and magnetic properties of this compound, was observed. Highest crystalline ordering was determined for the post annealing temperature of 500 °C. The coercivity is strongly influenced by the post annealing process and shows a strong increase up to 400 Oe for the 20 nm thin, and 470 Oe for the 10 nm thin Co_2FeGe layer, after post annealing at 500 °C. Unexpected low magnetic moments ($1.8\,\mu_B$/f.u.) were determined using XMCD for this compound.

Two additional stoichiometries were investigated, with the purpose of finding PMA. **Fe_2CoGe** revealed high crystallinity even after room temperature sputter deposition. The magnetization of Fe_2CoGe is $(5.77 \pm 0.8)\,\mu_B$/f.u. and thus much higher, compared to the Co_2FeGe thin films. Still, in this case PMA was observed for 1.05 nm thickness and a post annealing temperature of 400 °C. Hence, TiN buffered Fe-Co-Ge is promising for spintronic applications, due to the low roughness, high crystallinity, low magnetic damping and perpendicular magnetic anisotropy at low thicknesses.

However, this work provides only the first tests of the properties of Co-Fe-Ge. Therefore, more detailed investigations of the surface morphology, the electrical and magnetic properties of Fe_2CoGe need to be carried out in the future.

As a final conclusion, these theses addresses the major issues for the implementation of Heusler compounds into spintronic devices, which were investigated thoroughly for four different materials.

The major topics are: the crystalline ordering, surface texture, magnetic properties and particularly PMA, as well as the electrical behavior of the investigated Heusler compounds. It was shown, that manifold parameters have an impact on the materials properties and thus need to be examined. Most notable is the challenge to find the balance between the need of a high deposition temperature, in order to achieve high crystallinity of the thin films, and the need of low deposition temperatures to minimize the surface roughness. The investigated materials, each reveal promising properties for the implementation into spin-transfer-torque devices. However, the implementation into spintronic devices, as well as the functionality and stability testing is still to be investigated.

The challenge of decreasing the roughness of Mn-based compounds is rarely discussed in the literature, and thus it is important to recognize this issue and find possible solution, as the described 2-step deposition process, which was

successfully deployed in this work. Another possible solution could be the use of different deposition techniques, as molecular beam epitaxy, for example, which can be one of the future projects.

The Co-based Heusler compounds are promising for future applications, due to the possibility of room temperature deposition. The challenge here, is to find a suitable buffer layer, which allows high quality crystalline growth of the compounds and is stable agains diffusion for high post annealing temperatures. TiN is one highly promising candidate, fulfilling all the required properties, as was shown in this work.

Performed pre-investigations for future work revealed, that TiN can be grown on amorphous SiO_2 substrates using a 10 nm seed-layer of MgO. SiO_2 is a commonly used material in the CMOS industry and thus it is beneficial to have materials or layer systems, which can be grown on the SiO_2 substrate directly.

Outlook

This work was aiming to discover and investigate novel Heusler, and Heusler related materials, for the implementation into future spintronic devices. This aim was met with high accuracy, hoping that the gained knowledge will contribute to further understanding of Heusler compounds, growth processes of sputter deposited thin films, and the influence of the manifold parameters, as composition of the compounds, deposition temperatures, substrate or seed-layer, and many many more.

Future work should focus on further improvement of the surface properties of the Mn-based compounds, followed by implementation of those into magnetic tunnel junctions. The TiN buffered Co_2FeAl was already successfully implemented in magnetic tunnel junctions with **in-plane** oriented magnetization switching. Not only a stable and high TMR effect (of 100%) was shown, but also a high tunneling magneto-Seebeck effect (also around 100%) was achieved, which enables the possibility of using these materials in energy conversion and waste heat recovery applications. A detailed description of this effects is given in [86].

The influence of the layer thickness and post annealing temperature for TiN buffered Co_2FeGe compound on the magnetic damping and anisotropy is

recently investigated using FMR studies at the Technische Universität Kaiserslautern by Dr. Andrés Conca Parra, which will strongly contribute to further understanding of this compound and hopefully pave the way to a successful implementation of this material in future applications.

Bibliography

[1] J. M. D. Coey, *Magnetism and magnetic materials* (Cambridge University Press, 2010).

[2] S. A. Wolf, Science **294**, 1488 (2001).

[3] G. Reiss and D. Meyners, English, Journal of Physics: Condensed Matter **19** (2007).

[4] A. Thomas, D. Meyners, D. Ebke, N.-N. Liu, M. D. Sacher, J. Schmalhorst, G. Reiss, H. Ebert, and A. Hütten, Applied Physics Letters **89**, 012502 (2006).

[5] D. Weller, A. Moser, L. Folks, M. E. Best, W. Lee, M. F. Toney, M. Schwickert, J. U. Thiele, and M. F. Doerner, "High *Ku* materials approach to 100 Gbits/in2", IEEE Transactions on Magnetics **36**, 10 (2000).

[6] S. Mangin, D. Ravelosona, J. A. Katine, M. J. Carey, B. D. Terris, and E. E. Fullerton, "Current-induced magnetization reversal in nanopillars with perpendicular anisotropy", Nat Mater **5**, 210 (2006).

[7] S. Ikeda, K. Miura, H. Yamamoto, K. Mizunuma, H. Gan, M. Endo, S. Kanai, J. Hayakawa, F. Matsukura, and H. Ohno, "A perpendicular-anisotropy CoFeB-MgO magnetic tunnel junction", Nat Mater **9**, 721 (2010).

[8] F. Heusler, Verhandlungen der Deutschen Physikalischen Gesellschaft **5** (1903).

[9] J. Kübler, A. R. William, and C. B. Sommers, "Formation and coupling of magnetic moments in heusler alloys", Phys. Rev. B **28**, 1745 (1983).

[10] R. A. de Groot, F. M. Mueller, P. G. v. Engen, and K. H. J. Buschow, "New class of materials: half-metallic ferromagnets", Phys. Rev. Lett. **50**, 2024 (1983).

[11] M. Julliere, "Tunneling between ferromagnetic films", Physics Letters A **54A** (1975).

[12] M. Kumar, T. Nautiyal, and S. Auluck, "Full potential results on the magneto-optical properties of the Heusler compounds Co_2FeX (X = Al, Ga, Si and Ge)", Journal of Physics: Condensed Matter **21**, 196003 (2009).

[13] S. Ikeda, K. Miura, H. Yamamoto, K. Mizunuma, H. D. Gan, M. Endo, S. Kanai, J. Hayakawa, F. Matsukura, and H. Ohno, "A perpendicular-anisotropy CoFeB-MgO magnetic tunnel junction", Nature Materials **9**, 721 (2010).

[14] M. Belmeguenai, H. Tuzcuoglu, M. S. Gabor, T. P. Jr., C. Tiusan, F. Zighem, S. M. Chérif, and P. Moch, "Co_2FeAl Heusler thin films grown on Si and MgO substrates: Annealing temperature effect", Journal of Applied Physics **115**, 043918 (2014).

[15] X. Li, S. Yin, Y. Liu, D. Zhang, X. Xu, J. Miao, and Y. Jiang, "Perpendicular Magnetic Anisotropy of Full-Heusler Films in $Pt/Co_2FeAl/MgO$ Trilayers", Applied Physics Express **4**, 043006 (2011).

[16] A. Manchon, C. Ducruet, L. Lombard, S. Auffret, B. Rodmacq, B. Dieny, S. Pizzini, J. Vogel, V. Uhlíř, M. Hochstrasser, and G. Panaccione, "Analysis of oxygen induced anisotropy crossover in $Pt/Co/MOx$ trilayers", Journal of Applied Physics **104**, 043914 (2008).

[17] H. Sukegawa, J. P. Hadorn, Z. Wen, T. Ohkubo, S. Mitani, and K. Hono, "Perpendicular magnetic anisotropy at lattice-matched $Co_2FeAl/MgAl_2O_4$ (001) epitaxial interfaces", Applied Physics Letters **110**, 112403 (2017).

[18] B. Balke, G. H. Fecher, J. Winterlik, and C. Felser, Applied Physics Letters **90**, 152504 (2007).

[19] J. Winterlik, B. Balke, G. Fecher, C. Felser, M. Alves, F. Bernardi, and J. Morais, Physical Review B **77**, 12 (2008).

[20] S. Wurmehl, H. C. Kandpal, G. H. Fecher, and C. Felser, Journal of Physics: Condensed Matter **18**, 6171 (2006).

[21] H. Kurt, K. Rode, M. Venkatesan, P. Stamenov, and J. Coey, "High spin polarization in epitaxial films of ferrimagnetic Mn_3Ga", Physical Review B **83** (2011).

[22] S. Mizukami, A. Sakuma, A. Sugihara, T. Kubota, Y. Kondo, H. Tsuchiura, and T. Miyazaki, "Tetragonal $D0_{22}$ $Mn_{3+x}Ge$ Epitaxial Films Grown on MgO(100) with a Large Perpendicular Magnetic Anisotropy", Applied Physics Express **6**, 123002 (2013).

[23] A. Sugihara, K. Z. Suzuki, T. Miyazaki, and S. Mizukami, "Magnetic properties of ultrathin tetragonal Heusler $D0_{22}$-Mn_3Ge perpendicular-magnetized films", Journal of Applied Physics **117**, 17B511 (2015).

[24] J. Winterlik, S. Chadov, A. Gupta, V. Alijani, T. Gasi, K. Filsinger, B. Balke, G. H. Fecher, C. A. Jenkins, F. Casper, J. Kübler, G.-D. Liu, L. Gao, S. S. P. Parkin, and C. Felser, "Design Scheme of New Tetragonal Heusler Compounds for Spin-Transfer Torque Applications and its Experimental Realization", Advanced Materials **24**, 6283 (2012).

[25] J. J. Versluijs, M. A. Bari, and J. Coey, "Magnetoresistance of half-metallic oxide nanocontacts", Physical Review Letters **87**, 026601 (2001).

[26] R. Degroot, F. Mueller, P. Vanengen, and K. Buschow, "New Class of Materials - Half-Metallic Ferromagnets", Physical Review Letters **50**, 2024 (1983).

[27] S. Trudel, O. Gaier, J. Hamrle, and B. Hillebrands, Journal of Physics D: Applied Physics **43**, 193001 (2010).

[28] C. Felser-Wenz and A. Hirohata, eds., *Heusler alloys*, eng, Vol. 222, Springer series in materials science (Springer, 2016), p. 86.

[29] T. Graf, C. Felser, and S. S. P. Parkin, "Simple rules for the understanding of Heusler compounds", Progress in Solid State Chemistry **39**, 1 (2011).

[30] L. Wollmann, S. Chadov, J. Kübler, and C. Felser, Physical Review B **90**, 214420 (2014).

[31] H. Itoh, T. Nakamichi, Y. Yamaguchi, and N. Kazama, "Neutron Diffraction Study of Heusler Type Alloy $Mn_{0.47}V_{0.28}Al_{0.25}$", Trans. Japan Inst. Met. **24**, 265 (1983).

[32] N. Fukatani, K. Inagaki, T. Miyawaki, K. Ueda, and H. Asano, "Structural and magnetic properties in Heusler-type ferromagnet/ antiferromagnet bilayers", Journal of Applied Physics **113**, 17C103 (2013).

[33] A. K. Nayak, V. Kumar, T. Ma, P. Werner, E. Pippel, R. Sahoo, F. Damay, U. K. Rössler, C. Felser, and S. S. P. Parkin, "Magnetic antiskyrmions above room temperature in tetragonal heusler materials", Nature **548**, 561 (2017).

[34] S. Chadov, X. Qi, J. Kübler, G. H. Fecher, C. Felser, and S. C. Zhang, "Tunable multifunctional topological insulators in ternary heusler compounds", Nature Materials **9**, 541 (2010).

[35] J. Winterlik, G. H. Fecher, C. Felser, M. Jourdan, K. Grube, F. Hardy, H. von Löhneysen, K. L. Holman, and R. J. Cava, "Ni-based superconductor: Heusler compound $ZrNi_2Ga$", Phys. Rev. B **78**, 184506 (2008).

[36] K. Özdogan, I. Galanakis, E. Şaşioglu, and B. Aktaş, "Search for half-metallic ferrimagnetism in V-based Heusler alloys Mn_2VZ (Z=Al, Ga, In, Si, Ge, Sn)", Journal of Physics: Condensed Matter **18**, 2905 (2006).

[37] R. Sahoo, L. Wollmann, S. Selle, T. Häche, B. Ernst, A. Kalache, C. Shekhar, N. Kumar, S. Chadov, C. Felser, S. S. P. Parkin, and A. K. Nayak, "Compensated ferrimagnetic tetragonal heusler thin films for antiferromagnetic spintronics", Advanced Materials **28**, 8499 (2016).

[38] J. W. Criss and L. S. Birks, "Calculation methods for fluorescent x-ray spectrometry. Empirical coefficients versus fundamental parameters.", Analytical Chemistry **40**, 1080 (1968).

[39] J. W. Olesik, "Elemental analysis using ICP — OES and ICP/MS", Analytical Chemistry **63**, 12A (1991).

[40] L. Spieß, *Moderne Röntgenbeugung*, edited by H. Behnken, C. Genzel, R. Schwarzer, and G. Teichert, 2., überarbeitete und erweiterte Auflage (Vieweg+Teubner Verlag / GWV Fachverlage GmbH, Wiesbaden, Wiesbaden, 2009).

[41] L. G. Parratt, "Surface studies of solids by total reflection of x-rays", Phys. Rev. **95**, 359 (1954).

[42] G. Binnig, C. Quate, and C. Gerber, "Atomic force microscope", Physical Review Letters **56**, 930 (1986).

[43] M. H. Grabow and G. H. Gilmer, "Thin film growth modes, wetting and cluster nucleation", Surface Science **194**, 333 (1988).

[44] M. Pritschow, PhD thesis (Institut für Mikroelektronik Stuttgart, 2007).

[45] K. John, "On rotation of the plane of polarization by reflection from the pole of a magnet", The London, Edinburgh, and Dublin Philosophical Magazine and Journal of Science **3**, 321 (1877).

[46] T. Kuschel, H. Bardenhagen, H. Wilkens, R. Schubert, J. Hamrle, J. Pištora, and J. Wollschläger, "Vectorial magnetometry using magnetooptic kerr effect including first- and second-order contributions for thin ferromagnetic films", Journal of Physics D: Applied Physics **44**, 265003 (2011).

[47] S. Foner, "Versatile and sensitive vibrating sample magnetometer", Review of Scientific Instruments **30**, 548 (1959).

[48] J. P. C. Bernards, "Design of a detection coil system for a biaxial vibrating sample magnetometer and some applications", Review of Scientific Instruments **64**, 1918 (1993).

[49] P. J. Flanders, "An alternating gradient magnetometer (invited)", Journal of Applied Physics **63**, 3940 (1988).

[50] C. Chen, Y. Idzerda, H. Lin, N. Smith, G. Meigs, E. Chaban, G. Ho, E. Pellegrin, and F. Sette, Physical Review Letters **75**, 152 (1995).

[51] J. Schmalhorst, D. Ebke, M. Meinert, A. Thomas, G. Reiss, and E. Arenholz, "Element-specific study of the temperature dependent magnetization of Co-Mn-Sb thin films", Journal of Applied Physics **105**, 053906 (2009).

[52] J. Stohr, “Exploring the microscopic origin of magnetic anisotropies with X-ray magnetic circular dichroism (XMCD) spectroscopy”, Journal of Magnetism and Magnetic Materials **200**, 470 (1999).

[53] H. E. Herbert, Philos. Mag. **10**, 301 (1880).

[54] R. Karplus and J. M. Luttinger, “Hall effect in ferromagnetics”, Phys. Rev. **95**, 1154 (1954).

[55] G. Sundaram and Q. Niu, “Wave-packet dynamics in slowly perturbed crystals: gradient corrections and berry-phase effects”, Phys. Rev. B **59**, 14915 (1999).

[56] J. Smit, “The spontaneous hall effect in ferromagnetics ii”, Physica **24**, 39 (1958).

[57] L. Berger, “Side-jump mechanism for the hall effect of ferromagnets”, Phys. Rev. B **2**, 4559 (1970).

[58] L. J. van der Pauw, “A method of measuring specific resistivity and hall effect of discs of arbitrary shape”, Philips Research Reports **13** (1958).

[59] T. Kubota, S. Ouardi, S. Mizukami, G. Fecher, C. Felser, Y. Ando, and T. Miyazaki, “Magnetic and transport properties of tetragonal- or cubic-Heusler-type Co-substituted Mn-Ga epitaxial thin films”, Journal of Applied Physics **113**, 17C723 (2013).

[60] M. Glas, D. Ebke, I. Imort, P. Thomas, and G. Reiss, Journal of Magnetism and Magnetic Materials 333, 134 (2013).

[61] M. Glas, C. Sterwerf, J.-M. Schmalhorst, D. Ebke, C. Jenkins, E. Arenholz, and G. Reiss, Journal of Applied Physics **114**, 183910 (2013).

[62] L. Zhu and J. Zhao, “Perpendicularly magnetized Mn_xGa films: promising materials for future spintronic devices, magnetic recording and permanent magnets”, Applied Physics A, 1 (2013).

[63] C. Felser, V. Alijani, J. Winterlik, S. Chadov, and A. K. Nayak, IEEE Transactions on Magnetics **49**, 682.

[64] H. Kurt, N. Baadji, K. Rode, M. Venkatesan, P. Stamenov, S. Sanvito, and J. Coey, “Magnetic and electronic properties of $D0_{22}$ - Mn_3Ge (001) films”, Applied Physics Letters **101**, 132410 (2012).

[65] J. M. D. Coey, “New permanent magnets; manganese compounds”, Journal of Physics: Condensed Matter **26**, 064211 (2014).

[66] T. Kubota, M. Araidai, S. Mizukami, X. Zhang, Q. Ma, H. Naganuma, M. Oogane, Y. Ando, M. Tsukada, and T. Miyazaki, “Composition dependence of magnetoresistance effect and its annealing endurance in tunnel junctions having Mn-Ga electrode with high perpendicular magnetic anisotropy”, Applied Physics Letters **99**, 192509 (2011).

[67] F. Wu, S. Mizukami, D. Watanabe, H. Naganuma, M. Oogane, Y. Ando, and T. Miyazaki, “Epitaxial $Mn_{2.5}Ga$ thin films with giant perpendicular magnetic anisotropy for spintronic devices”, Applied Physics Letters **94**, 122503 (2009).

[68] S. Mizukami, T. Kubota, F. Wu, X. Zhang, T. Miyazaki, H. Naganuma, M. Oogane, A. Sakuma, and Y. Ando, “Composition dependence of magnetic properties in perpendicularly magnetized epitaxial thin films of Mn-Ga alloys”, Physical Review B **85** (2012).

[69] S. M. Azar, B. A. Hamad, and J. M. Khalifeh, “Structural, electronic and magnetic properties of $Fe_{3-x}Mn_xZ$ (Z=Al, Ge, Sb) Heusler alloys”, Journal of Magnetism and Magnetic Materials **324**, 1776 (2012).

[70] L. Wollmann, S. Chadov, J. Kübler, and C. Felser, “Magnetism in tetragonal manganese-rich Heusler compounds”, Phys. Rev. B **92**, 064417 (2015).

[71] F. Magnus, A. S. Ingason, S. Olafsson, and J. T. Gudmundsson, Thin Solid Films (2011).

[72] Y. Krockenberger, S.-I. Karimoto, H. Yamamoto, and K. Semba, Journal of Applied Physics **112**, 083920 (2012).

[73] A. Niesen, M. Glas, J. Ludwig, J.-M. Schmalhorst, R. Sahoo, D. Ebke, E. Arenholz, and G. Reiss, “Titanium nitride as a seed layer for heusler compounds”, Journal of Applied Physics **118**, 243904 (2015).

[74] A. Niesen, N. Teichert, T. Matalla-Wagner, J. Balluf, N. Dohmeier, M. Glas, C. Klewe, E. Arenholz, J.-M. Schmalhorst, and G. Reiss, “Structural, magnetic, and electrical properties of perpendicularly magnetized $Mn_{4-x}Fe_xGe$ thin films”, Journal of Applied Physics **123**, 113901 (2018).

[75] G. Kádár and E. Krén, "Neutron diffraction study of Mn_3Ge", International Journal of Magnetism **1**, 143 (1971).

[76] T. Ohoyama, "X-ray and Magnetic Studies of the Manganese-Germanium System", Journal of the Physical Society of Japan **16**, 1995 (1961).

[77] A. Niesen, C. Sterwerf, M. Glas, J. M. Schmalhorst, and G. Reiss, IEEE Transactions on Magnetics **52**, 1 (2016).

[78] T. Gasi, A. K. Nayak, J. Winterlik, V. Ksenofontov, P. Adler, M. Nicklas, and C. Felser, Applied Physics Letters **102** (2013).

[79] R. Franz and G. Wiedemann, "Über die Wärme-Leitungsfähigkeit der Metalle", Annalen der Physik **165**, 497 (1853).

[80] N. Stojanovic, D. H. S. Maithripala, J. M. Berg, and M. Holtz, "Thermal conductivity in metallic nanostructures at high temperature: Electrons, phonons, and the Wiedemann-Franz law", Phys. Rev. B **82**, 075418 (2010).

[81] Z.-Y. Quan, L. Zhang, W. Liu, H. Zeng, and X.-H. Xu, "Resistivity dependence of magnetoresistance in Co/ZnO films", Nanoscale Research Letters **9**, 6 (2014).

[82] M. Henini, "Principles of electronic materials and devices (second edition)", Microelectronics journal **33**, 681 (2002).

[83] Z. Wen, H. Sukegawa, S. Mitani, and K. Inomata, "Perpendicular magnetization of Co_2FeAl full-Heusler alloy films induced by MgO interface", Applied Physics Letters **98**, 242507 (2011).

[84] C. Sterwerf, M. Meinert, J.-M. Schmalhorst, and G. Reiss, "High TMR Ratio in Co_2FeSi and Fe_2CoSi Based Magnetic Tunnel Junctions", IEEE Transactions on Magnetics **49**, 4386 (2013).

[85] D. Ebke, Z. Kugler, P. Thomas, O. Schebaum, M. Schäfers, D. Nissen, J. Schmalhorst, A. Hütten, E. Arenholz, and A. Thomas, "X-Ray Absorption and Magnetic Circular Dichroism Studies of Co_2FeAl in Magnetic Tunnel Junctions", Magnetics, IEEE Transactions on **46**, 1925 (2010).

[86] A. Boehnke, U. Martens, C. Sterwerf, A. Niesen, T. Hübner, M. von der Ehe, M. Meinert, T. Kuschel, A. Thomas, C. Heiliger, M. Münzenberg, and G. Reiss, "Large magneto-seebeck effect in magnetic tunnel junctions with half-metallic heusler electrodes", Nature Communications **8**, 1626 (2017).

[87] D. Ebke, P. Thomas, O. Schebaum, M. Schäfers, D. Nissen, V. Drewello, A. Hütten, and A. Thomas, "Low B2 crystallization temperature and high tunnel magnetoresistance in magnetic tunnel junctions", Journal of Magnetism and Magnetic Materials **322**, 996 (2010).

[88] M. Gabor, T. J. Petrisor, O. Pop, S. Colis, and C. Tiusan, "Temperature dependence of the perpendicular magnetic anisotropy in Ta/Co_2FeAl/MgO structures probed by Anomalous Hall Effect", Journal of Magnetism and Magnetic Materials **392**, 79 (2015).

[89] H. Lee, Y.-H. A. Wang, C. K. A. Mewes, W. H. Butler, T. Mewes, S. Maat, B. York, M. J. Carey, and J. R. Childress, "Magnetization relaxation and structure of CoFeGe alloys", Applied Physics Letters **95**, 082502 (2009).

[90] M. Ding and S. J. Poon, "Perpendicular magnetization of $Co_{20}Fe_{50}Ge_{30}$ films induced by MgO interface", Applied Physics Letters **101**, 122408 (2012).

[91] A. Niesen, J. Ludwig, M. Glas, R. Silber, J.-M. Schmalhorst, E. Arenholz, and G. Reiss, "Perpendicular magnetic anisotropy of TiN buffered Co_2FeAl/MgO bilayers", Journal of Applied Physics **121**, 223902 (2017).

[92] M. S. Gabor, T. Petrisor, C. Tiusan, M. Hehn, and T. Petrisor, "Magnetic and structural anisotropies of Co_2FeAl Heusler alloy epitaxial thin films", Physical Review B **84**, 134413 (2011).

[93] K. Inomata, S. Okamura, A. Miyazaki, M. Kikuchi, N. Tezuka, M. Wojcik, and E. Jedryka, "Structural and magnetic properties and tunnel magnetoresistance for Co_2(Cr,Fe)Al and Co_2FeSi full-Heusler alloys", Journal of Physics D: Applied Physics **39**, 816 (2006).

[94] Z. Wen, H. Sukegawa, S. Mitani, and K. Inomata, Applied Physics Letters **98**, 242507 (2011).

[95] S. Mizukami, D. Watanabe, M. Oogane, Y. Ando, Y. Miura, M. Shirai, and T. Miyazaki, "Low damping constant for Co_2FeAl Heusler alloy films and its correlation with density of states", Journal of Applied Physics **105**, 07D306 (2009).

[96] W. Wang, H. Sukegawa, R. Shan, T. Furubayashi, and K. Inomata, "Preparation and characterization of highly $L2_1$-ordered full-Heusler alloy $Co_2FeAl_{0.5}Si_{0.5}$ thin films for spintronics device applications", Applied Physics Letters **92**, 221912 (2008).

[97] D. Ebke, "Cobalt-based Heusler compounds in magnetic tunnel junctions", PhD thesis (2010).

[98] I. Galanakis, "Orbital magnetism in the half-metallic Heusler alloys", Physical Review B **71** (2005).

[99] V. Jung, G. H. Fecher, B. Balke, V. Ksenofontov, and C. Felser, "Electronic structure, magnetic properties and order-disorder phenomena in $Co_2Mn_{1-x}Fe_xAl$", Journal of Physics D: Applied Physics **42**, 084007 (2009).

[100] M. Johnson, P. Bloemen, F. Den Broeder, and J. De Vries, "Magnetic anisotropy in metallic multilayers", Reports on Progress in Physics **59**, 1409 (1996).

[101] W. Wang, H. Sukegawa, and K. Inomata, "Perpendicular Magnetic Anisotropy of Co_2FeAl/Pt Multilayers for Spintronic Devices", Applied Physics Express **3**, 093002 (2010).

[102] S. Maat, M. J. Carey, and J. R. Childress, "Current perpendicular to the plane spin-valves with cofege magnetic layers", Applied Physics Letters **93**, 143505 (2008).

[103] H. J. Elmers, G. H. Fecher, D. Valdaitsev, S. A. Nepijko, A. Gloskovskii, G. Jakob, G. Schönhense, S. Wurmehl, T. Block, C. Felser, P.-C. Hsu, W.-L. Tsai, and S. Cramm, "Element-specific magnetic moments from core-absorption magnetic circular dichroism of the doped Heusler alloy $Co_2Cr_{0.6}Fe_{0.4}Al$", Phys. Rev. B **67**, 104412 (2003).

[104] N. V. Uvarov, Y. V. Kudryavtsev, A. F. Kravets, A. Y. Vovk, R. P. Borges, M. Godinho, and V. Korenivski, “Electronic structure, optical and magnetic properties of Co_2FeGe Heusler alloy films”, Journal of Applied Physics **112**, 063909 (2012).

Publications

1. **Alessia Niesen**, Manuel Glas, Jana Ludwig, Jan-Michael Schmalhorst, Roshnee Sahoo, Daniel Ebke, Elke Arenholz, and Günter Reiss "Titanium nitride as a seed layer for Heusler compounds", Journal of Applied Physics, **118**, 243904 (2015)

2. **Alessia Niesen**, Christian Sterwerf, Manuel Glas, Jan-Michael Schmalhorst, and Günter Reiss "Structural and magnetic properties of sputter deposited $Mn_{3-x}Fe_xGa$ thin films", IEEE Transactions on magnetics, **52**, no. 7, pp. 1-4 (2016)

3. **Alessia Niesen**, Jana Ludwig, Manuel Glas, Robin Silber, Jan-Michael Schmalhorst, Elke Arenholz, Günter Reiss "Perpendicular magnetic anisotropy of TiN buffered Co_2FeAl/MgO bilayers", Journal of Applied Physics, **121**, 223902 (2017)

4. Alexander Boehnke, Ulrike Martens, Christian Sterwerf, **Alessia Niesen**, Torsten Huebner, Marvin von der Ehe, Markus Meinert Timo Kuschel, Andy Thomas, Christian Heiliger, Markus Münzenberg und Günter Reiss "Large magneto-Seebeck effect in magnetic tunnel junctions with half-metallic Heusler electrodes", Nat. Commun. **8**, 1626 (2017)

5. Orestis Manos, Alexander Boehnke, Panagiota Bougiatioti, Robin Klett, Karsten Rott, **Alessia Niesen**, Jan-Michael Schmalhorst und Günter Reiss "Tunneling magnetoresistance of perpendicular CoFeB-based junctions with exchange bias", Journal of Applied Physics, **122**, 103904 (2017)

6. **Alessia Niesen**, Niclas Teichert, Tristan Matalla-Wagner, Jan Balluf, Niklas Dohmeier, Manuel Glas, Jan-Michael Schmalhorst, and Günter Reiss "Structural, magnetic and electrical properties of perpendicularly magnetized $Mn_{4-x}Fe_xGe$ thin films", Journal of Applied Physics, **123**, 113901 (2018).[1]

7. Andres Conca Parra, **Alessia Niesen**, Günter Reiss and Burkard Hillebrands, "Evolution of the interfacial perpendicular magnetic anisotropy constant of the Co_2FeAl/MgO interface upon annealing", Journal of Physics D: Applied Physics, **51**, no. 16, 165303 (2018)

8. Hamza Cansever, Rysard Narkowicz, Kilian Lenz, Ciaran Fowley, Lakshmi Ramasubramanian, Oguz Yildirim, **Alessia Niesen**, Torsten Huebner, Günter Reiss, Jürgen Lindner, Juergen Fassbender and Alina Deac "Investigating spin-transfer torques induced by thermal gradients in magnetic tunnel junctions by using micro-cavity ferromagnetic resonance", Journal of Physics D: Applied Physics, **51**, no. 22, 224009 (2018)

9. Hamza Cansever, Jürgen Lindner, Torsten Huebner, **Alessia Niesen**, Günter Reiss, Juergen Fassbender, Alina Deac "Characterization of Continuous Wave Laser-Induced Thermal Gradients in Magnetic Tunnel Junctions Integrated Into Microresonators via COMSOL Simulations", IEEE Transactions on Magnetics, doi: 10.1109/TMAG.2019.2891903 (2019)

[1] Editor's pick

Conferences

03/2014 Poster at the **78th Deutsche Physikalische Gesellschaft spring meeting**, Dresden, Germany

03/2015 Talk at the **79th Deutsche Physikalische Gesellschaft spring meeting**, Berlin, Germany

05/2015 Talk at the **IEEE International Magnetics Conference (INTERMAG) 2015**, Beijing, China

01/2016 Talk at the **13th Joint Magnetism and Magnetic Materials Conference (MMM-Intermag) 2016**, San Diego (CA), USA

03/2016 Talk at the **80th Deutsche Physikalische Gesellschaft spring meeting**, Regensburg, Germany

11/2016 Poster at the **61st Annual Magnetism and Magnetic Materials Conference (MMM) 2016**, New Orleans (LA), USA

Danksagung

An dieser Stelle möchte ich den vielen Menschen danken, die direkt und/oder indirekt zu der Erstellung dieser Doktorarbeit beigetragen haben.

Als erstes bin ich meinem Doktorvater Prof. Dr. Günter Reiss zu großem Dank verpflichtet für die Möglichkeit, im Rahmen eines DFG geförderten Projektes, in seiner Gruppe zu promovieren! Ich danke für die Möglichkeit eine selbstständige und freie Forschung zu betreiben, sowie für das stets offene Ohr und eine hervorragende Betreuung!

Des Weiteren danke ich Dr. Jan Michael Schmalhorst, der mich bei vielen Fragen der Physik immer unterstützt und auf den rechten Weg gebracht hat. Dr. Karsten Rott möchte ich von ganzem Herzen, für die stete Hilfsbereitschaft in allen Fragen der Betreuung von Maschinen, Instandhaltung von Pumpen und sämtlichem Laborequipment danken!

Für die Möglichkeit Messungen an der Beamline 4.0.2 an der Advanced Light Source (Berkeley, CA) durchführen zu können, sowie für die tatkräftige Unterstützung bei den Messungen danke ich Dr. Elke Arenholz, Dr. Jan Michael Schmalhorst, Dr. Christoph Klewe, Niklas Dohmeier und Dr. Jan Balluf. Ich danke Tristan Matalla-Wagner für das Durchführen der VSM Messungen. Ganz herzlich möchte ich Michel Bovender und Jan Krieft danken, ohne deren unermüdlichen Einsatz beim Bestec Instandhalten und die stets tolle Arbeit und Zuverlässigkeit beim Umbau der Sputteranlage, die Herstellung der Proben unmöglich gewesen wäre!

Für eine tolle Zusammenarbeit, eine großartige Kollegialität, Hilfsbereitschaft und Atmosphäre, die es einem stets ermöglichte voller Motivation an die Arbeit zu gehen, danke ich meinen Kollegen Dr. Daniel Meier, Dr. Stefan Niehörster, Dr. Christian Sterwerf, Dr. Alexander Böhnke, Dr. Christoph Klewe,

Polina Bougiattioti, Orestis Manos, Robin Silver, Anastasiia Moskaltsova und dem gesamten D2-Team. Dr. Manuel Glas danke ich für die geleistete Vorarbeit auf dem Gebiet der senkrechten Heusler, für die großartige Unterstützung bei der Betreuung der Leybold, sowie den guten Zuspruch, den ich oft gebraucht habe!

Einen besonderen Dank möchte ich an Dr. Niclas Teichert richten, für seine Unterstützung und Motivation, insbesondere dabei dieser Arbeit den letzten Schliff zu verleihen!

Mein besonderer Dank gilt ebenfalls Aggi Windmann, für ihre sehr herzliche und kompetente Art, mit welcher sie uns häufig durch den Verwaltungsdschungel geführt hat, sowie für die vielen wundervollen und liebevoll zubereiteten Frühstücke!

Meiner Familie und allen meinen Freunden, inklusive der ehemaligen Kollegen, die nunmehr sehr gute Freunde geworden sind, gebührt meine tiefste Dankbarkeit! Ich danke meinen Eltern, meiner Schwester, meiner Cousine und meinen engsten Freunden für Ihre fortwährende Unterstützung während des gesamten Studiums, sowie der Promotion. Ich danke Euch für die Kraft, die gute Laune, die vielen tollen gemeinsamen Momente, die mich in dieser Zeit stets weitergebracht und motiviert haben!